

Study on luminescence and structural properties of vanadates phosphors

by

**Kewele Emily Foka
(MSc)**

A thesis submitted in fulfilment of the requirements for the degree

PHILOSOPHIAE DOCTOR

in the

Faculty of Natural and Agricultural Sciences

Department of Physics

at the

University of the Free State

Promoter: Prof B.F Dejene

Co-Promoter: Prof H.C. Swart

January 2016

Acknowledgements

I would like to say thanks to a number of people that helped me in accomplishing the work presented in this thesis.

Firstly I would like to thank Prof. B.F Dejene as supervisor for his guidance and mentorship. His guidance and perseverance has taught me a lot in the last years. We have working together to complete projects in all the years during my PhD studies, I am very thankful for his undivided attention he has showed towards me.

I would also like to thank my co-supervisor Prof. H.C Swart for his encouragement and support during the entire course of my studies.

I am very thankful to the staff of National Laser Center (CSIR) for showing me how to operate the PLD system.

I would like to thank the staff members of the Department of Chemistry (Dr. Puseletso Mofokeng) for their assistant with the DSC and TGA measurements.

I also want to thank my fellow researchers (Seithati Tebele, Lephoto Mantwa, Pulane mokoena, Fokotsa Molefe, Ungula Jathan, Ali Wako, Ali Abdul, Winfred Mweni, Thembikosi Malevu, Mart-Marie Duvenhage, Mokoena Puseletso, Yousif) for their support and special thanks to Massie Tshabalala for her assistant whenever I needed her in Bloemfontein.

I'm also thankful to all the staff members of the Physics department. Special thanks to Dr. L.F Koao for always helping me with my PhD project. I have learned many things from him. Ms Meiki Lebeko for always assisting us when we needed her.

I am grateful to the financial support from the South African National Research Foundation and the University of the Free State.

I am very thankful to my husband (Qinimuze Lethlatla) for always being there for me, my son (Sibusiso), my mother, my in-laws, my brothers, sisters, and friends.

To all: Thank you

With God everything is possible

Abstract

A self-activated yellow emitting zinc vanadate ($Zn_2V_2O_7$) was synthesized by combustion method. The influence of the processing parameters such as synthesis temperature and dopants concentration on the structure, morphology and luminescence properties was investigated. The X-ray diffraction (XRD) analysis confirmed that the samples have a tetragonal structure and no significant structural change was observed in varying both the synthesis temperature and the dopants concentration. The estimated average grain size was 78 nm for the samples synthesized at different temperatures and 77 nm for the doped samples. Scanning electron microscope (SEM) images show agglomerated hexagonal-like shape particles with straight edges at low temperatures and the shape of the particles changed to cylindrical-like structures at moderate temperatures but were destroyed at higher temperatures. The microstructure retained its original structure when the phosphor was doped with Ba, Ca and Sr. The photoluminescence (PL) of the product exhibited broad emission bands ranging from 400 to 800 nm. The best luminescence intensity was observed for the undoped $Zn_2V_2O_7$ samples and those synthesized at 600°C. Any further increase in synthesis temperature and concentration of dopants, respectively, led to a decrease in the luminescence intensity. The broad band emission peak of $Zn_2V_2O_7$ consist of two broad band's corresponding to emission from the Em_1 (${}^3T_2 \rightarrow {}^1A_1$) and Em_2 (${}^3T_1 \rightarrow {}^1A_1$) transitions.

The $Zn_2V_2O_7$ phosphor was prepared by a sol-gel method. The effect of annealing temperature on the structure and photoluminescence of $Zn_2V_2O_7$ was investigated. The XRD results showed the single monoclinic phase of $Zn_2V_2O_7$. The crystallinity of the $Zn_2V_2O_7$ phosphor improved while the full width at half maximum of (022) XRD peak was decreased with the increase in annealing temperature. SEM showed that the grains size increased with the increase in annealing temperature, which is due to the improvement in crystallinity of $Zn_2V_2O_7$. Thermal behaviour of the $Zn_2V_2O_7$ phosphor was investigated by Thermogravimetric analysis (TGA) and differential scanning calorimetry (DSC), respectively. TGA results showed a total weight loss of 65.3% when temperature was risen from 35 to 500°C. The photoluminescence emission spectra of annealed $Zn_2V_2O_7$ powders showed a broad band emission from 400 to 800 nm. The PL intensity enhanced as the annealing temperature was increased, resulting to an improvement of the crystallinity. PL emission peaks shift from green emission towards a yellow emission.

Dy doped $\text{YVO}_4:\text{Dy}^{3+}$ phosphors were produced by the combustion method at 600°C . The structure and optical properties of the powders were investigated. The XRD patterns showed the tetragonal phase similar to the standard JCPD file (17-0341). SEM shows that the particle sizes were small and agglomerated, and the size increased with the Dy^{3+} dopant concentration and its shape changed to bulk-like particles. In PL, the emission spectra exhibited a weak band at 663 nm for the ${}^4\text{F}_{9/2} - {}^6\text{H}_{11/2}$ transition and a peak at 483 nm (blue) for the ${}^4\text{F}_{9/2} - {}^6\text{H}_{15/2}$ transition and a 574 nm (yellow) peak with higher intensity for the ${}^4\text{F}_{9/2} - {}^6\text{H}_{13/2}$ transition.

The dependence of the properties of $\text{YVO}_4:\text{Dy}^{3+}$ phosphor upon urea:nitrate concentration was investigated. The samples were synthesized by combustion method. The single tetragonal phase was observed by x-ray diffraction spectra. A highly crystalline $\text{YVO}_4:\text{Dy}^{3+}$ sample was observed when increasing the ratio of the urea to 2. The estimated crystalline size were found to be 20, 39, 33, 30, and 27 nm for the sample prepared with the ratio of 1, 2, 2.5, 3 and 4, respectively. The formation of agglomerated particles was observed by SEM images and it was observed that when increasing the concentration of urea further the flake-like particles formed. The UV diffuse reflectance spectra of $\text{YVO}_4:\text{Dy}^{3+}$ with various ratios of urea showed the determined optical band gap ranging from 3.3 to 2.3 eV. Luminescence properties of $\text{YVO}_4:\text{Dy}^{3+}$ showed that the phosphor emit yellow colour at 573 nm and blue colour at 482 nm corresponding to ${}^4\text{F}_{9/2} \rightarrow {}^6\text{H}_{13/2}$ and ${}^4\text{F}_{9/2} \rightarrow {}^6\text{H}_{15/2}$, respectively. A very weak band at 663 nm which correspond to ${}^4\text{F}_{9/2} \rightarrow {}^6\text{H}_{11/2}$ transition was also observed. It was found that the PL emission intensity increases with an increase in the ratio of urea and reached maximum at 2 then decreases when increasing the ratio of urea further.

$\text{YVO}_4:\text{Eu}$ thin films were well deposited by pulse laser deposition at deposition temperature of 200, 300 and 400°C . The oxygen pressure and deposition time were held constant. The films deposited at higher temperature showed a tetragonal phase. The XRD spectra for the sample deposited at 200°C showed a very small peak at (200) orientation. Phosphor thin film showed a crystalline structure when the temperature increased. SEM images indicated larger particles at higher temperature. Atomic force microscopy (AFM) results showed the smooth surface with small particles at lower temperature and surface roughness at higher temperature due to the crystallinity. The PL shows the typical emission peaks of Eu in a red region at the 594 and 618 nm attributed to ${}^5\text{D}_0 - {}^7\text{F}_1$ and ${}^5\text{D}_0 - {}^7\text{F}_2$, transitions. Also the peaks at 652 and 699 nm corresponding to ${}^5\text{D}_0 - {}^7\text{F}_3$ and ${}^5\text{D}_0 - {}^7\text{F}_4$ are observed. The spectra showed an increase in intensity when deposition temperature was increased.

YVO₄:Eu³⁺ thin films were prepared by pulse laser deposition (PLD). YVO₄:Eu³⁺ thin films were deposited at room temperature by varying the deposition time from 30, 45 to 60 minutes. The XRD analysis confirmed that the samples have a tetragonal phase. The improved on crystallinity of the films was observed when increasing deposition time. The estimated grain particle size increased from 52 to 69 nm as the deposition time increased from 30 to 60 minutes, respectively. SEM images showed that when increasing the deposition time, particles were agglomerated and the formation of homogeneous surface was observed for a film deposited at 45 minutes. The rough surface with larger particles was observed for the sample deposited at 60 minutes. PL emission spectra of YVO₄:Eu³⁺ showed the main emission peaks which are due to the Eu³⁺ transition ⁵D_j→⁷F_j. The strongest red emission peak at 618 nm is due to transition ⁵D₀→⁷F₂. The increased in deposition time showed the improvement in intensity of the thin films.

Keywords: Sol-gel, Dopants, Thin films, Vanadates, Deposition, Transitions, Combustion, Crystallinity, Luminescence, Thermogravimetric

DECLARATION

I (Foka Kewele Emily) declare that the thesis hereby submitted by me for the Philosophiae Doctor degree at the University of the Free State (Qwa Qwa Campus) is my own independent work and has not previously been submitted by me at another university/faculty. I furthermore, cede copyright of the thesis in favor of the University of the Free State.

Signature:.....

Date:.....

Table of Contents

Acknowledgements.....	ii
Abstract.....	iii
Keywords.....	v
Declaration.....	vi
Chapter 1. Introduction.....	1
1.1 Luminescence.....	2
1.2 Vanadates/Metavanadates.....	2
1.3 Light Emitting Diode (LED).....	3
1.4 Rare earth (RE) elements.....	3
1.4.1 Dysprosium.....	4
1.4.2 Europium.....	4
1.4.3 Yttrium.....	5
1.5 Rare earth luminescence.....	5
1.5.1 d-f transition (Eu^{2+}).....	6
1.5.2 h-f transition (Dy^{3+}).....	6
1.6 Structural characteristics of vanadate host.....	6
1.6.1 Crystal structure of $\text{Zn}_2\text{V}_2\text{O}_7$	7
1.6.2 Crystal structure of YVO_4	7
1.7 Problem statement.....	8
1.8 Aim of the study.....	9
1.9 Research objectives.....	9
1.10 Thesis layout.....	9
References.....	11
Chapter 2. Synthesis and characterization technique.....	13
2.1 Introduction.....	13

2.2 Sol-gel method.....	13
2.3 Combustion method.....	15
2.4 Pulse laser deposition (PLD).....	16
2.5 Characteristics techniques.....	18
2.5.1 Atomic force microscopy (AFM).....	18
2.5.2 Fourier transform infrared spectrometer (FTIR).....	19
2.5.3 X-ray diffraction (XRD).....	20
2.5.4 Thermogravimetric analysis (TGA).....	21
2.5.5 Differential scanning calorimetry (DSC).....	21
2.5.6 Scanning electron microscopy and Energy dispersive spectrometer.....	21
2.5.7 Photoluminescence.....	22
References.....	23
Chapter 3. Structural and luminescence properties of self-yellow emitting undoped $Zn_2V_2O_7$ and (Ca, Ba, Sr)-doped $Zn_2V_2O_7$ phosphors synthesised by combustion method.....	24
3.1 Introduction.....	24
3.2 Results and discussion.....	25
3.3 Conclusion.....	34
References.....	35
Chapter 4. The effect of annealing temperature on the structure and luminescence of $Zn_2V_2O_7$ prepared by sol-gel method.....	37
4.1 Introduction.....	37
4.2 Results and discussion.....	38
4.3 Conclusion.....	44
References.....	45
Chapter 5. Combustion synthesis of Dy^{3+} -doped YVO_4	47
5.1 Introduction.....	47
5.2 Results and discussion.....	47

5.3 Conclusion.....	54
References	55
Chapter 6. The effect of urea:nitrate ratio on the structure and luminescence properties of YVO ₄ :Dy ³⁺ phosphors	56
6.1 Introduction	56
6.2 Results and discussion.....	57
6.3 Conclusion.....	64
References	65
Chapter 7. Effect of substrate temperature on structure and luminescence properties of YVO ₄ :Eu thin films grown by PLD.....	67
7.1 Introduction	67
7.2 Results and discussion.....	67
7.3 Conclusion.....	72
References	75
Chapter 8. Optimizing deposition time to enhanced photoluminescence properties of laser-ablated red Eu ³⁺ doped YVO ₄ thin films.....	76
8.1 Introduction	76
8.2 Results and discussion.....	77
8.3 Conclusion.....	84
References	86
Chapter 9	87
9.1 Summary	87
9.2 Future work	88
9.3 Publications.....	90

LIST OF FIGURES

1. Figure 1.1: Transition metal ion atomic structure of RE's	5
2. Figure 1.2: Schematic diagram of the energies of $4f^7$ and $4f^65d^1$ levels in Eu^{2+} influenced by crystal field Δ	6
3. Figure 1.3: The schematic crystal structure of monoclinic $\text{Zn}_2\text{V}_2\text{O}_7$	7
4. Figure 1.4: The schematic crystal structure of tetragonal YVO_4	8
5. Figure 2.1: Schematic diagram of $\text{Zn}_2\text{V}_2\text{O}_7$ prepared by the sol-gel method.....	14
6. Figure 2.2: shows the schematic of the PLD setup.....	17
7. Figure 2.3: General principle of AFM.....	18
8. Figure 2.4: Schematic diagram of a Michelson Interferometer.....	19
9. Figure 2.5: shows the schematic of the XRD setup.....	20
10. Figure 2.6: Typical experimental set-up for PL measurements.....	22
11. Figure 3.1: XRD patterns of $\text{Zn}_2\text{V}_2\text{O}_7$ phosphor prepared at different synthesis combustion Temperature.....	25
12. Figure 3.2: XRD powder diffraction of (111) peak for $\text{Zn}_2\text{V}_2\text{O}_7$ phosphor prepared at different synthesis combustion temperature.....	25
13. Figure 3.3: XRD patterns of the products of (a) undoped $\text{Zn}_2\text{V}_2\text{O}_7$ phosphor and $\text{Zn}_2\text{V}_2\text{O}_7$ doped with (b) Ba, (c) Ca and (c) Sr.....	26
14. Figure 3.4: XRD powder diffraction patterns of (111) for $\text{Zn}_2\text{V}_2\text{O}_7$ phosphor doped with Ba, Ca and Sr.....	26
15. Figure 3.5: The schematic crystal structure of monoclinic $\text{Zn}_2\text{V}_2\text{O}_7$	27
16. Figure 3.6: The SEM micrographs of $\text{Zn}_2\text{V}_2\text{O}_7$ (a) 500, (b) 600 and (c) 700 °C at higher Magnification.....	28
17. Figure 3.7: SEM micrographs of (a) $\text{Zn}_2\text{V}_2\text{O}_7$, (b) $\text{Zn}_2\text{V}_2\text{O}_7$ doped Ba, (c) $\text{Zn}_2\text{V}_2\text{O}_7$ doped Ca and (d) $\text{Zn}_2\text{V}_2\text{O}_7$ doped Sr phosphor.....	29
18. Figure 3.8: FTIR spectra of the products of undoped $\text{Zn}_2\text{V}_2\text{O}_7$ and $\text{Zn}_2\text{V}_2\text{O}_7$ doped with Ba, Ca and Sr.....	30
19. Figure 3.9: Effect of synthesis temperature on the PL (a) excitation and (b) emission intensity of $\text{Zn}_2\text{V}_2\text{O}_7$	30

20. Figure 3.10: (a) PL excitation spectra of $Zn_2V_2O_7$ doped (Ba, Ca and Sr) and (b) emission spectra of $Zn_2V_2O_7$ doped (Ba, Ca and Sr).....	31
21. Figure 3.11: (a) PL emission spectra of $Zn_2V_2O_7$ doped (a) Sr, (b) Ca and (c) Ba. Black line indicates the emission spectra and the dotted lines are the fitted emission spectrum by two fitted with two Gaussian curves corresponding to emission bands Em_1 and Em_2	32
22. Figure 3.12: Schematic model for excitation and emission process of VO_4 tetrahedron with T_d symmetry in $Zn_2V_2O_7$	32
23. Figure 3.13: CIE chromaticity diagram for $Zn_2V_2O_7$ synthesized at $600^\circ C$, and $Zn_2V_2O_7$ doped with (Ba, Ca, and Sr).....	33
24. Figure 4.1: (a) TGA and (b) DSC curves of the $Zn_2V_2O_7$ powder prepared by sol gel	38
25. Figure 4.2: XRD spectra of $Zn_2V_2O_7$ powder annealed at (a) 700 (b) 770 and (c) $850^\circ C$ for 2 Hours.....	39
26. Figure 4.3: Full width at half maximum of the (022) XRD peak as a function of annealing Temperature.....	39
27. Figure 4.4: SEM images of $Zn_2V_2O_7$ powder annealed at (a) 700 (b) 770 and (c) $850^\circ C$ for 2 Hours.....	40
28. Figure 4.5: EDS spectra $Zn_2V_2O_7$ powder prepared by sol gel.....	41
29. Figure 4.6: (a) Photoluminescence emission spectra of $Zn_2V_2O_7$ powder annealed at 700, 770 and $850^\circ C$ for 2 hours (b) PL emission spectra of $Zn_2V_2O_7$ annealed at $850^\circ C$ fitted with two Gaussian curves.....	41
30. Figure 4.7: PL intensity as a function of annealing temperature.....	42
31. Figure 4.8: CIE chromaticity colour diagram of $Zn_2V_2O_7$ annealed at 700, 750 and $850^\circ C$	42
32. Figure 5.1: XRD pattern for the $YVO_4:Dy^{3+}$ phosphors –doped with different concentration of Dy^{3+} as well as the standard JCPD file (17-0341).....	48
33. Figure 5.2: FTIR spectra of $YVO_4:Dy^{3+}$	48
34. Figure 5.3: SEM image of $YVO_4:Dy^{3+}$ doped with (a) 0.5, (b) 1, (c) 1.5, and (d) 2 mol % Dy^{3+} ions.....	49
35. Figure 5.4: Excitation spectra of $YVO_4:Dy^{3+}$	51

36. Figure 5.5: PL emission spectra of YVO ₄ :Dy ³⁺	51
37. Figure 5.6: (a) 574 nm PL peak intensity vs concentration graph of the YVO ₄ :Dy ³⁺ phosphor, (b) CIE of YVO ₄ :Dy ³⁺	52
38. Figure 5.7: Decay curves of YVO ₄ :Dy ³⁺ phosphors with different concentration of Dy ³⁺	53
39. Figure 6.1: XRD patterns of YVO ₄ :Dy ³⁺ with various ratios of urea:nitrate (a) 1, (b) 2, (c) 2.5, (d) 3 and (e) 4.....	57
40. Figure 6.2: SEM images of YVO ₄ :Dy ³⁺ for different ratios of urea. (a) 1 (b) 2 (c) 2.5 (d) 3 and (e) 4.....	59
41. Figure 6.3: EDS spectra of YVO ₄ :Dy ³⁺ for the ratio of 2 urea:nitrate.....	59
43. Figure 6.4: The reflectance spectra for YVO ₄ :Dy ³⁺ structures prepared with different ratios of urea:nitrate (a) 1, (b) 2, (c) 2.5, (d) 3 and (e) 4.....	60
44. Figure 6.5: PL excitation spectra of YVO ₄ :Dy ³⁺ with different ratio of urea:nitrate.....	60
45. Figure 6.6: PL emission spectra of YVO ₄ :Dy ³⁺ with different ratio of urea:nitrate.....	61
46. Figure 6.7: PL intensity of the ⁴ F _{9/2} → ⁶ H _{13/2} and the ⁴ F _{9/2} → ⁶ H _{15/2} transitions as a function of the ratio of urea:nitrate.....	61
47. Figure 6.8: CIE chromaticity diagram showing the dependence of the emission colour with regard to the urea:nitrate ratio in the synthesized YVO ₄ :Dy ³⁺ powders.....	63
48. Figure 6.9: Luminescence decay curves of ⁴ F _{9/2} for YVO ₄ : Dy ³⁺ at different ratio of urea:nitrate.....	63
49. Figure 7.1: XRD spectra of YVO ₄ :Eu ³⁺ thin films deposited at various substrate temperatures (200, 300 and 400°C).....	68
50. Figure 7.2: XRD powder diffraction of (200) peak for YVO ₄ :Eu ³⁺ thin films deposited at various substrate temperatures (200, 300 and 400°C)......	68
51. Figure 7.3: SEM images of YVO ₄ :Eu ³⁺ thin films deposited at (a) 200°C and (b) 400°C.....	69
52. Figure 7.4: AFM images of YVO ₄ :Eu ³⁺ thin films deposited at (a) 200°C (b) 300°C and (c) 400°C.....	69

53. Figure 7.5: PL excitation spectra of $\text{YVO}_4:\text{Eu}^{3+}$ thin films deposited at substrate temperature of (a) 200 °C (b) 300 °C and (c) 400 °C.....	70
54. Figure 7.6: PL emission spectra of $\text{YVO}_4:\text{Eu}^{3+}$ thin films deposited at substrate temperature of (a) 200°C (b) 300°C and (c) 400°C.....	71
55. Figure 7.7: PL emission spectra of $\text{YVO}_4:\text{Eu}^{3+}$ thin films deposited at 400°C at 20, 50, 72 and 85 mTorr.....	71
56. Figure 7.8: PL intensity of $\text{YVO}_4:\text{Eu}^{3+}$ thin films as a function of oxygen pressure in mTorr.....	71
57. Figure 7.9: Luminescence decay curve of $\text{YVO}_4:\text{Eu}^{3+}$ thin films deposited at 20, 50, 72 and 85 mTorr Observed at 618 nm emission and 6270 excitation under 400°C.....	72
58. Figure 7.10: (a) Diffuse reflectance and (b) band gap energy of the $\text{YVO}_4:\text{Eu}^{3+}$ thin films deposited at 20, 50, 72 and 85 mTorr.....	73
59. Figure 8.1: XRD patterns of $\text{YVO}_4:\text{Eu}^{3+}$ deposited at (a) 30, (b) 45 and (c) 60 minutes.....	79
60. Figure 8.2: XRD powder diffraction patterns of [200] for $\text{YVO}_4:\text{Eu}^{3+}$ (a) 30, (b) 45 and (c) 60 minutes.....	79
61. Figure 8.3: average grain size as a function of deposition time for (200) plane.....	79
62. Figure 8.4: SEM images of the $\text{YVO}_4:\text{Eu}^{3+}$ thin films deposited at different times (a) 30, (b) 45 and (c) 60 minutes in 5 mTorr at room temperature.....	80
63. Figure 8.5: AFM images for $\text{YVO}_4:\text{Eu}^{3+}$ thin films deposited at different deposition times (a) 30, (b) 45 and (c) 60 minutes at 5 mTorr.....	80
64. Figure 8.6: rms roughness as a function of deposition time.....	81
65. Figure 8.7: Excitation spectra of the $\text{YVO}_4:\text{Eu}^{3+}$ thin films deposited at different deposition time of (a) 30 (b) 45 and (c) 60 minutes.....	82
66. Figure 8.8: emission spectra of the $\text{YVO}_4:\text{Eu}^{3+}$ thin films deposited at different deposition time of 30, 45 and 60 minutes.....	82
67. Figure 8.9: PL intensity as a function of deposition time.....	84
68. Figure 8.10: CIE chromaticity diagram showing the red emission colour for $\text{YVO}_4:\text{Eu}^{3+}$ thin Films.....	84

69. Figure 8.11: luminescence decay curves of $\text{YVO}_4:\text{Eu}^{3+}$ thin films deposited at different deposition time of 30, 45 and 60 minutes.....84

1. Introduction

The word phosphor is the word used to mean luminescence material. Luminescence material essentially emits light by containing one type of energy into another. Phosphor material can be a combination of a host lattice and an activator/dopant and co-activator of any amount of mole percent. The phosphor activated with rare earth resulted into a luminescence properties. The materials of the phosphor absorb the incident energy and convert it into light in the electromagnetic spectrum regions. The whole process includes the energy transfer from the UV to the electrons in phosphor. The phosphor electrons are raised to the higher energy levels after they have been excited by a source energy and return to the ground state after the light has been emitted [1]. Phosphor have various potential applications especially in an energy saving. These applications can be in a light source by fluorescent lamps, display devices by cathode ray tube, detector system by x-ray screens.

A development on phosphors has stimulated on luminescence materials as the light emitting component in flat panel displays (FPD) such as field emission displays (FED) [2]. The research on the luminescence nanostructure materials is attractive for a FED applications. The small size of nano-materials is penetrated by a low voltage electrons utilization of an efficient material. The recent development of phosphors has been on light emitting diode (LEDs) and white light emitting diode (W-LEDs) [3]. The W-LEDs are finding their way into general lighting applications. High efficiency in light conversion and high thermal quenching temperature are needed for a LED phosphor to be applied in the commercial products. Also LEDs must have possibility to adjust to the colour point by varying the chemical composition. Among these developments of the white light LEDs, the single broad band emitting phosphor materials needed to be developed for the low cost W-LEDs. Some of these broad band materials are vanadates (vanadium oxide). These vanadates materials have shown an efficient intense charge transfer (CT) absorption bands in the near-ultraviolet region and broad emission from 400 to 700 nm [4-5].

1.1 Luminescence

Luminescence has been interesting since the ancient times. The term luminescence was first used in 1888 by the great German Physicist and historian of science, Eilhardt Wiedemann [6]. Luminescence is the emission of light by certain materials when they are relatively cool. The development of luminescence has been done by invention of the fluorescence lamp and the new phosphors for screen [7]. Light emission does not result from the material being above room temperature, so luminescence is often called cold light. Luminescence emission occurs after a material has been absorbed energy from a source such x-ray radiation, electron beams etc. The atoms of the materials lift up into an excitation state, and then the material undergoes another transition because of the unstable excitation state. Then the atoms of the materials fall back to its ground state, and the absorbed energy is liberated in the form of heat or light. Electrons taking part in the luminescence process are the outermost electrons of the atoms or molecules. For example: in fluorescent lamps, a mercury atom is excited by the impact of an electrons having energy of ~ 6.7 eV raising one of the two outermost electrons to a higher level. The energy difference is estimated as ultraviolet light of wavelength of 185 nm, as the electrons returns to the ground state.

1.2 Vanadates/metavanadates

Vanadates are group of minerals or compound. Vanadates are classified in the phosphates group. The vanadates are prepared by combining vanadium pentoxide with oxide or carbonate of metal with calculated quantity, or by ammonium metavanadate with carbonate or nitrates. The metavanadates are white or pale yellow in colour. Vanadates are almost soluble in water but become insoluble in the presence of small quantities of the precipitate agent. Some vanadates of mercury, lead and copper ion are fuse at higher temperature of about 600°C . In other hand vanadates of aluminium, calcium, zinc etc., can be destroyed and be bad conductors of electricity if they fuse at much higher temperature. The following metavanadates have been reported in this work, Yttrium vanadate (YVO_4) and zinc vanadates ($\text{Zn}_2\text{V}_2\text{O}_7$).

Zinc vanadates have luminescence properties such as broadband emission from 400 to 700 nm. The broadband is due to the charge transfer (CT) of an electron from the oxygen $2p$ orbital to the vacant $3d$ orbital of V^{5+} in tetrahedral VO_4 with T_d symmetry [8]. The broadband emission luminescence in the visible light range is effective to obtain a good colour rendering

properly for the lighting devices [9]. Vanadates have many applications in the fields of optical laser, electrochemistry, biology materials and catalyst [10]. These materials have been applied to various types of LED and w-LED.

1.3 Lighting emitting diode (LED)

The phosphors studied in this work are designed for applications of LED's. The first practical visible spectrum LED was developed by Nick Holonyak in 1962 [11]. He invented the first yellow LED by injecting the charge carriers into silicon Carbide via a metal contact [12]. The type of luminescence found in LED is known as injection electroluminescence. LED is consisted of a p-type semiconductor and n-type semiconductor of the same kind (p-n homojunction). LED emits light from the LED surface by

- Increasing the concentration dopants of the substrate, so the electron charge carriers can move to the top, recombine and emit light
- Increasing the diffusion length $L = \sqrt{D\tau}$, where D is the diffusion coefficient and τ is the carrier life time. The performance of LED is characterized by its quantum efficiency (η_{ext}), where quantum efficiency is the product of three components:

$$\eta_{ext} = \eta_{inj} \times \eta_{rad} \times \eta_{opt} \quad (1)$$

Where η_{inj} is the injection efficiency, η_{rad} is the internal quantum efficiency (radiative efficiency) and η_{opt} is light-extraction efficiency (optical efficiency). There are various applications of LED such as devices, clothing, medical application, lighting, remote controls (e.g. TVs), optoisolator, etc.

1.4 Rare earth (RE) elements

The RE's have been around since the formation of earths. Geijer reported on a black mineral stone found by Carl Alex in a small town of Ytterby [12]. That black stone was a mixture of RE's and the stone was called ytteria. The first element to be isolated was cerium. From the mineral ceria; the light lanthanides, lanthanum, samarium, europium and gadolinium were separated [13]. Didymium was found later to be a mixture of praseodymium and neodymium. The mineral was containing the following elements terbium, cerium, yttrium, holmium, dysprosium, lutetium, and europium [13]. RE's metals are all relatively electropositive metals that favoured the tripositive oxidation state and are composed of the 15 lanthanides (from lanthanum to lutetium), plus scandium and yttrium. They all can enter a +3 oxidation state in which both s electrons are lost and either d or f electron as well, but some of the lanthanide

rare earths also show +2 or +4 oxidation state. These RE's can form a very important class of luminescence activator in phosphors and single crystals [14]. Lanthanide (Ln) ions can exhibit sharp fluorescent emissions via intra-4f or 4f–5d transitions and thus are widely used as emitting species in many phosphors [15]. The RE ions are characterized by a partially filled 4f shell that is well shielded by 5s² and 5p⁶ orbitals [16]. The 4f shell remains unfilled, which means that the electrons in the 4f shell are optically active. The states arising from the various 4fⁿ configurations therefore tend to remain nearly invariant for a given ion. This shielding produces narrow spectral lines, long fluorescence lifetimes and energy level that are relatively insensitive to their host environment because the optically active electrons interact weakly with the ions environment [17].

1.4.1 Dysprosium

Dysprosium was first found by Paul Lecoq in 1886 [18]. The name dysprosium was derived from the Greek word dysprositos [19]. Dysprosium is a bright, soft, silver-white RE metal. It dissolves in both diluted and concentrated acids. The most common oxidation state is +3. Dysprosium has a high thermal neutron absorption cross-section, which makes it an excellent neutron absorber.

In this thesis dysprosium is used as a trivalent ion activator and its luminescence properties were studied. Dysprosium is also used in several other fields of science and technology. It is used for its high thermal neutron absorption cross-section in making control rods nuclear reactors. It is used in ships solar systems as sensors and transducers. It also used in data storage applications such as compact discs and hard discs. It is also used for making laser materials when combined with vanadium [20].

1.4.2 Europium

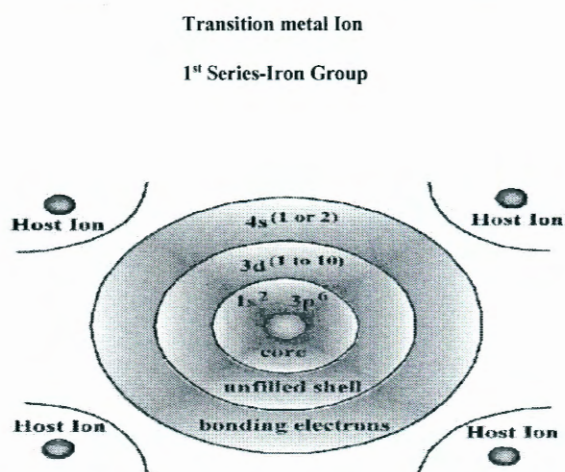
The spectral line of europium was discovered by the chemist Paul-Emile Lecoq in 1890 [18]. Europium was named after the continent Europe. It is a hard, silvery metal which oxidized in air and water. The source of Europium was found in the Basnasite and monazite. It can also be found in the sun and some stars. Europium is found in the oxidation state of +3 and +2, where the divalent ions are more often occurring. This is in contract to all the other rare earth ions which are mostly stable as trivalent ions. The luminescence properties of europium are strictly observed when using the divalent and trivalent europium. Europium-activated yttrium vanadate is used as the red phosphor in colour television tube. Europium activated phosphors are used in cathode ray tube, fluorescent tube.

1.4.3 Yttrium

Yttrium was named and discovered by Carl Alex Arrhenius when he found a new mineral and named it after a village Yttria in 1787 [21]. Yttrium is a soft, silvery metal. Yttrium usually exists as trivalent ion Y^{3+} in its compound. Yttrium is classified as one of the RE element of the lanthanide series. Yttrium can react with water to form yttrium hydroxide. Yttrium is used in making a red phosphor used in a television set, cathode ray tube (CRT) displays and in LEDs [22]. It is also used in a various medical applications. Yttrium-90, a radioactive isotope is used in a treatment for cancers [23]. It is also used in to make yttrium on garnets for microwaves filters and in devices such as satellites [24].

1.5 RE luminescence

The RE ions of trivalent or divalent charge states are luminescence activators in a phosphor materials. The RE's are valued for their important properties since energy and electron transfer between these states influence the efficiency of materials and stability. The optical transition of the RE luminescence is related to the $4f^N$ or $4f^{(N-1)}5d$ states [25]. These states showed properties for the development of phosphors for application in field emission and plasma displays. The atomic structure of transition metal ions of the iron group is shown in Figure 1.1. Xe core, an unfilled 4f shell and some outer shells that screen the 4f shell from outside influences are the characterization of all lanthanides ions.



- 3d shell strongly affected by host ions
- Free ion $2^{S+1} \Gamma$ states split into $S^{+1} \Gamma(X)$ multiplets
- Broad spectral lines, small cross sections

Figure 1.1: Transition metal ion atomic structure of RE's

1.5.1 d-f transition (Eu^{2+})

The divalent europium (Eu^{2+}), similarly to trivalent Eu^{3+} is the most well-known applied example of RE ions. RE ions have an outer most electron configuration of $4f^n$ [26]. The transition of $4f^n \rightarrow 4f^{(n-1)}5d$ for divalent RE ions is possible to occur in the optical range. It gives a very intense and a broad emission and a broad absorption bands. The emission bands of Eu^{2+} are usually broad due to $f-d$ transitions [27]. The position of the emission bands wavelength is depending on the host material. It can change from the near UV to the red, this is due to the crystal field splitting of the $5d$ level, as shown in figure 1.2 [28]. The emission bands shift to a longer wavelength when increasing the crystal field strength.

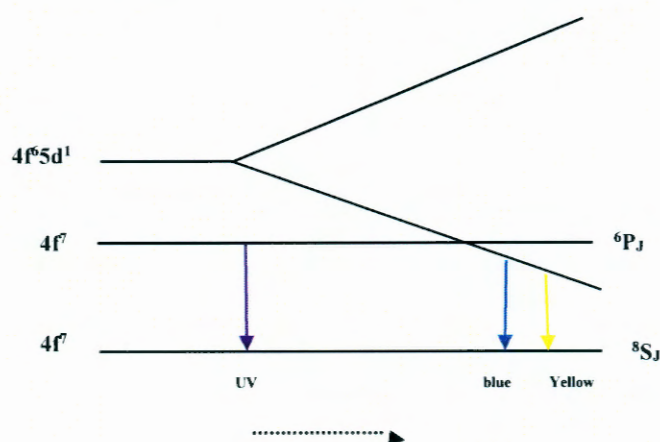


Figure 1.2: Schematic diagram of the energies of $4f^7$ and $4f^6 5d^1$ levels in Eu^{2+} influenced by crystal field Δ [29]

1.5.2 h-f transition (Dy^{3+})

Dy^{3+} emits in two spectral regions: 470 to 500-nm region due to the ${}^4F_{9/2} \rightarrow {}^6H_{15/2}$ transition and 570 to 600-nm region due to the ${}^6F_{15/2} \rightarrow {}^6F_{13/2}$ transition [30]. However, the direct UV excitation of this ion is not effective due to the relatively large energy of both the charge transfer as well as the $4f^8 5d^1$ states. Excitation by means of host complex ions may be achievable by an energy transfer process [31].

1.6 Structural characteristics of vanadates host

Vanadates show an efficient and broad emission which are due to the charge transfer (CT) of an electron from the oxygen $2p$ orbital to the vacant $3d$ orbital of V^{5+} in tetrahedral VO_4 with T_d symmetry.

1.6.1 Crystal structure of zinc vanadate ($\text{Zn}_2\text{O}_2\text{V}_7$)

$\text{Zn}_2\text{V}_2\text{O}_7$ has a monoclinic with lattice parameters $a = 7.429 \text{ \AA}$, $b = 8.340 \text{ \AA}$, $c = 10.098 \text{ \AA}$ and $\beta = 111.37^\circ$, $V = 582.63 \text{ \AA}^3$ [32]. Structural unit cell with space group $c1\ 2/c1$, and Zn^{2+} and V^{5+} cations are surrounded by various quantitative of oxygen. The Zn ions are coordinated to five oxygen atoms with Zn-O bonds ranging from 1.973 to 2.088 \AA . The anion consists of a pair of VO, tetrahedra sharing an oxygen atom which lies on a two-fold axis. A schematic of a crystal structure of $\text{Zn}_2\text{V}_2\text{O}_7$ obtained from (-100) direction is presented in Figure 1.3.

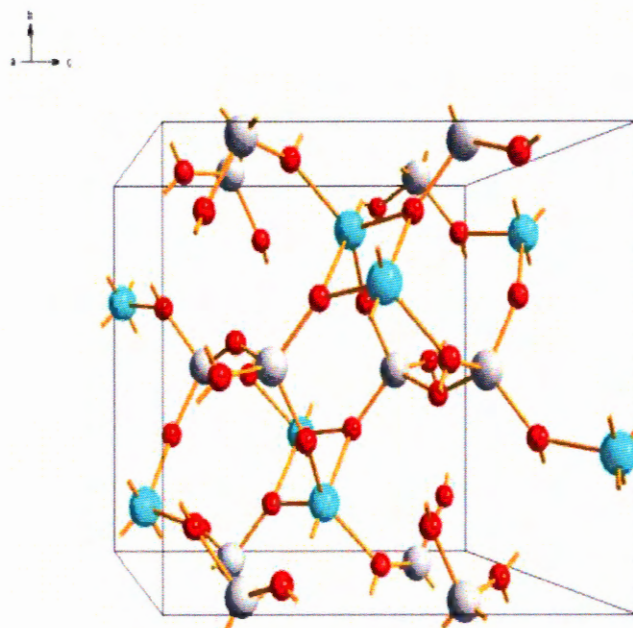


Figure 1.3: The schematic crystal structure of monoclinic $\text{Zn}_2\text{V}_2\text{O}_7$.

1.6.2 Crystal structure of Yttrium vanadate (YVO_4)

The crystal tetragonal structure of YVO_4 is a zircon type with a space group of $14_1/amd$ (141) and the cell parameters $a=b$ and c are 7.12 \AA and 6.28 \AA , respectively. YVO_4 include two kinds of polyhedral which are VO_4 tetrahedron and YV_8 polyhedron. Each vanadium site is surrounded by four oxygen atoms with atomic distance of 1.71 \AA between Vanadium and oxygen.

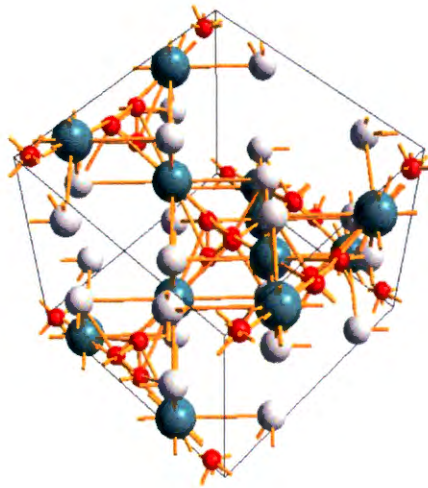


Figure 1.4: The schematic crystal structure of tetragonal YVO_4

1.7 Statement of the problem

For several years, a white LED comprising a blue-emitting LED and a yellow-emitting $\text{Y}_3\text{Al}_5\text{O}_{12}:\text{Ce}^{3+}$ phosphor has widely been used as an illumination source. However, such devices are known to have limited emission intensity in the orange/red spectral region and are characterized as cool white LED. For general lighting applications, it is essential to make devices that emit warm white light. Inorganic phosphors that emit red and yellow light are of interest for producing large-surface-area white light LED devices because of their good chemical stability. Unfortunately, the methods currently used such as solid state reaction (SSR) to make the phosphors and displays require high temperature steps, which are inconsistent with mass production and fragile plastic substrates. The discovery and development of new compounds such as vanadate for ultraviolet-excited phosphors is of great importance for the development of flat-panel displays and lighting. As there are no reliable theories to predict the relation between composition and phosphor colour and efficiency, several useful commercial phosphor materials have been discovered through one-by-one serial synthesis and testing. Our approach of using low temperature synthesis method, in contrast, offers rapid screening of many

compositions and variation of growth parameters, and it has enabled us to identify a new red and yellow phosphors, $\text{YVO}_4:\text{Eu}^{3+}$, $\text{YVO}_4:\text{Dy}^{3+}$, $\text{Zn}_2\text{V}_2\text{O}_7$ and (Ca, Ba, Sr)-doped $\text{Zn}_2\text{V}_2\text{O}_7$ phosphors, which has a material properties and efficiency comparable to those of existing commercial red and yellow phosphors.

1.8 Aim of the study

The two specific aims of the study were:

- To concentrates on the possibility of engineering the optical properties, physical, chemical, and opto-electronic properties of the vanadates. The vanadates was studied with different research techniques i.e. Scanning electron microscope (SEM) and photoluminescence spectroscopic (PL).
- To synthesis undoped and doped vanadates by using the combustion method and sol-gel method, respectively.

1.9 Research objectives

The specific objectives of the study were:

- To study the structural and luminescence properties of self-yellow emitting undoped $\text{Zn}_2\text{V}_2\text{O}_7$ and (Ca, Ba, Sr)-doped $\text{Zn}_2\text{V}_2\text{O}_7$ phosphors synthesised by combustion method
- To investigate the effect of annealing temperature on the structure and luminescence of $\text{Zn}_2\text{V}_2\text{O}_7$ prepared by sol-gel method
- To investigate the effect of urea ratio on structure and luminescence properties of $\text{YVO}_4:\text{Dy}^{3+}$ phosphors
- To study and investigate luminescence prosperities of Dy^{3+} -doped YVO_4 phosphor prepared by combustion method.
- To optimize deposition time to enhance photoluminescence properties of laser-ablated red Eu^{3+} doped YVO_4 thin films.
- To study the Effect of substrate temperature on structure and luminescence properties of $\text{YVO}_4:\text{Eu}$ thin films grown by PLD.

1.10 Thesis layout

The thesis is organized into nine chapters. The summary of each chapter is provided below: Chapter 1 gives the introduction to phosphor and the theoretical basis of the luminescence phenomenon. A short introduction to vanadates is given followed by a summary of physical principle involved in the luminescence process.

Chapter 2 comprises with two parts. The first part gives the description of the synthesis procedures that was used in this work which are combustion method and sol-gel process. The other part gives the relevant characterization techniques that were employed in this study.

In chapter 3 the structural and the luminescence properties of doped and undoped zinc vanadate are investigated. The discussion on structural properties when compared to both doped and undoped zinc vanadate material is given.

Chapter 4 gives the discussion on the effect of annealing temperature on luminescence of zinc vanadated. A discussion on the thermal properties based on DSC and TGA is also given.

Chapter 5 considers the characterization of the Dysprosium doped yttrium vanadate phosphor, which was synthesized by combustion method. The morphology, grain size and structural characterization were presented.

In chapter 6 the amount of urea (NH_2CONH_2) was introduced as a fuel because of its effectiveness in an exothermic reaction. The behaviour of the urea:nitrate ratio on the structure and luminescence properties $\text{YVO}_4:\text{Dy}^{3+}$ phosphor was investigated.

Chapter 7 gives the investigation of the change in the crystalline structure on the yttrium vanadate doped europium thin films phosphor. The substrate temperature was varied and the oxygen pressure was also varied.

To enhanced photoluminescence properties of laser-ablated of the yttrium vanadate doped with europium, the deposition time was optimised. Chapter 8 gives the discussion of changing the deposition time on luminescence and structural properties.

Chapter 9 gives the summary of the study of this thesis.

References

- [1] G. F. J. Garlick, IOPscience 1949 Rep. Prog. Phys. 12. 34
- [2] J. A. Wani, N. S. Dhoble, N. S. Kokode, S. J. Dhoble, Adv. Mat. Lett., **5(8)**(2014) 459-464.
- [3] Y. Muramoto, M. Kimura and S. N. Semicond, Sci. Technol. 29 (2014) 084004-1-8
- [4] J. Zhou, F. Huang, Ju Xu, H. Chen and Y. Wang, J. Mater. Chem. C, **3** (2015) 3023-3028.
- [5] Y. Huang, Y. Moon Yu, T. Tsuboi, H. Jin Seo, Optics Express, 20 (4) (2012) 4360-4368.
- [6] E. Newton Harvey, A history of Luminescence volume 44.
- [7] R. Chen, D. J. Lockwood, J. of The Electrochemical Society, **149 (9)** (2002) s67-s78.
- [8] K. N. Shinde, J Material Sci Eng, 3(3) (2014), <http://dx.doi.org/10.4172/2169-0022.S1.017>.
- [9] P. F. Smet, A. B. Parmentier and D. Poelman, J. Electrochem. Socie, **158** (2011) R37-R54.
- [10] H. H. Yu, H. J. Zhang, J. Y. Wang, Acta Physica Polonica A, **124** (2013) 301-304.
- [11] T. Schlieper, W. Milius, W. Schnick, Z. Anorg. Allg. Chem. **621** (1995) 1380-1384.
- [12] B. Geijer, Annalen fur die Freunde der Naturlehre 9 (1788) 229-230.
- [13] W. H. Brock, The Norton History of Chemistry (1st ed. W.W. Norton & Company, 1993).
- [14] A. J. Kenyon, Progress in Quantum Electronics, **26** (2002) 225–284.
- [15] S. Gai, C. Li, P. Yang, and J. Lin, Chem. Rev. **114** (2014) 2343–2389.
- [16] P. X. Gao, Y. Ding, Z. L. Wang, Nano. Lett. **3** (2003) 1315–1320.
- [17] W. Liu, L. S. Gu, D. L. Ye, S. M. Zhu, S. M. Liu, X. Zhou, R. Zhang, Y. Shi, Y. Hang, C. L. Zhang, Appl. Phys. Lett. **88** (2006) 092101-1-4.
- [18] F. Szabadvary, Handbook on the physics and chemistry of rare earths, **11** (1988) 33-80.
- [19] P. Thyssen, K. Binnemans, Handbook on the Physics and Chemistry of Rare Earths, **41** (2011) 1–93.

- [20] J. Wanga, Y. Xua, M. Hojamberdieva, Y. Cui, H. Liu, G. Zhua, *J. Alloy. Comp*, **479** (2009) 772–776.
- [21] C. W. Gehrke, R. L. Wixom, E. Bayer, *J. Chromato. Library*, **64** (2001) 99–599.
- [22] C. Lo, J. Duh, B. Chiou, C. I. Peng, L. Ozaw, *Mater. Chem. Phys*, **71(2)** (2001) 179–189.
- [23] D. P. Al-Adra, R. S. Gill, S. J. Axford, X. Shi, N. Kneteman, S.-S. Liau, *European J. of Surgical Oncology (EJSO)*, **41** (2015) 120–127.
- [24] R. Nazlan, M. Hashim, I. R. Ibrahim, F. M. Idris, I. Ismail, W. N. Wan Ab Rahman, N. H. Abdullah, M. M. M. Zulkimi, M. S. Mustaffa, *J. of Physics and Chemistry of Solids*, **85** (7522) (2015) 1-12.
- [25] V. B. Pawade, N. S. Dhoble, S. J. Dhoble, *J. of Rare Earths*, **32(7)** (2014) 593-597.
- [26] J. Krupa, N. A. Kulagin, *Physics of laser crystals, NATO Science Series, II, Mathematics, Physics and Chemistry*, 126 (2003) 166.
- [27] F. B. Dejene, D. B. Bem, H. C. Swart, *J. Rare. Earth*, **28** (2010) 272-276.
- [28] Y. Gu, Q. Zhang, Y. Li, H. Wang, *J. of Physics: Conference Series*, 152, (2009) 012083-1-5.
- [29] W. M. Yen, S. Shionoya, H. Yamamoto, *phosphor handbook*, ISBN 0-8494-3564-7, page 207.
- [30] Lin, Y. Tang, Z. Zhang, Z. Nan, *C.W. Appl. Phys. Lett.*, **81** (2002) 996-998.
- [31] N. Suriyamurthy, B. S. Panigrahi, *J. Lumin.*, **128** (2008) 1809-1814.
- [32] S. P. Kuang, Y. Meng, J. Lui, Z. C. Wu and L. S. Zhao, *Optik*, **124** (2013) 5517-5519.

Synthesis and characterization technique

2.1 Introduction

Nanomaterials have been proved to be one of the most attractive and promising technological development in this field. The physical and chemical properties of the materials at nanomaterials scale are of interest and important for technological applications. Nanostructured materials often exhibit different properties when compared to other materials. To synthesize the crystalline materials at nanometre scale with controlled size and composition, combustion and sol gel route was used and also the pulse laser deposition was used to prepare the thin films of these nanomaterials [1, 2].

Characterizing particle or feature size for nanocrystals and nanostructures is done routinely using scanning electron microscopy (SEM) and atomic force microscopy (AFM). The advantage of SEM and AFM methods is that they can be used to study the morphology of prepared nanoparticles. For a complete picture of the crystal phase, average particle diameter, particle size can be obtained from X-ray diffraction (XRD). The complete characterization of a whole material requires elemental analysis, which is often performed in an electron microscope using energy-dispersive spectrometry (EDS). Elemental and qualitative analytical techniques are also necessary to identify intentional adsorbates or unintentional contaminants on a particle surface. Molecular spectroscopy Fourier transform infrared (FTIR) spectroscopy can characterize materials and help identify any surface contaminants. Emission and excitation is very important for luminescence properties. Luminescence spectra, lifetimes, and quantum efficiency measurements can be made with the Photoluminescence (PL).

2.2 Sol-gel method

Sol-gel method is a wet chemical technique to produce metal oxide nanoparticles through chemical process hydrolysis, gelation, followed by drying and thermal treatment. It is define as a stable dispersion of colloidal particles or polymers in a solvent. The metal alkoxide are used as reactive metal precursors and are hydrolysed with water during the sol-gel process.

The homogenous gels can be produced from the mixture of alkoxides through the hydrolysis process and gelation. After gelation, the precipitation is washed, dried and then undergoes a

sintering temperature to obtain a crystalline nanoparticle. For sol-gel method, the annealing procedure (temperature and time) is the key step in the preparation process, which can seriously determine the quality of the samples. It should be noted that, although the sol-gel method can be used for large-scale production and the product usually offers high luminescence intensity due to the high crystallinity formed at high annealing temperature, the sol-gel derived nanocrystals generally have broad particle size distribution, irregular morphology, and are insoluble in water, which compose the shortcomings of this method. Sol-gel method has advantages over other methods like: short annealing time, lower processing temperature, good control of the size and shape of particles.

2.2.1 Synthesis of $Zn_2V_2O_7$ by Sol-gel method

The schematic experimental procedure of $Zn_2V_2O_7$ is shown in figure 2.1. Zinc nitrate ($Zn(NO_3)_2 \cdot 6H_2O$), ammonium metavanadate (NH_4VO_3) and citric acid ($C_6H_8O_7$) were used as starting materials and were dissolved in 10 ml of deionised water. The yellow colour solution was heated at 80 °C while stirring.

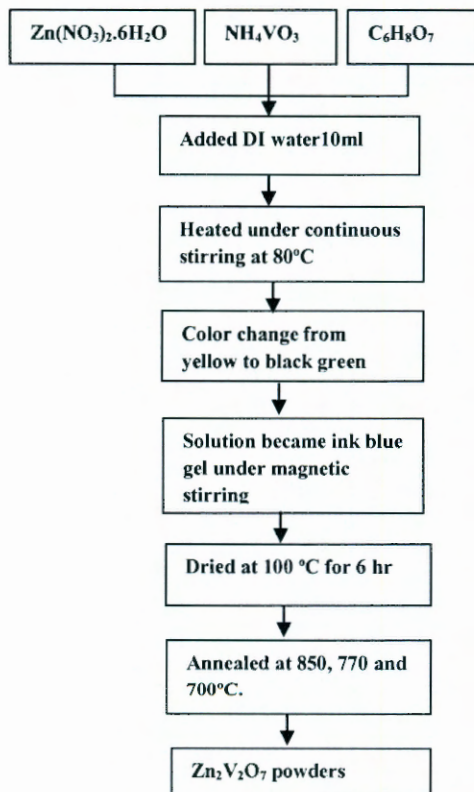


Fig. 2.1: Schematic diagram of $Zn_2V_2O_7$ prepared by the sol-gel method.

Solution changed from yellow to a black green colour and then to a blue ink gel under a magnetic stirring. The final green gel solution was observed. The green gel was then dried in an oven at 100 °C for 6 hrs and annealed at 700-850°C for 2 hours.

2.3 Combustion method

The combustion method is one of the ideal techniques, because an exothermic reaction is initiated at the ignition temperature and it generates heat. It has been used into the production of various materials like ceramic powders for a variety of advanced applications. Combustion method can be prepared by combining the metal nitrates and the fuel in an aqueous solution. Glycine and urea serve as fuels for the synthesis of nanocrystalline metal oxide. The process involves a self-sustained reaction in homogenous solution of different oxidizers. When the mixture of fuel and oxidizer is heated, the mixture grows into frothy foam which may occupy the entire reaction vessel and then gets self-ignited followed by combustion [3]. The advantages of combustion method are that it is effective, simple and rapid process.

2.3.1 Synthesis of undoped $Zn_2V_2O_7$ and (Ca, Ba, Sr)-doped $Zn_2V_2O_7$ powders by Combustion method.

The $Zn_2V_2O_7$ powders were synthesized by the combustion method by varying the initial temperature. Zn nitrate hexahydrate ($Zn(NO_3)_2 \cdot 6H_2O$), ammonium metavanadates (NH_4VO_3), $Ba(NO_3)_2$, $Sr(NO_3)_2$ and $Ca(NO_3)_2$ were used as starting materials. Urea ($(NH_2)_2CO$), was added as a fuel. Stoichiometric amounts of materials of undoped samples were mixed by grinding in an agate mortar and the homogenous mixture was obtained. The mixture was burned in a muffle furnace at various temperatures of 500°C, 600°C and 700°C. Initially the solution boiled and underwent dehydration. Followed by decomposition with escape of large amount of gases, ten spontaneous ignitions occurred and underwent smouldering combustion with enormous swelling. The foamy powder was obtained and crushed, and the pale yellow colour powder was obtained. Then the $Zn_2V_2O_7$ sample prepared at 600°C was singly doped with Ba, Ca and Sr.

2.3.2 Synthesis of Dy³⁺ -doped YVO₄ using combustion method

YVO₄:Dy³⁺ was prepared by the combustion method. The starting materials were yttrium nitrate Y(NO₃)₃, ammonium metavanadate (NH₄VO₃), urea (NH₂CONH₄) and dysprosium nitrate Dy(NO₃)₃. The chemical reaction is as follows:



All the ingredients were mixed according to the stoichiometric ratio in an agate mortar and a pasty solution was formed. The solution was transferred to a crucible and then kept in a furnace maintained at a temperature of 600°C. A combustion process started in a few minutes and a flame was observed. The formation of a foamy powder was observed and a pale yellow powder was obtained.

2.3.3 Synthesis of urea:nitrate ratio on the structure and luminescence properties of YVO₄:Dy³⁺ phosphors by combustion method.

YVO₄:Dy³⁺ was prepared by combustion method. The starting materials were yttrium nitrate Y(NO₃)₃, ammonium metavanadate (NH₄VO₃), urea (NH₂CONH₄) and dysprosium nitrate DY(NO₃)₂. The ratio of urea:nitrate was varied from 1-4. All the ingredients were mixed according to the stoichiometric ratio in an agate mortar and a pasty solution was formed. The solution was transferred to the crucible and then kept in the furnace maintained at a temperature of 600°C. Combustion process started in a few minutes and a flame was observed. The formation of a foamy powder was observed and the pale yellow powder was obtained.

2.4 Pulse laser deposition (PLD) technique

The pulse laser deposition is a technique that uses high power laser pulses (typically ~10⁸ Wcm⁻²) to remove material from the surface of a target [4]. This material is vaporized from the target (in a plasma plume) which deposits it as a thin film on a substrate. Thin films are prepared by the ablation of targets illuminated by a focused pulsed-laser beam. In the process of laser ablation, the photons are converted first into electronic excitations and then into thermal, chemical, and mechanical energy, resulting in the rapid removal of material from a surface [5]. The process occurs in ultra-high vacuum (UHV) or in the presence of a background gas, usually oxygen, so that the deposited films are fully oxygenated. Out of

many laser sources available for PLD of films, mostly short and high energy KrF and Nd:YAG lasers are used.

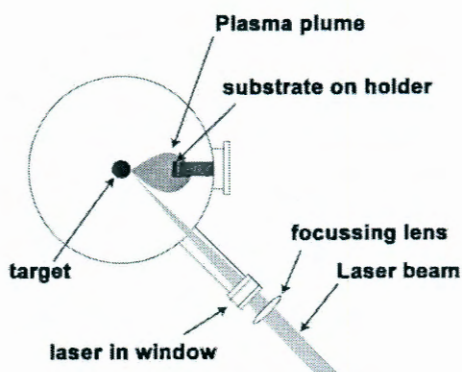


Figure 2.2: shows the schematic of the PLD setup [6]

2.4.1 Synthesis of undoped $\text{YVO}_4:\text{Eu}$ thin films grown by PLD method.

A commercial $\text{YVO}_4:\text{Eu}^{3+}$ phosphor powder was obtained from phosphor technology. $\text{YVO}_4:\text{Eu}^{3+}$ was pressed into a pellet and mounted on a rotating holder on which Si substrates were mounted for ablation. Before the deposition, the Si (100) substrates were first Ultrasonically cleaned in acetone, and ethanol then rinsed with distilled water and then dried in air. $\text{YVO}_4:\text{Eu}^{3+}$ thin films were deposited on the Si substrates with typical size of 25 x 25 mm using a frequency tripled Nd:YAG Laser. A laser pulse of 10 Hz was focused onto the rotating target and the laser energy was approximately 47 J/cm. The distance between the target and the substrate was kept constant at 45 mm during the deposition of each film. The films were deposited on Si (100) substrates. The oxygen background pressures were also varied for a series of samples deposited at 400, the oxygen pressures were varied from 20 to 50 to 72 and to 85 mTorr during deposition at the substrate temperature of 400°C.

Following the same procedure, the synthesis of Eu^{3+} doped YVO_4 deposited at different time was done by PLD. The films were deposited on Si (100) substrates at oxygen background pressures of 5 mTorr at room temperature for different deposition time of 30, 45 and 60 minutes.

2.5 Characterization techniques

2.5.1 Atomic Force Microscopy (AFM)

Electron microscopy has long been recognized as a key technique in microbiology to study the surface of the structure. AFM is a very high-resolution non-destructive tool capable of scanning probe microscopy. The measurement of an AFM is made in three dimensions, the horizontal X-Y plane and the vertical Z dimension. During the last years, AFM has been used increasingly to investigate microbial surfaces at high resolution [7]. AFM, which uses a sharp tip to probe the surface features by raster scanning, can image the surface topography with extremely high magnifications, up to 1,000,000X [8]. Resolution (magnification) at Z-direction is normally higher than X-Y. AFM imaging is performed by sensing the force between a very sharp probe and the sample surface. The force is monitored by attaching the probe to a pliable cantilever, which acts as a spring, and measuring the bending or “deflection” of the cantilever. A laser beam is focused on the free end of the cantilever, and the position of the reflected beam is detected by a position-sensitive detector (photodiode). AFM cantilevers and probes are typically made of silicon.

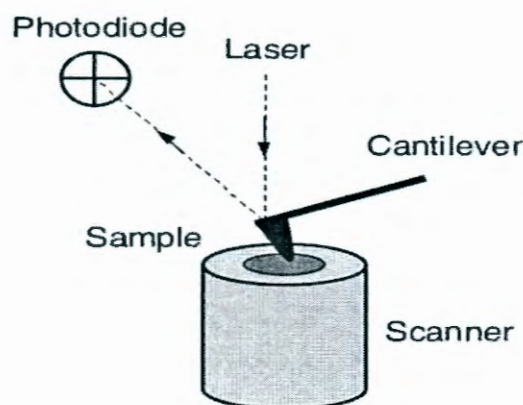


Figure 2.3: General principle of AFM

AFM has a number of imaging modes such as contact, intermittent and non-contact mode. The most useful imaging mode is the contact mode, in which sample topography can be measured in different ways. When the spring constant of cantilever is less than surface, then the cantilever bends. By maintaining a constant cantilever deflection (using the feedback loops) the force between the probe and the sample remains constant and an image of the surface is obtained. The advantage of this mode is fast scanning, good for rough samples, and

is used in friction analysis. The surface roughness of the films was analysed by a Shimadzu SPM – 96 model Atomic force microscopy (AFM).

2.5.2 Fourier Transform Infrared Spectrometer (FTIR)

The discovery of infrared light was discovered back in 19th century. Infrared absorption spectroscopy is the method which used to determine the structures of molecules with the molecules' characteristic absorption of infrared radiation. A common FTIR spectrometer consists of a source, interferometer, sample compartment, detector, amplifier, A/D convertor, and a computer. The source generates radiation which passes the sample through the interferometer and reaches the detector. Then the signal is amplified and converted to digital signal by the amplifier and analog-to-digital converter, respectively. Eventually, the signal is transferred to a computer in which Fourier transform is carried out.

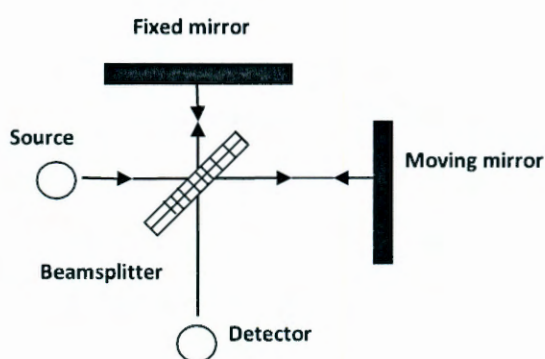


Figure 2.4: Schematic diagram of a Michelson Interferometer

Infrared absorption spectroscopy is more useful because of the fact that it is capable to analyze all gas, liquid and solid samples. The common used region for infrared absorption spectroscopy is $4000 \sim 400 \text{ cm}^{-1}$ because the absorption radiation of most organic compounds and inorganic ions is within this region [9]. The unique part of an FTIR spectrometer is the interferometer and, is used to split one beam of light into two so that the paths of the two beams are different. A Michelson interferometer consists of two mirrors and a beam splitter is shown in figure 2.4. The beam splitter transmits one half of the radiation, and reflects the other half. Both transmitted and reflected beams strike mirrors, which reflect the two beams back to the beam splitter.

2.5.3 X-ray Diffraction (XRD)

XRD is a technique used to identify phase of a crystalline material. It can use to measure the average spacing between layers and it can also measure the size and internal stress of small crystalline regions [10]. This technique consists of three basic elements: an X-ray tube, a sample holder and an X-ray detector. X-rays are generated in a cathode ray tube. When filament is heated to produce electrons, the electrons will accelerate towards the target by applying a voltage and bombarding the target materials. XRD is widely used for the identification of the unknown crystalline materials. It can be used to determine the unit cell dimensions, sample purity, crystal structure etc.

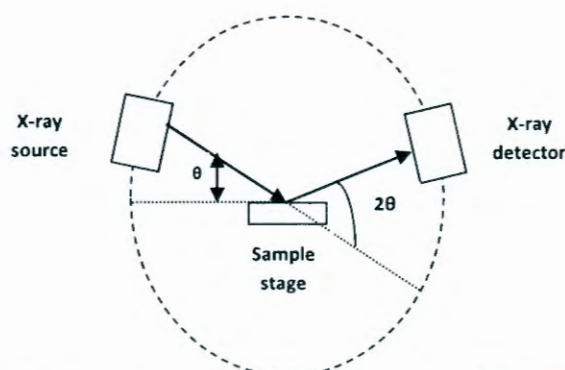


Figure 2.5: shows the schematic of the XRD setup

If the crystallites of the powder are very small, the peaks of the pattern will be broadened. From this broadening it is possible to determine an average crystallite size by the Debye–Scherer equation.

$$d = \frac{k\lambda}{\cos\theta \sqrt{\beta^2 \beta_0^2}} \quad (2)$$

where d denotes the average size of the crystallites, k is a factor which is usually set to 0.9, λ is the x-ray radiation wavelength, θ is the Bragg angle, β is the broadening of the diffraction line measured at half of its maximum intensity (radians), and β_0 represents the scan aperture of the diffractometer. D8 advanced AXS GmbH X-ray diffractometer was used in this study. The XRD patterns were conducted using a Bruker AXS Discover Model diffractometer with $\text{CuK}\alpha$ (1.5418Å) radiation.

2.5.4 Thermogravimetric Analysis (TGA)

TGA is the most widely used thermal method. TGA is a technique in which the mass of a substance is monitored as a function of temperature or time as the sample specimen. It is a technique that controls the temperature programme in a controlled atmosphere. TGA consist of a sample pan hanging from the balance or located above the balance on the sample stem. This pan resides in a furnace and it is heated or cooled during the experiment and the sample mass is monitored during the experiment. TGA can be used to quantify the loss of water, loss of solvent, decarboxylation, pyrolysis, decomposition, oxidation, weight % filler, amount of metallic catalytic residue remaining on carbon nanotube and weight % ash [11]. These quantifiable applications are usually done upon heating. TGA spectrums were done using the Perkin Elmer TGA7 thermogravimetric analyser, under nitrogen atmosphere at a flow rate of 20 ml.min⁻¹.

2.5.5 Differential Scanning Calorimetry (DSC)

DSC is a technique in which the difference in the amount of heat required to increase the temperature of a sample and a reference. The heat capacity is defined over the range of temperatures that are scanned. DSC can also give information about thermodynamic properties of phase changes, glass transitions, crystallization, melting oxidation stability and product stability [12]. For a sample to undergo a physical transformation, the heat must flow whether the process is exothermic or endothermic. The sample will undergo a phase transition or a thermal decomposition. An exothermic or endothermic process in the sample results in a deviation between the two heat flows and results in a peak in the DSC curve. The process of DSC can be carried out under the oxygen and other atmospheres such as gas [13]. Analysis of samples were carried out under nitrogen atmosphere (20 ml min⁻¹) using a Perkin Elmer Pyris-1 differential scanning calorimeter.

2.5.6 Scanning Electron Microscopy (SEM) and Energy Dispersive Spectrometer (EDS)

SEM is a technique that generates a verity of signal at the surface by focusing a beam of high energy electrons. The beam is collimated by electromagnetic condenser lenses, focused by an objective lens, and then scanned by electromagnetic deflection coils across the surface of the sample. Primary imaging method is collecting secondary electrons that are released by the sample. Materials that produce flashes of light from the electrons are detected. The detected

flash light can be amplified by a photomultiplier tube. The image can be formed by correlating the sample scan position with the resulting signal.

X-rays are also produced by the interaction of electrons with the sample. These x-rays are characteristic of the elements present in the sample and can be detected in a SEM coupled with an x-ray analyzer such as the EDS. The morphology was examined by JSM-7800F field emission SEM coupled with an EDS for elemental composition analysis.

2.5.7 Photoluminescence (PL)

PL spectroscopy is a non-destructive method to probe the electronic structure of materials. It is used to characterize a variety of material parameters. The light emitted in PL can be collected and analyzed to yield information about the photoexcited materials [14]. The PL spectrum provides the transition energies, which can be used to determine the electronic energy levels. The emission spectrum of PL can be used to identify the surface, interface and the impurity levels [15]. Intensity of the PL signals provides the information on the quality of the surface and interface.

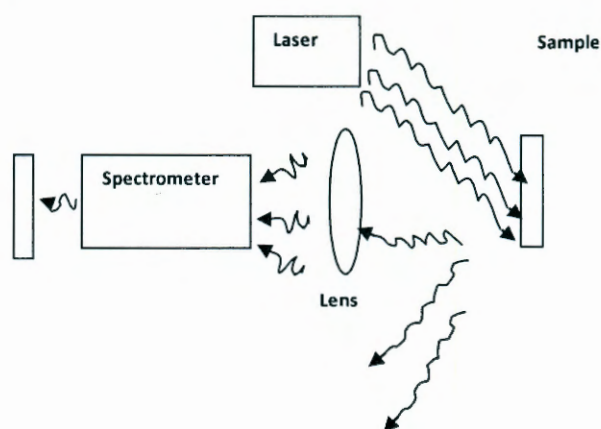


Figure 2.6: Typical experimental set-up for PL measurements

Variation of the PL intensity with external parameters like, temperature and applied voltage can be used to characterize further the underlying electronic states and bands. It is an important technique for obtaining detailed information about the nature of the state, since this state lie near the surface and interfaces.

In this study the Cary Eclipse PL spectrophotometer with a 150W xenon lamp as the excitation source was used.

References

- [1] M. Niederberber, *Acc. Chem. Res.* **40** (2007) 793–800.
- [2] B. Huang, Min-hua Cao, Fu-de Nie, H. Huang, Chang-wen Hu, *Defence Technology*, **9** (2013) 59–79.
- [3] S. T. Aruna, A. S. Mukasyan, *Current Opinion in Solid State and Materials Science*, **12** (2008) 44–50.
- [4] N. Kumar, S. Dash, A. K. Tyagi and B. R. Sadhan, *Indian Academy of Sciences*, **35** (2010) 493–511.
- [5] T. Lippert, *Adv Polym Sci*, **168** (2004) 51–246.
- [6] K. Tanaka, Y. Inoue, S. Okamoto, K. Kobayishi and K. Takizawa, *Jpn. J. Appl. Phys.*, **38** (1997) 3517-3521.
- [7] L. S. Dorobantua, G. G. Goss, E. Robert, *Burrell Micron*, **43** (2012) 1312–1322.
- [8] H. G. Oral, Z. Parlak, F. L. Degertekin, *Ultramicroscopy*, **120** (2012) 56-63.
- [9] M. Cornac, A. Janin, J. C. Lavalley, *Infrared Physics*, **24** (1984) 143–150.
- [10] S. J. S. Qazi, A. R. Rennie, J. K. Cockcroft, M. Vickers, *Journal of Colloid and Interface Science*, **338** (2009) 105–110.
- [11] S. W. Carvalho, T. J. Oliveira, C. R. Cardoso, C. H. Ataíde, *chemical engineering research and design*, **9** (2015) 337–345.
- [12] D. Gao and T. Deng, *Materials and processes for energy: communicating current research and technological developments* (A. Méndez-Vilas, Ed.). 32-44
- [13] D. Shen, J. Hu, R. Xiao, H. Zhang, S. Li, S. Gu, **130** (2013) 449–456.
- [14] Kengo Suzuki, *Nature Photonics*, **5** (2011) 247-314.
- [15] V. Sh. Yalishev, Y. S. Kim, X. L. Deng, B. H. Park, and Sh. U. Yuldashev, *Journal of Applied Physical*, **112** (2012) 013528-1-8.

Structural and luminescence properties of self-yellow emitting undoped $Zn_2V_2O_7$ and (Ca, Ba, Sr)-doped $Zn_2V_2O_7$ phosphors synthesised by combustion method

3.1 Introduction

Development of phosphor materials has been accelerated with the expansion of lighting and display applications as well as the progress on material science [1]. Lately light emitting device (LED) has been attracted many attention because of its success as a new light source to the incandescent lamp and fluorescent [2]. Through continuous efforts for improving efficiency and stability, YAG:Ce³⁺ phosphor that emit yellow light are utilized for white light. The combination of the blue light from the LED and the yellow light from the YAG:Ce³⁺ results in white light. However, this system lacks thermal stability at higher temperatures above 150°C. Also, the resultant white light exhibits low color rendering index (Ra) due to lack of individual blue, red and green region colors [3–5]. Therefore single-host broad band emitting phosphors need to be developed for low-cost W-LEDs with improved chemical and thermal stability better reproducibility and a simpler fabrication process [6, 7]. Vanadates (vanadium oxide) base materials such as $Zn_3V_2O_8$, C_5VO_3 have attracted special attention due to their unique structural and optical properties which might render a possible substitute in near future. These vanadates show an efficient and broad emission from 400 to 700 nm and are due to the charge transfer (CT) of an electron from the oxygen 2p orbital to the vacant 3d orbital of V⁵⁺ in tetrahedral VO₄ with T_d symmetry [8-10]. These materials are self-activated phosphors and they have several advantage, e.g. comparing with the rare-earth doped phosphors, vanadate self-activated phosphors are cheaper [11]. Many Zn vanadates were synthesized by sol gel method [12], hydrothermal method [13], Solid state method [14], etc. However, these methods have several disadvantages: In homogeneity, impure structure, irregular morphology, large particle size with broad particle size distribution, poor control of stoichiometry, longer period of synthesis and calcination, and followed by extended grinding. Therefore, a simple, fast and cheap process is still needed for the large scale production of such materials. In this work, materials with high purity better homogeneity and good particle distribution were achieved by the combustion process [15].

Combustion synthesis is one of the simplest powder preparation processes in which chemical reaction between fuel and metal nitrates converts the metal ions to the target materials. Motivated by the broadband emission of $Zn_3(VO_4)_2$ phosphor, herein, the structural, morphological, and photoluminescence characterization of undoped and Ca, Ba and Sr doped $Zn_2V_2O_7$ synthesized via the combustion method has been investigated. Other researchers, firstly Lintel *et al* [16] prepared Zn vanadates by using combustion method. From their results they obtained that the XRD structure was not single phase at a low synthesis temperature and that the best luminescent intensity was obtained for samples synthesised at 750°C. Secondly Kuang *et al* [17] reported that there is urgent need to search for new green and red phosphors or a new yellow phosphor with high efficiency, low cost, no environmental hazards. Following their footsteps [17] the ZnVO nano phosphor doped with the different dopands were investigated for the first time according to our knowledge, we have synthesized Zn vanadates by combustion method. In contrast to their findings it was found that the XRD structure obtained was single phase at low and higher synthesis temperature and the best luminescent intensity was obtained for samples synthesized at 600°C.

3.2 Results and discussion

3.2.1 X-ray diffraction and structural results

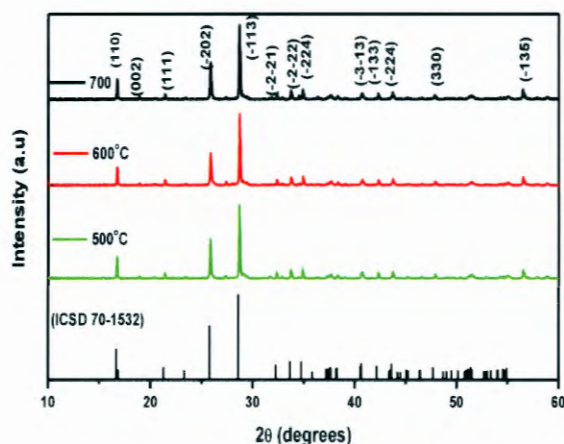


Figure 3.1: XRD patterns of $Zn_2V_2O_7$ phosphor prepared at different synthesis combustion temperature.

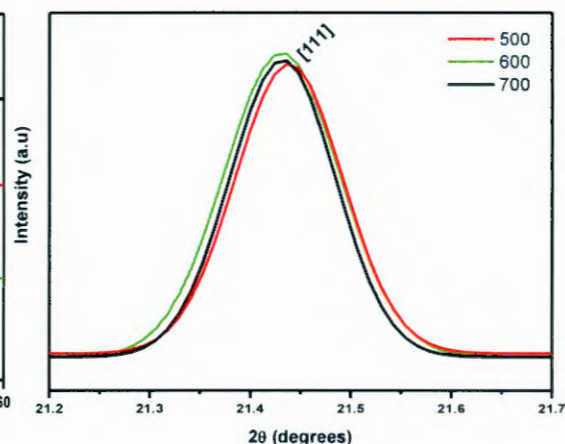


Figure 3.2: XRD powder diffraction of (111) peak for $Zn_2V_2O_7$ phosphor prepared at different synthesis combustion temperature.

Figure 3.1 shows the X-ray diffraction patterns of the samples synthesized at different initiating combustion temperatures of 500, 600 and 700°C. The phosphors products can be indexed with the monoclinic structure of $Zn_2V_2O_7$ phosphor (ICSD 70-1532). As can be seen, there is no significant change among all the phases of the products and no impurity phases were observed. From figure 3.2, it clearly seen that by drawing the XRD orientation of (111) peak no effect on XRD intensity and also on the diffraction angle was observed by varying the synthesis temperature. The average particles size was obtained from the measured half width of the Bragg reflection using the Scherrer formula [18]. There was no effect observed on estimated average particle size as it was found to be 78 nm when varying the synthesis temperature. Luitel or other research observed that at a very low synthesis temperature between 500 and 600°C the structure of their materials was $Zn_2V_2O_7$ and when the synthesis temperatures was increased further to 750°C a pure $Zn_3V_2O_8$ phase was also observed [16]. Other researchers reported the same behaviour that the structure of the materials changed with an increase in synthesis temperature [19]. In contrast to our work that showed that there is no change on the structure of the $Zn_2V_2O_7$ with the synthesis temperature increase.

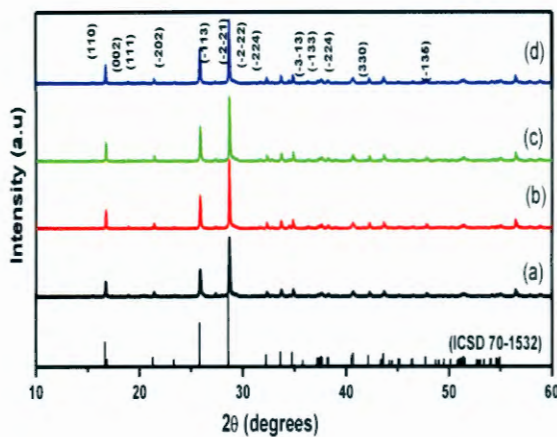


Figure 3.3: XRD patterns of the products of (a) undoped $Zn_2V_2O_7$ phosphor and $Zn_2V_2O_7$ doped with (b) Ba, (c) Ca and (d) Sr.

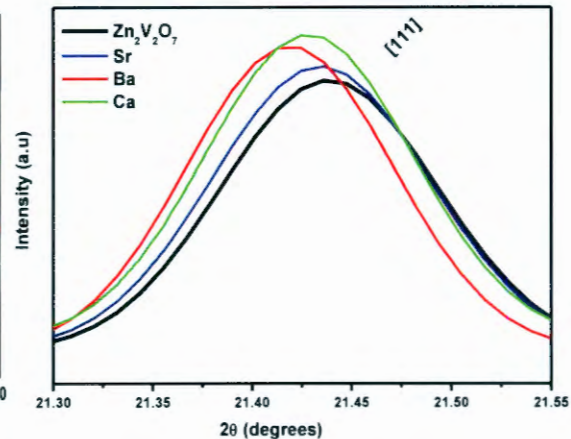


Figure 3.4: XRD powder diffraction patterns of (111) for $Zn_2V_2O_7$ phosphor doped with Ba, Ca and Sr.

Figure 3.3 shows the XRD patterns of $Zn_2V_2O_7$ doped with the different dopants (Ca, Ba, Sr) synthesized by combustion method. All the samples were synthesized at 600°C. From the figure it is clear that no impurities or secondary phases were observed by adding the different dopants to $Zn_2V_2O_7$. This may be due to the small ionic radii of the dopants compared to the

host, indicating that the dopant ions were well incorporated into the lattice sites of Zn^{2+} and lead to the increase in inter atomic distance [20]. The estimated grain size of the host $Zn_2V_2O_7$ and $Zn_2V_2O_7$ doped with (Ca, Ba, Sr) were 87, 79, 81 and 85 nm respectively. It's clear that the estimated grain size decreased slightly as compare to the host $Zn_2V_2O_7$.

In figure 3.4 the (111) diffraction peak for the undoped and doped samples are shown, it can be seen that the diffraction angle shifted compared to the undoped sample and the diffraction width became broader with the addition of the different dopants. The shift towards the lower angle indicate that the increase in d spacing due to substitution of lattice site by ions of higher radius [21]. All peaks were indexed to the monoclinic structure with the lattice parameters $a = 7.429\text{\AA}$, $b = 8.340\text{\AA}$, $c = 10.098\text{\AA}$ and $\beta = 111.37^\circ$, $V = 582.63\text{\AA}^3$ [17]. A schematic of a crystal structure of $Zn_2V_2O_7$ obtained from (-100) direction is presented in figure 3.5. $Zn_2V_2O_7$ has a monoclinic structure unit cell with space group $c1\ 2/c1$, and Zn^{2+} and V^{5+} cations are surrounded by various quantitative of oxygen.

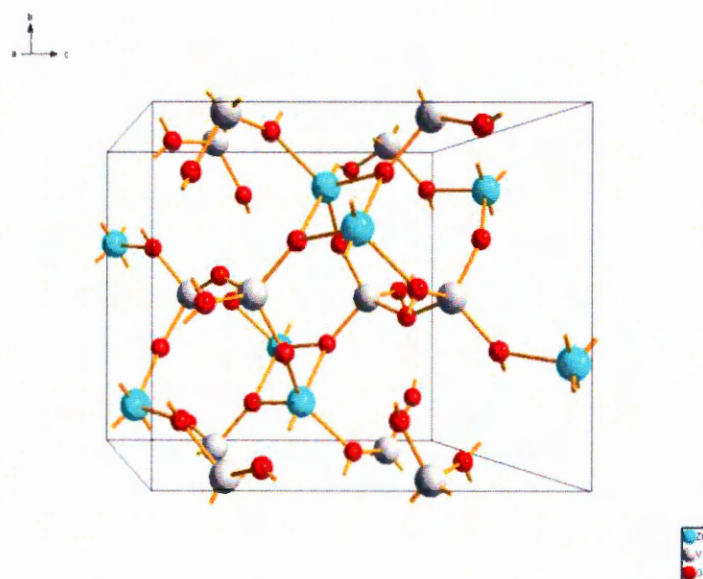


Figure 3.5: The schematic crystal structure of monoclinic $Zn_2V_2O_7$.

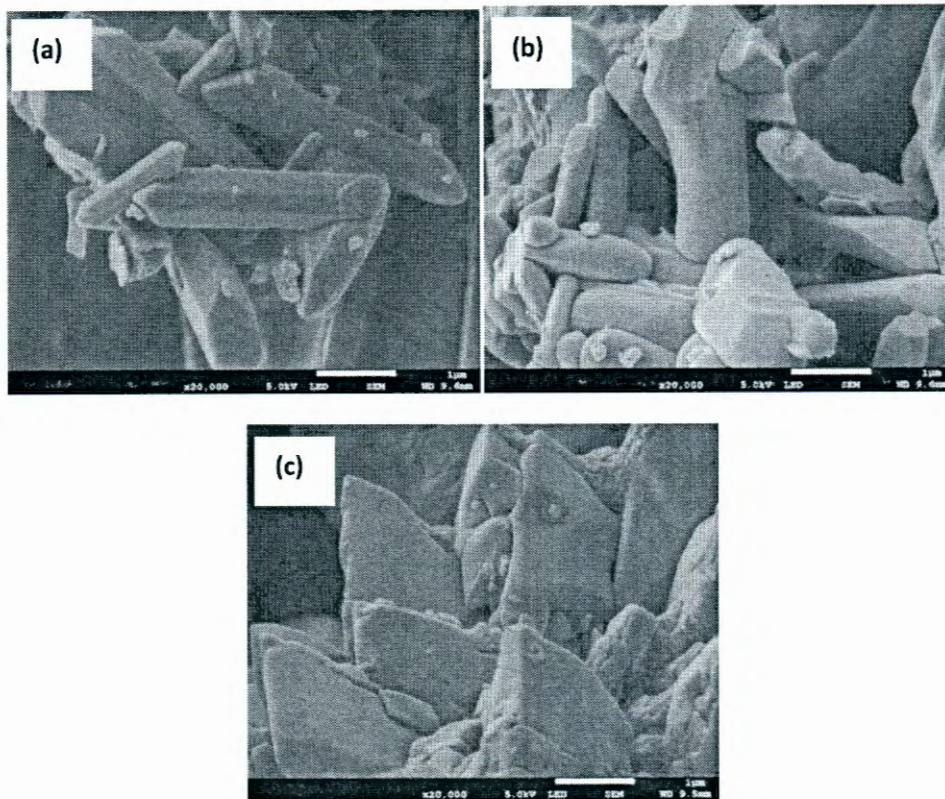


Figure 3.6: SEM micrographs of $Zn_2V_2O_7$ (a) 500, (b) 600 and (c) 700 °C at higher magnification.

3.2.2 SEM results

Figure 3.6 shows the SEM micrographs of the phosphor prepared at different temperatures by combustion method. As can be seen from figure 3.6(a) the image prepared at lower temperatures shows the particles with a hexagonal-like shape. As the temperature was increased to 600°C the microstructure has the mixture of hexagonal and irregular shape particles and those hexagonal shape decreases in size. By increasing the temperature further the original shape of the particles were destroyed at the higher temperature of 700°C, which might be due to the melting of the particles as seen in figure 3.6(c). It is noted that by increasing the synthesis temperature that the hexagonal shape change to irregular particles and the irregular particles increases in size with an increasing synthesis temperature.

Luitel observed the same behaviour where the flakes like particles were destroyed due to the increase in synthesis temperature but when synthesized using hydrothermal method [16]. They said this change in the shape of flakes like particles maybe due to melting of the flakes as seen at higher temperatures.

SEM images of the undoped $Zn_2V_2O_7$ and $Zn_2V_2O_7$ doped (Ba, Ca and Sr) phosphors prepared at $600^\circ C$ are shown in figure 3.7. Doping $Zn_2V_2O_7$ with Ba the shape of the hexagonal-like particles does not changed and the particle became agglomerated as shown in figure 3.7 (b). By doping $Zn_2V_2O_7$ with Ca or Sr, it can be seen that the shape of the microstructures retain its original structure and it is clear that the particle sizes decreased in size when doped, which confirms the XRD analysis of figure 3.4.

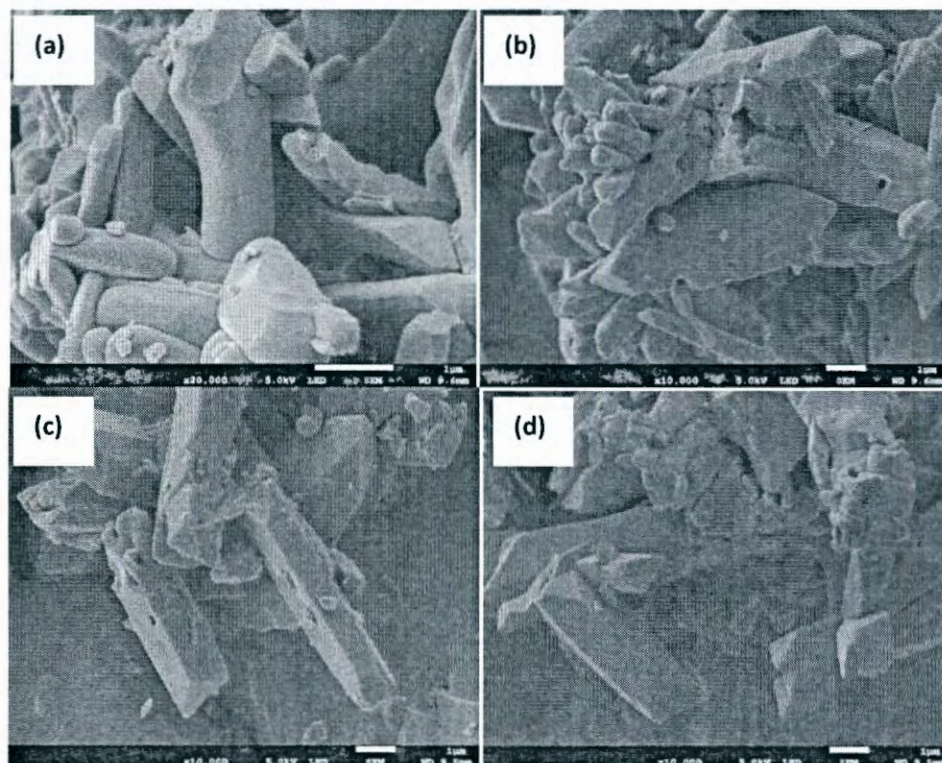


Figure 3.7: SEM micrographs of (a) $Zn_2V_2O_7$, (b) $Zn_2V_2O_7$ doped Ba, (c) $Zn_2V_2O_7$ doped Ca and (d) $Zn_2V_2O_7$ doped Sr phosphor.

3.2.3 FTIR Results

Figure 3.8 shows the FTIR spectra of the Zn vanadate. The spectra of the $Zn_2V_2O_7$ show a strong and weak absorption peak at 932 cm^{-1} due to vibration modes of the district $V=O$ units. Comparing the three IR peaks of the doped $Zn_2V_2O_7$ powders vibration bands at 1004 and 931 cm^{-1} for Ba, 1002 and 926 cm^{-1} for Ca and 1004 and 929 cm^{-1} for Sr, suggests that the distance of the $V=O$ bond for $Zn_2V_2O_7$ doped Ba is longer than that of Ca but shorter than of the Sr doped samples [22]. The broad absorption peak near 720 cm^{-1} is assigned to the antisymmetric stretching bond and the bending modes of the $V-O_b$ bond and $V-O-V$ bridges

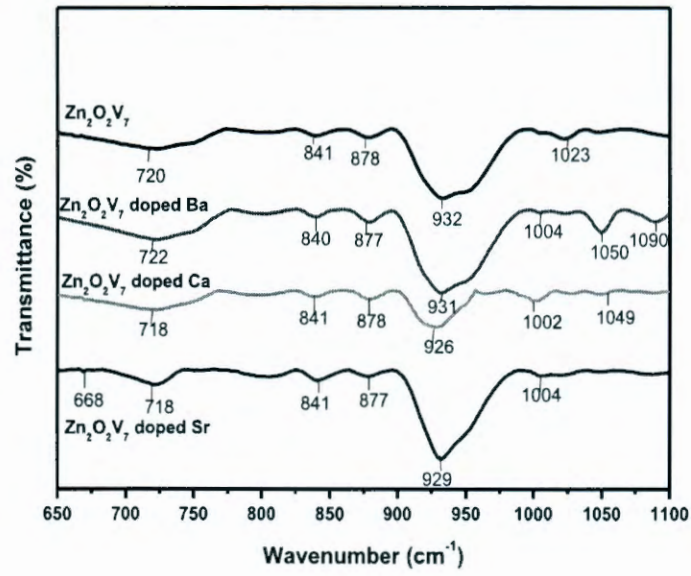


Figure 3.8: FTIR spectra of the products of undoped $Zn_2V_2O_7$ and $Zn_2V_2O_7$ doped with Ba, Ca and Sr.

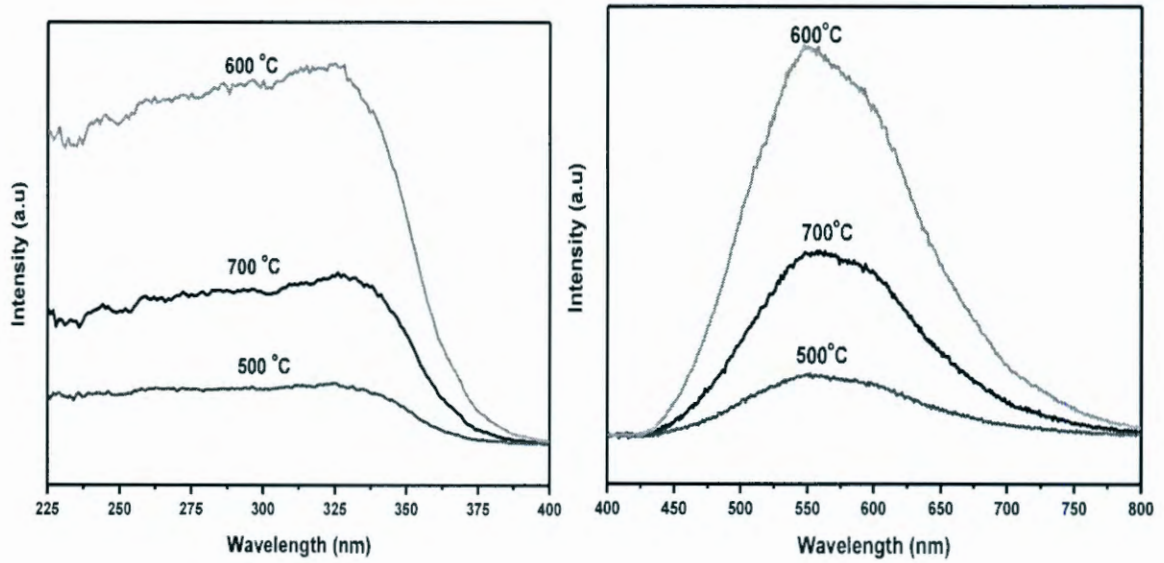


Figure 3.9: Effect of synthesis temperature on the PL (a) excitation and (b) emission intensity of $Zn_2V_2O_7$.

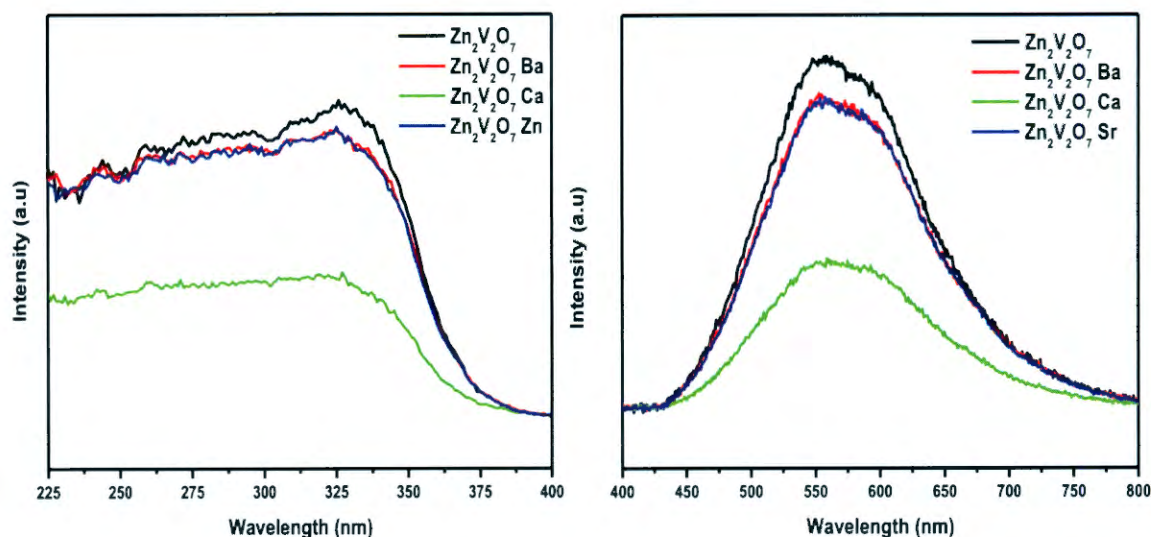


Figure 3.10: (a) PL excitation spectra of $Zn_2V_2O_7$ doped (Ba, Ca and Sr) and (b) emission spectra of $Zn_2V_2O_7$ doped (Ba, Ca and Sr).

[23]. The broad bands near 840 and 874 cm^{-1} correspond to the vanadate bonds and the broad peak at 668 cm^{-1} is assigned to the bending mode of the bridging V-O_b-V units.

3.2.4 Photoluminescence results

Figure 9(a) showed the excitation spectra of different synthesis combustion temperatures. The corresponding PL emission spectra of $Zn_2V_2O_7$ prepared at different synthesis temperature are presented in figure 9 (b). The PL of the samples shows the broad emission peak between 400 and 800 nm. The emission spectra show the broad luminescence with the maximum wavelength of 550 nm. The PL emission intensity increased with an increase in synthesis temperature and reaches a maximum at 600°C and decreased drastically when the temperature was increased to 700°C . The difference in PL intensity as a function of the synthesis combustion temperature may be attributed to the fact that at lower synthesis temperature (500°C), the lower reaction heat may lead to the incomplete reaction temperature of the raw materials. *Lui et al.* [24] prepared other phosphor materials at different synthesis temperatures, and the highest luminescence intensity was observed for a sample prepared at 600°C . It's observed that the best luminescence was due to higher synthesis combustion temperatures which may release more heat which may not be favourable for the formation of a more crystalline phosphor.

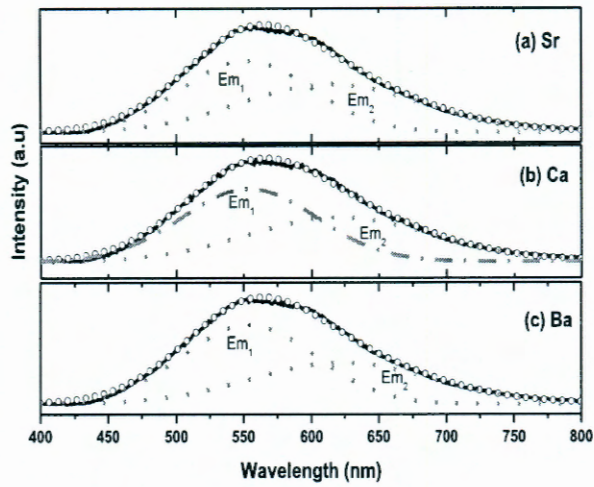


Figure 3.11: (a) PL emission spectra of $Zn_2V_2O_7$ doped (a) Sr, (b) Ca and (c) Ba. Black line indicates the emission spectra and the dotted lines are the fitted emission spectrum by two fitted with two Gaussian curves corresponding to emission bands Em1 and Em2.

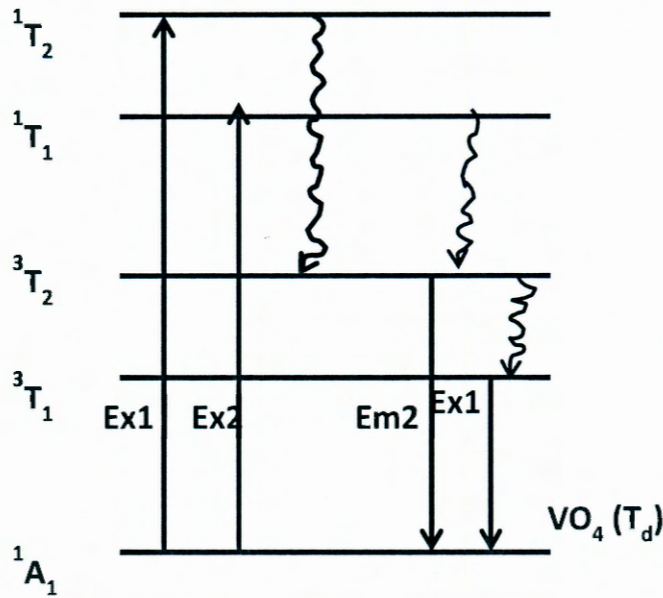


Figure 3.12: Schematic model for excitation and emission process of VO_4 tetrahedron with T_d symmetry in $Zn_2V_2O_7$.

Figure 3.10 (a) shows the excitation spectra of $Zn_2V_2O_7$ and $Zn_2V_2O_7$ doped (Ca, Ba and Sr) phosphors. The broad excitation band between 225 and 400 nm centered at around 326 nm in the excitation spectra attributed to the transition from the ground state 1A_1 to the excited

states 1T_1 [25]. The excitation band is attributed to the charge transfer (CT) from the oxygen 2p to the central vanadium ions (V^{5+}) in the VO_4 tetrahedral [26].

The emission spectra of $Zn_2V_2O_7$ and $Zn_2V_2O_7$ doped with Ba, Ca and Sr excited by 326 nm is presented in figure 3.10 (b). The PL spectra showed the broad band emission between 400 and 800 nm. The intensities of the phosphors are varied according to their ionic size. The broad band emission peak of $Zn_2V_2O_7$ consists of two broad peaks corresponding to emissions Em_1 ($^3T_2 \rightarrow ^1A_1$) and Em_2 ($^3T_1 \rightarrow ^1A_1$) transitions state of V^{5+} ion in the VO_4 tetrahedral, The T_d symmetry is expressed as a ground 1A_1 state and excited 1T_1 , 1T_2 , 3T_1 , and 3T_2 state as shown in figure 3.12. The excitation bands for the Ex_1 and Ex_2 in the excitation spectra correspond to spin-forbidden transitions from the ground state to the excited state 1T_2 , and 1T_1 levels, respectively. The chromaticity coordinates for $Zn_2V_2O_7$ could be turned from yellow-green (0.41, 0.49) to yellow (0.43, 0.49) position by doping with Ba, Ca and Sr as shown in figure 3.13.

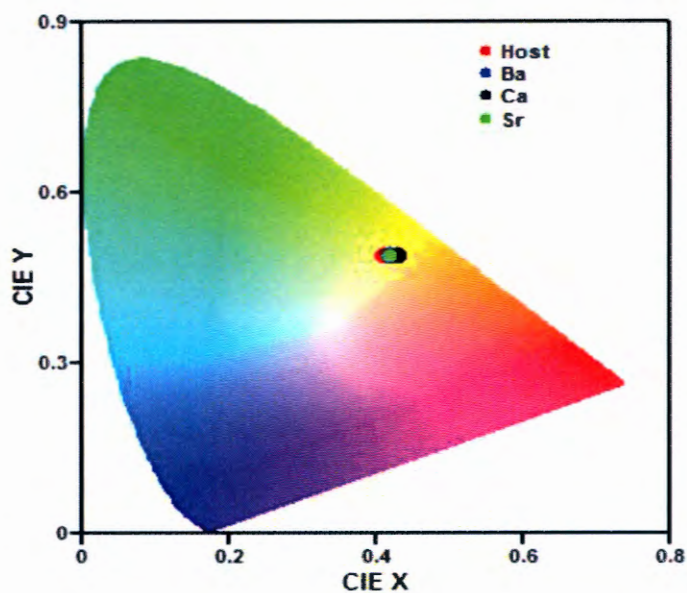


Figure 3.13: CIE chromaticity diagram for $Zn_2V_2O_7$ synthesized at 600°C, and $Zn_2V_2O_7$ doped with (Ba, Ca, and Sr).

Table 1: Luminescence properties of $Zn_2V_2O_7$ phosphors synthesis at (500, 600, and 700 °C), and $Zn_2V_2O_7$ doped with (Ba, Ca and Sr).

Sample	I_{em1}/I_{em2}	P_{em1} (nm)	W_{m1} (nm)	P_{em2} (nm)	W_{em2} (nm)	CIE (x,y)	Emission color
$Zn_2V_2O_7$ 500°C	2.016	550	98	620	136	(0.41,0.50)	Yellow green
$Zn_2V_2O_7$ 600°C	1.319	544	91	608	131	(0.41,0.49)	Yellow green
$Zn_2V_2O_7$ 700°C	1.923	553	98	618	135	(1.42,0.49)	Yellow green
$Zn_2V_2O_7$ doped Ba	1.877	553	99	621	134	(0.42,0.49)	Yellow
$Zn_2V_2O_7$ doped Ca	1.664	553	99	620	136	(0.43,0.49)	Yellow
$Zn_2V_2O_7$ doped Sr	1.823	554	99	620	134	(0.42,0.49)	yellow

All properties were measured at room temperature I, P and W present luminescent intensity, peak position and peak width, respectively. Subscripts em1 and em2 represents emissions.

3.3 Conclusion

The self-activated yellow emitting phosphor of $Zn_2V_2O_7$ was successfully prepared at initiation temperatures of 500, 600, and 700°C and doped with Ba, Ca and Sr at 600°C via the combustion process. Its structural and PL properties were studied. The XRD results indicated the single phase monoclinic structure. SEM images showed bigger particles with a hexagonal and cylindrical-like shape, and as the temperature increased the shape of the particles was destroyed. The microstructure retained its original structure when doped with Ba, Ca and Sr. Through the luminescence study $Zn_2V_2O_7$ phosphor exhibits a bright yellow broad band emission from 400 nm to 800 nm at an excitation of 326 nm that consist of two peaks corresponding to the emission from the Em_1 ($^3T_2 \rightarrow ^1A_1$) and Em_2 ($^3T_1 \rightarrow ^1A_1$) transitions states of the V^{5+} ion in the VO_4 tetrahedral.

References

- [1] S. Shionoya and W. M. Yen, "Phosphor Handbook," CRC Press, Boca Raton, (1999) 293-306.
- [2] L. Chen, K. Chen, C. Lin, S. Hu, M. Lee and R. Liu, *J. Comb. Chem.*, **12** (2010) 587-594.
- [3] T. S. Chan, R. S. Liu, and I. Baginskiy, *Chem. Mater.* **20** (2008) 1215-1217.
- [4] A. A. Reddy, S. Das, S. Ahmad, S. Babu, J. M. F. Ferreira, and G. V. Prakash, *RSC Advances* **2** (2012) 8768-8776.
- [5] Y. Q. Li, A. C. A. Delsing, G. D. With, H. T. Hintzen, *Chem. Mater.*, **17**, (2005) 3242-3248.
- [6] M. S. Wang, S. P. Guo, Y. Li, L. Z. Cai, J. P. Zou, G. Xu, W. W. Zhou, F. K. Zheng, G. C. Guo, *J. Am. Chem. Soc.*, **131** (2009), 13572-13573.
- [7] S. Das, A. A. Reddy, S. S. Babu, G. V. Prakash, *J. Mater. Sci.*, **46** (2011) 7770-7775.
- [8] Y. Huang, Y. M. Yu, T. Tsoboi, H. J. Seo, *Optics express*, **20** (2012) 4360-4368.
- [9] T. Nkajima, M. Isob, T. Tsuchiya, Y. Ueda, T. Manabe, *J. Phys. Chem.*, **114** (2010) 5160-5167.
- [10] T. Nkajima, M. Isobe, T. Tsuchiya, Y. Uyeda, T. Kumagai, *J. of Lumin*, **129** (2009)1598-1601.
- [11] S. Kuang, Y. Meng, J. Lui, Z. Wu , L. Zhao, *Optik*, **124** (2013)5517-5519.
- [12] L. El Mir, J. El Ghouli, S. Alaya, M. Ben Salem, C. Barthou, H. J. von Bardeleben, *Physica B*, **403** (2008) 1770-1774.
- [13] P.Y. Zavalij, F. Zhang, M. S. Whittingham, *Solid State Science*, **4(5)** (2002) 91-97 (2002).
- [14] U. Rambabu, D. Amalnerkar, B. Kale, S. Budduhudu, *Meter. Res. Bull.*, **35** (200) 929-936.
- [15] R. M. Mohamed, F. A. Harraz, and I. A. Mkhallid, *J. of Alloys and Compounds*, **532** (2012) 55-60.
- [16] H. N. Luitel, R. Chand, T. Torikai, M. Yada and T. Watari, *International J. of Photoenergy*, 2013 (2013) 3-9.
- [17] S. P Kuang, Y. Meng, J. Lui, Z. C. Wu, L. S. Zhao, *Optik*, **124** (2013) 5517-5519.
- [18] B. D. Cullity, 1956 *Elements of X-ray Diffraction* (2nd Ed), Addison Wesley, 284-285.
- [19] S. Lee, D. Song, D. Kim, J. Lee, S. Kim, I. N. Park, Y. D. Choi, *Materials Letters*, **58** (2004) 342-346.

- [20] L. F Koao, F. B Dejene, H. C Swart, J. R Botha, *J. of Luminescence*, **143** (2013) 463-458.
- [21] S. Karamat, S. Mahmood, J. J. Lin, Z. Y. Pan, P. Lee, T. L. Tan, S. V. Springham, R. V. Ramanujan, *Applied Surface science*, **254** (2008) 7285-7289.
- [22] Y. Oka, T. Yao, N. Yamamoto, *Mat. Res. Bull.*, **32 (9)** (1997) 1201-1209.
- [23] S. Krachodnok, K. J. Haller, D. Williams, *Engineering Journal*, **16** (2012) 19-27.
- [24] C. Liu, Y. Wang, Y. Hu, R. Chen, F. Liao, *J. of alloy and compounds*, **470** (2009) 473-476.
- [25] S. Benmokhtar, A. El Jazouli, J. P. Chaminamde, P. Gravereau, F. Guien, D. De Waal, *J. Solid State Chem.* **177(11)** (2004) 4175-4182.
- [26] A. A. Setlur, H. A. Comzo, A. M. Ssrava, W. W. Beers, *J. Electrochem. Soc.*, **152(12)** (2005) H205-H208.

The effect of annealing temperature on the structure and luminescence of $Zn_2V_2O_7$ prepared by sol-gel method

4.1 Introduction

During the few past years, vanadium oxides based material due to their structure, magnetic and optical properties have attracted special attention from researchers. Once the vanadate centre becomes excited, a broad luminescence in the visible region can be observed. Vanadate group $(VO_4)^{3-}$ where four oxygen ions in a tetrahedral (T_d) symmetry is coordinated on a central ion, is known as an efficient luminescent centre [1-2]. Among various vanadium oxides materials, zinc vanadate ($Zn_2V_2O_7$) has recently caught attention due to its yellow-green self-activation. $Zn_2V_2O_7$ is also interesting because it crystallize at a low temperature, which is consistent for saving energy and reducing the cost of production [3]. $Zn_2V_2O_7$ was reported to be a good material for application on white light emitting diodes [4]. Zinc vanadate ($Zn_2V_2O_7$) has a crystal structure of monoclinic with a spacing group $C2/c$ [5]. Several methods have been reported for the preparation of $Zn_2V_2O_7$ such as solid state method [6-7], hydrothermal method [8], combustion method [9, 10], and microwave method [11]. *Pookmanee et al.* [3] reported the structural properties of B_iVO_4 annealed at different temperature prepared by sol-gel method. It has been reported that the annealing temperature enhance the emission intensity. *Chen et al.* [12] reported the preparation of $Zn_2V_2O_7$ nanoflakes using hydrothermal synthesis. Other researchers prepared $Zn_2V_2O_7$ using solid state reaction method and found the agglomerated particles [4]. *S. D Abraham* [11] used microwave assisted combustion route to synthesize spherical hollow $Zn_2V_2O_7$ nanospheres. However $Zn_2V_2O_7$ prepared by sol gel method has not been reported so far. In this paper we report the preparation of $Zn_2V_2O_7$ by sol-gel method. Sol-gel method has advantage over other methods like: short annealing time, lower processing temperature, good control of the size and shape of particles. The effects of annealing temperatures on structural and luminescence properties were studied.

4.2 Results and discussion

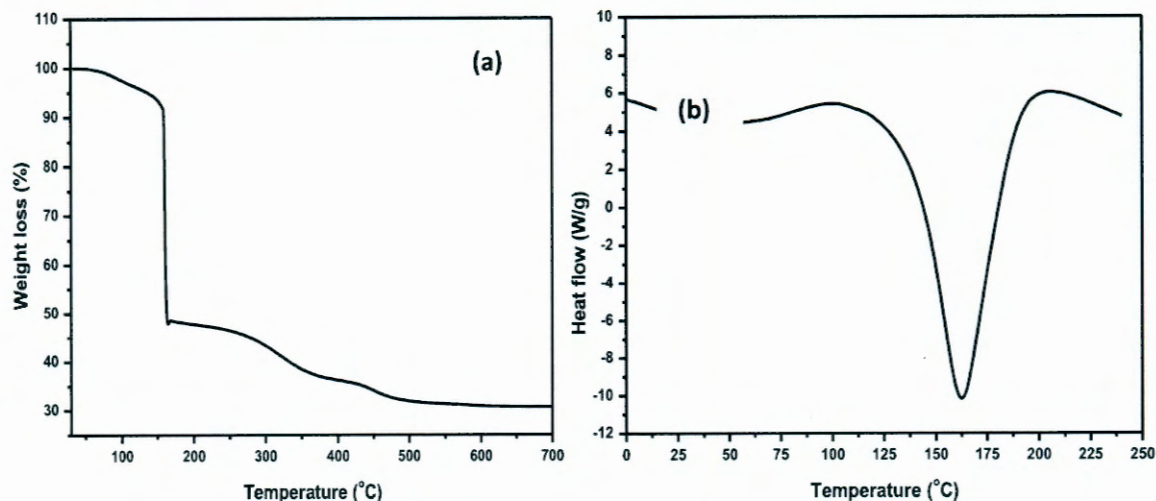


Figure 4.1: (a) TGA and (b) DSC curves of the $Zn_2V_2O_7$ powder prepared by sol gel.

The thermal behaviour of $Zn_2V_2O_7$ was investigated by TGA and DSC. TGA and DSC results of $Zn_2V_2O_7$ containing $(Zn(NO_3)_2, NH_4VO_3, \text{ and } C_6H_8O_7)$ as raw materials are shown in figure 4.1. The sample shows the endothermic peak in the DSC curve in a range temperature from 30 to 110°C which in accordance with the first weight loss. Thermal analysis shows three weight loss processes in TGA. The first weight loss (46%) endothermic from 110 to 160°C, is assigned to the removal of water. The second weight loss (10%) is from 160 to 350°C due to the decomposition of $Zn_2V_2O_7$. There is endothermic weight loss (6.3%) from 350 to 500°C. TGA indicates a total weight loss of 65.3% when temperature is raised from 30 to 500°C. No significant weight loss has been observed beyond 500°C. The stable residue that extends to 700°C was ascribed to crystallization of $Zn_2V_2O_7$. Figure 4.2 presents the x-ray diffraction results analysis of $Zn_2V_2O_7$ powder annealed at 700 – 850°C for 2 hours. All the samples can be indexed to monoclinic $Zn_2V_2O_7$ (ICSD 70-1532). No peaks of any other phases or impurities were observed. The diffraction intensity increased while the line width of the samples decreased with increasing of the annealing temperature. The samples become highly crystallized at higher annealing temperature. The full width at half maximum (FWHM) of (022) peak was used to measure the crystalline quantity of the $Zn_2V_2O_7$ crystallites. The FWHM decreased from 0.066° to 0.042° as annealed temperature increased from 700 to 850°C as shown in figure 4.3. The estimated particle size increased from 77 nm at 700°C to 90 nm at 850°C.

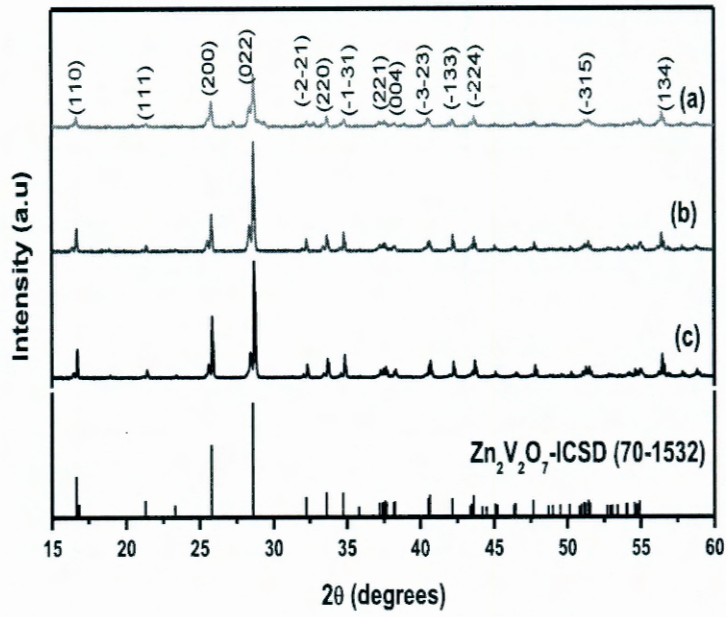


Figure 4.2: XRD spectra of $Zn_2V_2O_7$ powder annealed at (a) 700 (b) 770 and (c) 850°C for 2 hours.

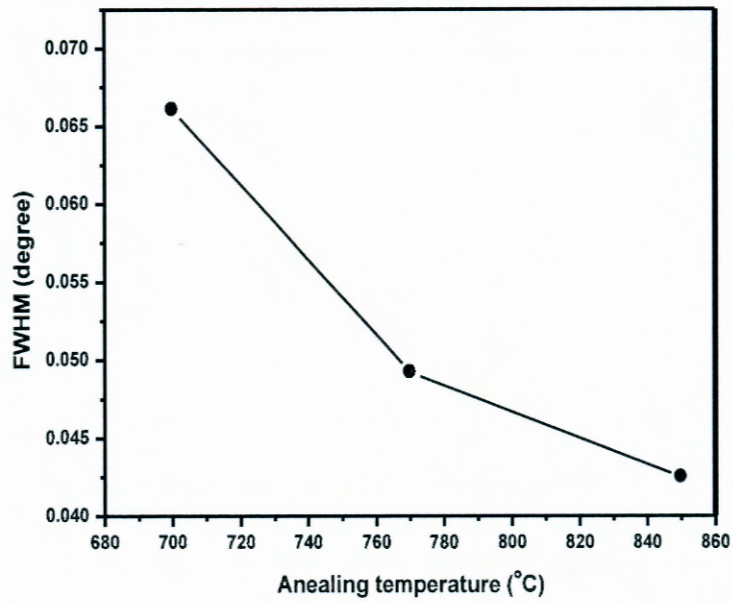


Figure 4.3: Full width at half maximum of the (022) XRD peak as a function of annealing temperature.

This clearly shows that the average particle size of the $Zn_2V_2O_7$ depends on annealing temperature. The calculated lattice parameter of $Zn_2V_2O_7$ was found to be $a= 7.429$, $b= 8.834$ and $c= 10.09$, like other researchers reported that the lattice parameters are temperature dependent [13].

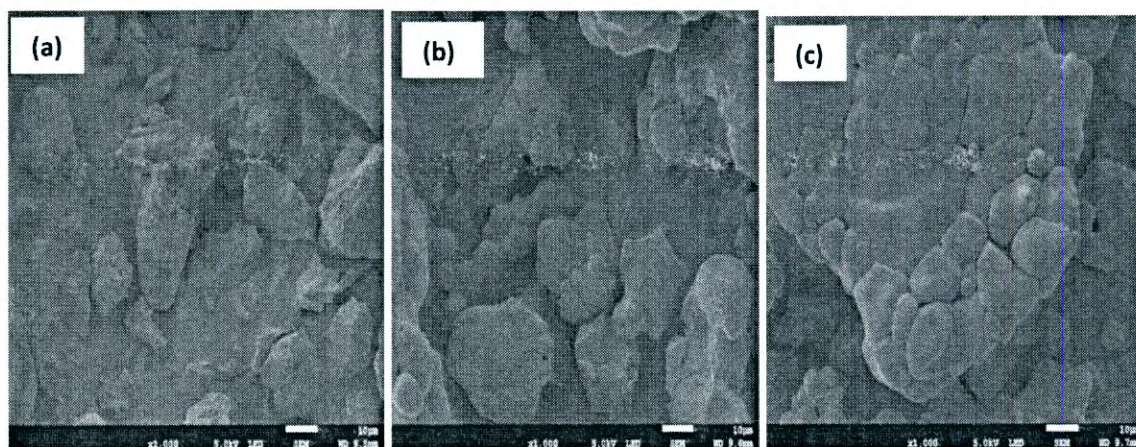


Figure 4.4: SEM images of $Zn_2V_2O_7$ powder annealed at (a) 700 (b) 770 and (c) 850°C for 2 hours.

SEM images of the $Zn_2V_2O_7$ samples annealed at (a) 700°C, (b) 770°C, and 850°C are shown in figure 4.4. All the $Zn_2V_2O_7$ samples have very smooth surfaces. At low temperature of 500 °C the image shows scattered particles. As the temperature increased the particles slightly agglomerated. The growth of $Zn_2V_2O_7$ particle size as the temperature increased further to 850°C, resulted in the spherical aggregation of the particles [14]. A high uniformity in particle size indicates that a higher annealing produces a sufficient uniform particle size. The particle size of $Zn_2V_2O_7$ increased with the increase in annealing temperature, which was due to crystallization of the samples as shown in XRD results. The element composition of $Zn_2V_2O_7$ powders prepared by sol-gel method is shown in figure 4.5. The single phase of $Zn_2V_2O_7$ powder consists of zinc (Zn), vanadium (V), and oxygen (O) only.

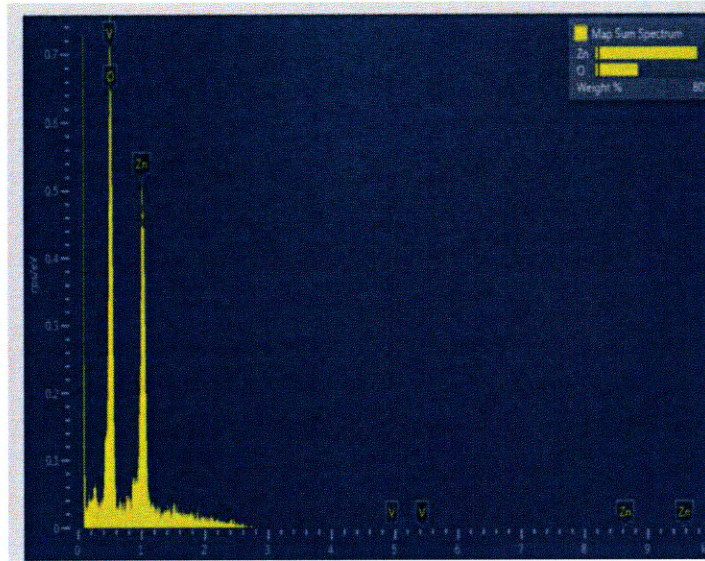


Figure 4.5: EDS spectra $Zn_2V_2O_7$ powder prepared by sol gel.

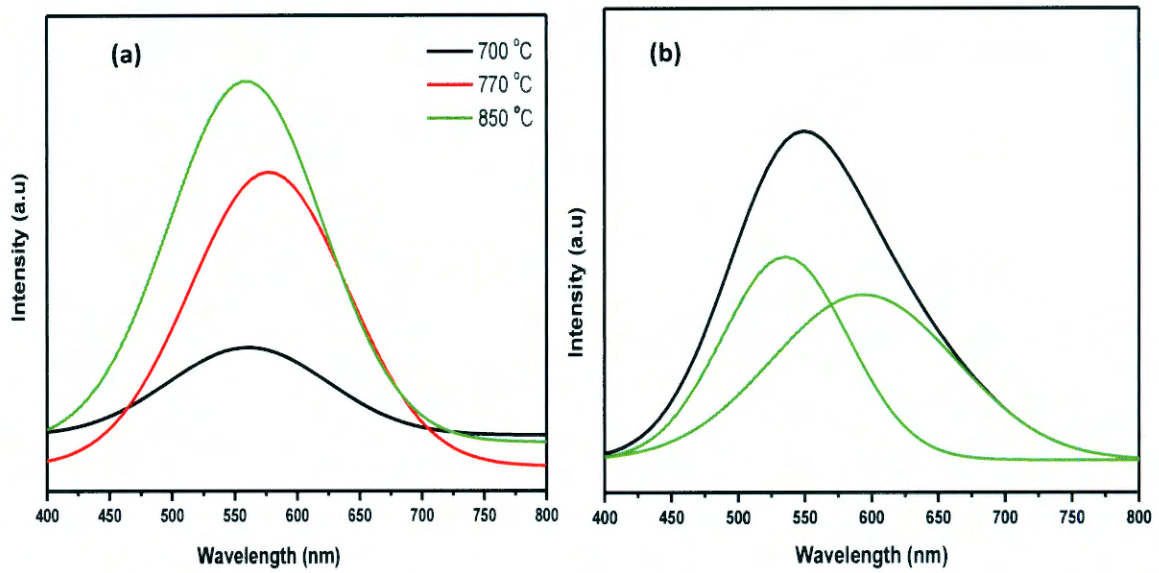


Figure 4.6: (a) Photoluminescence emission spectra of $Zn_2V_2O_7$ powder annealed at 700, 770 and 850°C for 2 hours (b) PL emission spectra of $Zn_2V_2O_7$ annealed at 850°C fitted with two Gaussian curves.

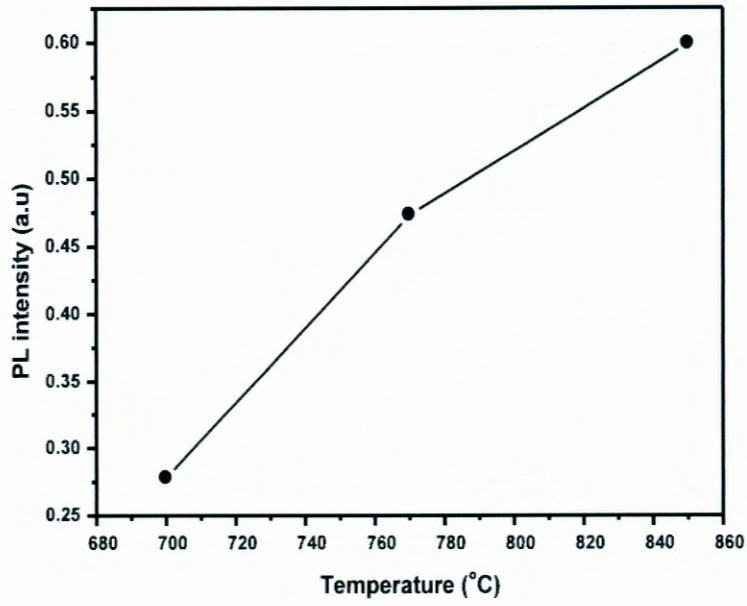


Figure 4.7: PL intensity as a function of annealing temperature.

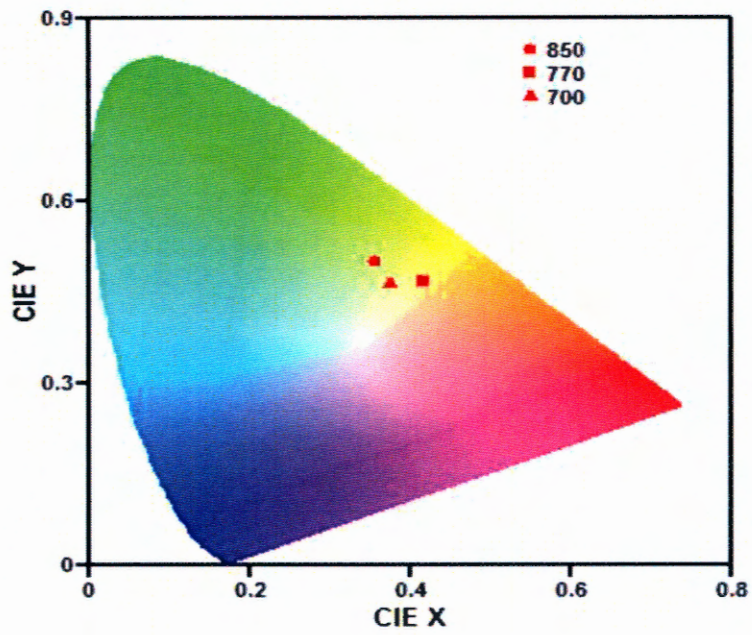


Figure 4.8: CIE chromaticity colour diagram of Zn₂V₂O₇ annealed at 700, 750 and 850°C.

The PL emission spectra of $Zn_2V_2O_7$ annealed at different temperature is shown in figure 4.6 (a). The spectra indicate the broad band from 400 nm to 800 nm which consist out of the two peaks shown in figure 4.6(b). The broad yellow to green emission band of $Zn_2V_2O_7$ corresponding to transitions from the 3T_2 and 3T_1 states to the 1A_1 ground state of V^{5+} ions, was observed [15]. The emission bands of the samples are shifting towards higher wavelength with annealing temperature. This is associated to the increase in particle sizes of $Zn_2V_2O_7$ as seen in the XRD results [16]. *Luwang et al.* [17] said the shifting of the peak towards a longer wavelength or towards a shorter wavelength might be related to the increase in covalent bonding on annealing. The sample annealed at low temperature has low emission intensity, because of a poor crystallinity. Higher annealing temperature enhances the luminescence intensity. The emission intensity increased with an annealing temperature, due to the improvement of the crystallinity. The PL peak intensity of the emission spectra as a function of annealing temperature ranging from 700 to 850°C was shown in figure 4.7. The PL peak intensity increased gradually with an increasing annealing temperature. As discussed above with XRD data, the crystallinity of the $Zn_2V_2O_7$ was improved with annealing temperature. The Commission Internationale de l'Elclairage CIE chromaticity diagram is shown in figure 4.8.

The calculated CIE colour coordinates for all the annealed samples are summarized in Table 1. The $Zn_2V_2O_7$ samples show the CIE coordinate around the green and yellow regions. The emission colour of annealed samples shifted from yellow with chromaticity coordinate of $x=0.417$ and $y=0.469$ to green colour with the coordinate of $x=0.354$ and $y=0.501$ when annealed from 700-850°C.

Table 1: CIE chromaticity colour coordinates in $Zn_2V_2O_7$ annealed at different temperatures.

Sample No.	Sample	CIE chromaticity coordinates	
		x	y
1	$Zn_2V_2O_7$ -700 °C	0.373	0.464
2	$Zn_2V_2O_7$ -770 °C	0.417	0.469
3	$Zn_2V_2O_7$ -850 °C	0.354	0.501

4.3 Conclusion

$Zn_2V_2O_7$ phosphor was successfully prepared by sol-gel method with zinc nitrate, ammonium metavanadate as precursors. A single phase monoclinic structure of $Zn_2V_2O_7$ was obtained after annealing at 700 to 850°C temperatures for 2 hours. It was obtained that the annealing temperature has influence on the structure and morphology. The aggregation of particle was increasing with the particles size from 77 nm at 700 °C to 90 nm at 850°C. TGA analysis indicates a total weight loss of 65.3% when temperature is raised from 30 to 500°C, this is due to the crystallinity of $Zn_2V_2O_7$. No significant weight loss has been observed beyond 500 °C . The photoluminescence emission spectra of $Zn_2V_2O_7$ annealed at different temperature was observed. The broad yellow to green emission band of $Zn_2V_2O_7$, which consist of the two peaks corresponding to the 3T_2 and 3T_1 states to the 1A_1 ground state of V^{5+} ions was observed.

References

- [1] Y. Huang, Y. M. Yu, T. Tsuboi and H. J. Seo, *Optics express*, **20** (2012) 4360-4368.
- [2] S. Mukhtar, C. Zou, W. Gau, *Appl. Nanosci*, **3** (2013) 535-542.
- [3] P. Pookmanee, S. Kojinok, S. Phanichiphant, *J. of Metals, Materials and Minerals*, **22** (2012) 49-53.
- [4] S. P. Kuang, Y. Meng, J. Liu, Z. C. Wu, L. S. Zhao, *Optik*, **124** (2013) 5517-5519.
- [5] P. Y. Zavalij, F. Zhang, M. Stanley, Whittingham, *Solid State Sciences*, **4** (2002) 591-597.
- [6] H. N. Luitel, R. Chand, T. Torikai, M. Yada, T. Watar, *International Journal of Photoenergy*, **2013** (2013) 1-9.
- [7] B. K. Grandhe, S. Ramaprabhu, S. Buddhudu, K. Sivaiah, V. R. Bandi, K. Jang, *Optics communications*, **285** (2012) 1194-1198.
- [8] M. Wang, Y. Shi, G. Jiang, *Materials Research Bulletin*, **47** (2012) 18-23.
- [9] S. S. Pitale, M. Gohain, I. M. Nagpure, O. M. Ntwaeaborwa, B. C. Bezuidenhout, H. C. Swart, *Physica B*, **407** (2012) 1485-1488.
- [10] R. M. Mohammed, F. A. Harraz, I. A. Mkhaliid, *J. of Alloy and Compounds*, **532** (2012) 55-60.
- [11] S. D. Abraham, S. T David, R. B. Bennie, C. Joel, M. Seethalakshimi, T. Adinaveen, *Chemical Science Transactions*, **3(4)** (2014) 1488-1496.
- [12] Z. Chen, W. Huang, D. Lu, R. Zhao, H. Chen, *Materials Letters*, **107** (2013) 35-38.
- [13] P. Thiyagarajan, M. Kottaisamy. M. S. Ramachandra Rao, *J of the Electrochemical Society*, **154** (2007) H297-H303.
- [14] S. E. Hashemi Amiri, M. R. Vaezi and A. Esmailzadeh Kandjani, *Journal of Ceramic Processing Research*. **12** (2011) 327-331.
- [15] X. Chen, Z. Xia, M. Yi, X. Wu and H. Xin, *Journal of Physics and Chemistry of Solids* **74** (2013) 1439-1443.

[16] S. F. Shayestehad, A. Ahmad and D. I. Zgahj, *J. of Physics*, **81** (2013) 319-330.

[17] M. N. Luwang, R. S. Ningthoujam, S. K. Srivastava and R. K. Vatsa, *J. of Material Chemistry*, **21** (2011) 5326-5337.

Combustion synthesis of Dy³⁺-doped YVO₄

5.1 Introduction

Yttrium orthovanadate (YVO₄) belongs to the space group ¹⁹D_{4h} [1] and it is an important optical material that has been given considerable attention due to its outstanding characteristics, such as excellent thermal, mechanical and optical properties. In recent years, significant progress has been made on luminescent materials using YVO₄ as host lattice and its emission colors are based mainly on the f–f transition [2]. Eu³⁺ doped YVO₄ nanocrystals have been widely used as an important commercial red phosphor. Their applications include color television, cathode ray tube, fluorescent lamps and plasma display panels. Yttrium orthovanadate activated by trivalent dysprosium (YVO₄:Dy) is a well-known phosphor material with high efficiency. The emission color of the luminescence is close to white because of the yellow (⁴F_{9/2} → ⁶H_{13/2}) and blue (⁴F_{9/2} → ⁶H_{15/2}) emissions of Dy³⁺. There are two basic approaches to generate white light from light emitting diodes (LEDs). One is by mixing light of different colors emitted by several chips called multichip LEDs and the other is to convert the light emitted from a blue or ultraviolet (UV) LED to a longer wavelength light using phosphors, which are called phosphor-converted (pc) – LEDs [3]. In order to produce a phosphor that will produce white light for the LED applications Dy³⁺ –doped YVO₄ phosphors were produced by a combustion method at 600°C. There are many methods to prepare YVO₄ phosphors, such as the chemical co-precipitation method [4], sol–gel method [5] and hydrothermal method [6]. Combustion has for a long time been the major source of energy for heating, transportation and production of electricity [7]. The combustion synthesis is very good because it can provide a product without sintering. In this paper, we report on the synthesis of YVO₄ phosphor material doped with different Dy³⁺ concentrations by combustion method. The structure and the luminescence properties of the YVO₄:Dy³⁺ is discussed.

5.2 Results and discussion

5.2.1 XRD study

Figure 5.1 shows the XRD patterns of YVO₄ phosphor material doped with different concentration of Dy. The XRD patterns show the tetragonal phase and agreed well with

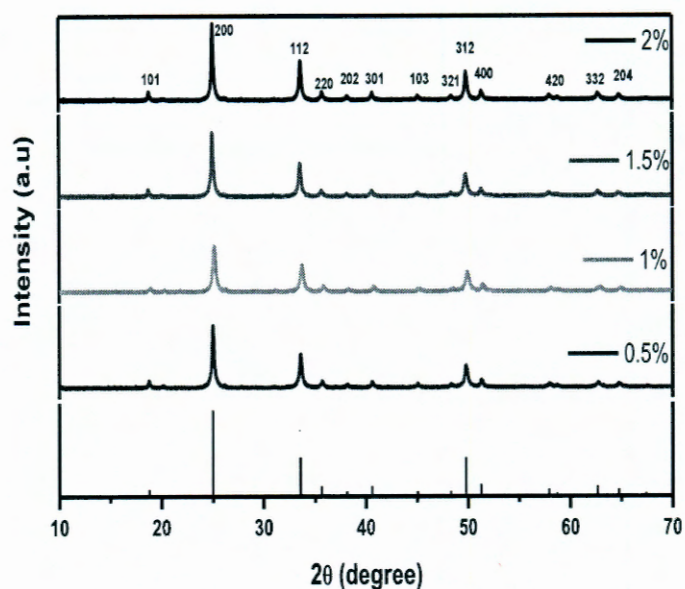


Figure 5.1. XRD pattern for the $\text{YVO}_4:\text{Dy}^{3+}$ phosphors –doped with different concentration of Dy^{3+} as well as the standard JCPD file (17-0341).

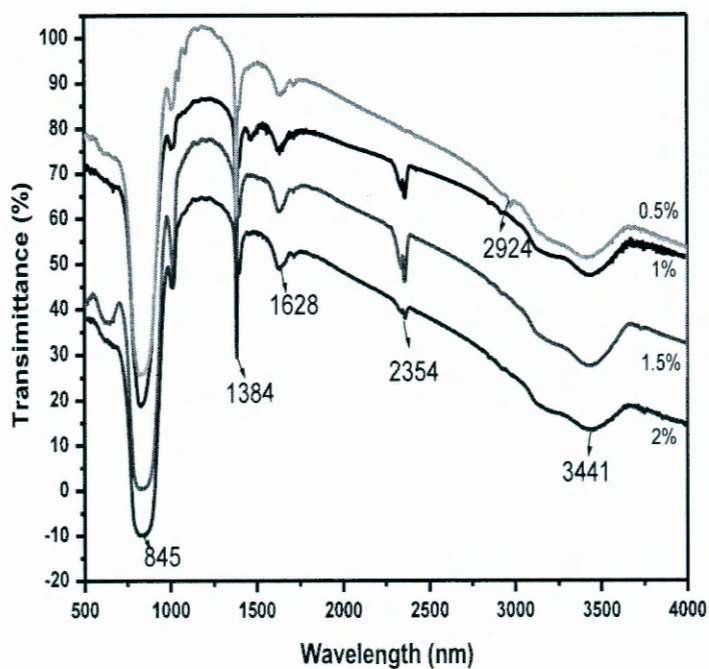


Figure 5.2. FTIR spectra of $\text{YVO}_4:\text{Dy}^{3+}$.

standard JCPD file (17-0341) [8]. It is clear from the XRD patterns that no impurity phases were present which shows that all reactants have reacted completely. The average crystallite

size determined from the broadening of the peaks (200), (112) and (312) using Scherrer formula was about 31 nm. The calculated lattice parameters were found to be $a = 0.711$ nm and $b = 0.628$ nm.

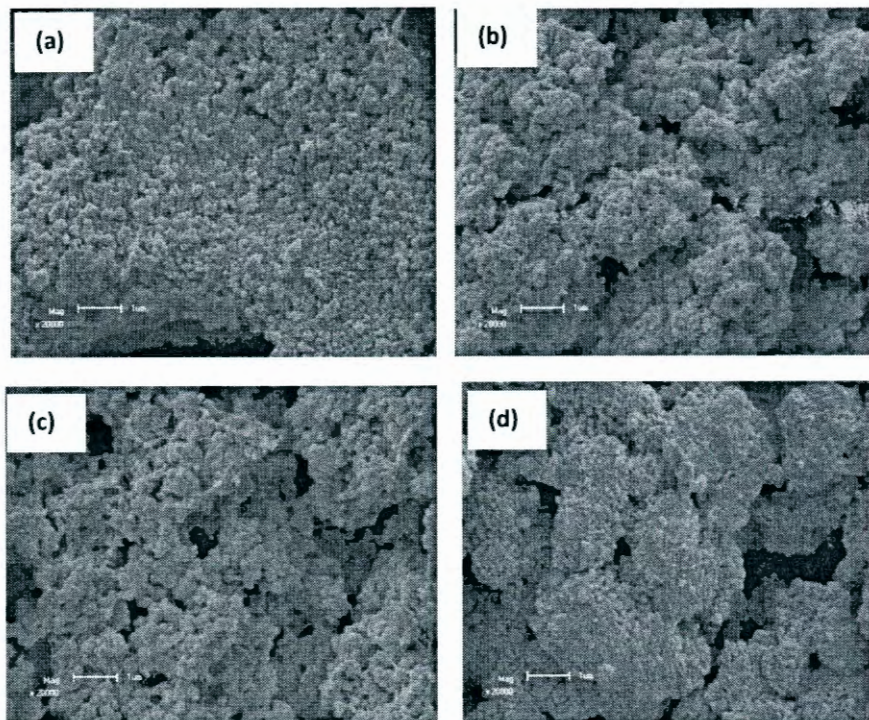


Figure 5.3. SEM image of $\text{YVO}_4:\text{Dy}^{3+}$ doped with (a) 0.5, (b) 1, (c) 1.5, and (d) 2 mol % Dy^{3+} ions

5.2.2 FTIR study

Figure 5.2 shows the FTIR spectra prepared for the combustion method at different concentrations of Dy^{3+} . The most intense band shows the characteristics of the V-O bonds with strong band ranges from $776\text{--}921\text{ cm}^{-1}$ consisted of a peak at 845 cm^{-1} . A broad band centered at 3441 cm^{-1} is assigned to the symmetric stretching vibration of H-O-H (H_2O molecules). The strong peak observed at 1384 cm^{-1} is ascribed to the asymmetrical vibration of the carboxyl groups. It can be seen that the position of the V-O stretching vibration remained the same for all the samples. The two weak bands at 2354 cm^{-1} and 2924 cm^{-1} correspond to the symmetrical and asymmetrical stretching vibration modes of the CH_2 group, respectively. The low 0.5% Dy concentration has some influence on symmetrical vibration modes of CH_2 since the band on 2.54 cm^{-1} is very weak.

5.2.3 SEM study

SEM has been carried out to study the morphological structure of the $\text{YVO}_4:\text{Dy}^{3+}$ prepared by the combustion method. The SEM micrographs that are shown in figure 5.3 show the YVO_4 doped with (a) 0.5, (b) 1, (c) 1.5 and (d) 2 mol% Dy^{3+} ions. In a lower Dy^{3+} concentration the particle size were small and much agglomerated. The particle size seems to increase along with the concentration and its shape changed to bulk-like particles. The surface of the morphology was rough. Table 1 shows the calculated average grain size of the YVO_4 doped with the various concentration of Dy^{3+} . The grain size decreased to 26 nm for 1 mol% of Dy^{3+} , and then increased as the Dy^{3+} concentration increased. When doped with 2 mol% Dy^{3+} the grain size was found to be 35 nm, which is also indicated in the increase in the intensity of the diffraction peaks, as observed in the XRD analysis.

Table I: The average crystallite size for the YVO_4 doped with different concentration of Dy^{3+} calculated by Scherer equation

Dy^{3+} concentration (mol%)	Average grain size (nm)	Experimental error (\pm)
0.5	30	± 4.5
1	26	± 3.7
1.5	30	± 1.2
2	35	± 2.6

5.2.4 PL study

The PL excitation spectrum of $\text{YVO}_4:\text{Dy}^{3+}$ phosphor monitored at an emission wavelength of 574 nm is shown in figure 5.4. The excitation spectra showed a broad peak around 257 nm. Figure 5.5 shows the emission spectra of the $\text{YVO}_4:\text{Dy}^{3+}$ prepared at different concentration of Dy^{3+} . The insert shows the enlargement of the 663 nm peak. The spectra show the characteristics of the emission peaks of Dy^{3+} .

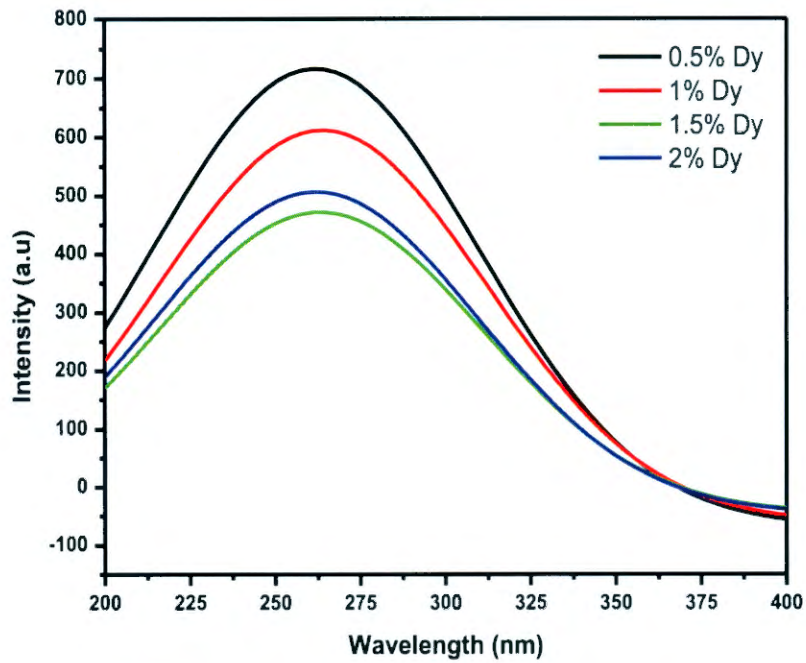


Figure 5.4. Excitation spectra of YVO₄:Dy³⁺

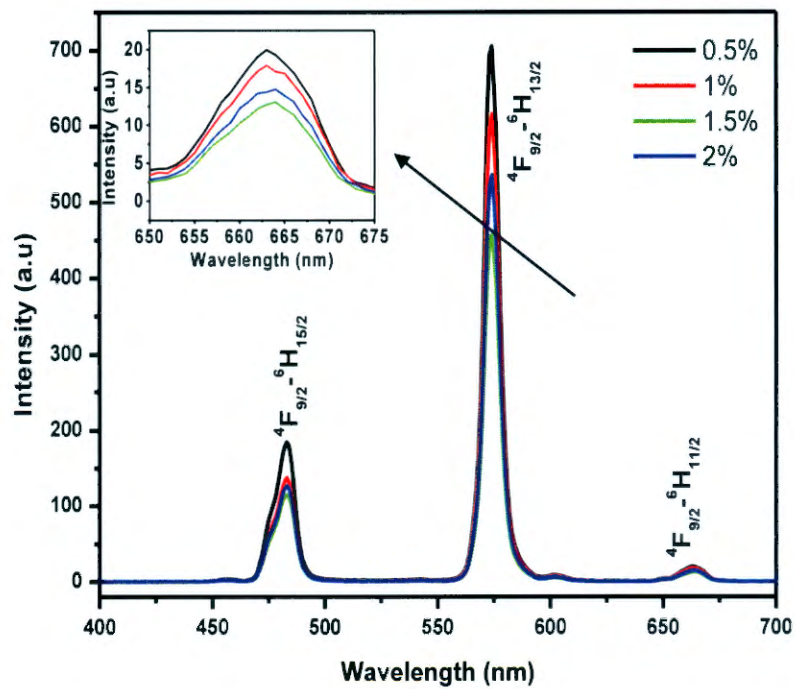


Figure 5.5. PL emission spectra of YVO₄:Dy³⁺.

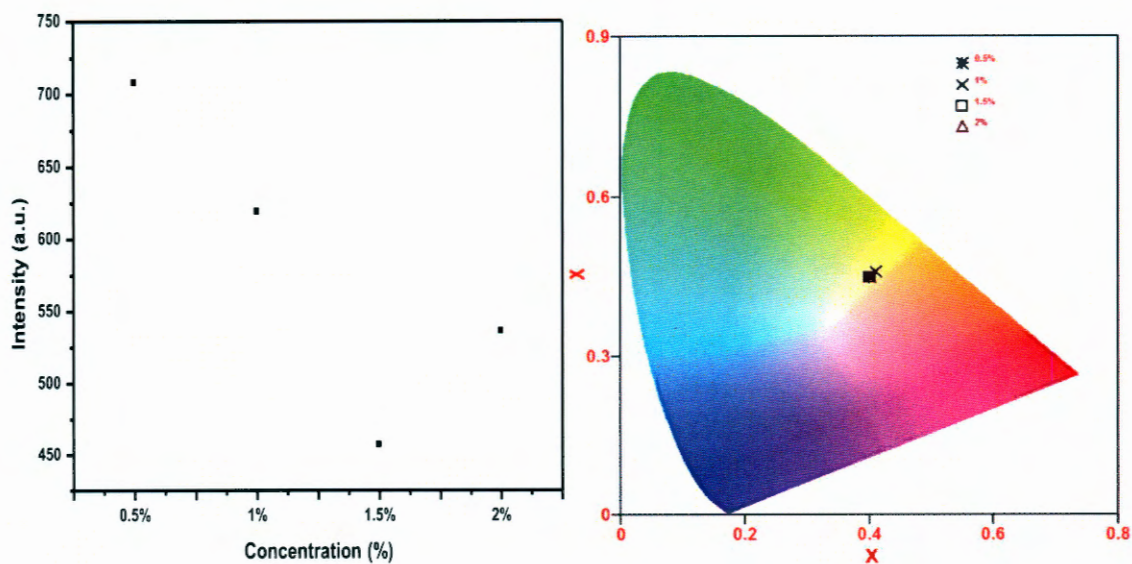


Figure 5.6 (a) 574 nm PL peak intensity vs concentration graph of the $\text{YVO}_4:\text{Dy}^{3+}$ phosphor, (b) CIE of $\text{YVO}_4:\text{Dy}^{3+}$.

The peaks are located at 483 nm (blue) and 574 nm (yellow). The peaks are related to the hypersensitive transition $4\text{F}_{9/2}-6\text{H}_{15/2}$ and the $4\text{F}_{9/2}-6\text{H}_{13/2}$, respectively. There is a very weak emission band located at 663 nm which correspond to the $4\text{F}_{9/2}-6\text{H}_{11/2}$ transition. The intensity of the yellow emission is stronger than that of the blue emission, because Dy^{3+} is located at a site of the D_{2d} , which is deviated from an inverse center in the YVO_4 host [9]. The maximum PL intensity was observed for the lower concentration of 0.5%, figure 5.6 (a). The PL peak intensity showed a decrease in intensity as the concentration of Dy^{3+} increased due to concentration quenching and then the intensity increased again when the concentration reached 2% as shown in figure 5.6. The reason is when the concentration is far above the critical concentration the intensity of the Dy^{3+} emission will increase quickly as the concentration increase until it reaches another critical concentration, and then the intensity of Dy^{3+} emission will decrease again for the energy transfer among different Dy^{3+} ions [10].

5.2.5 CIE chromaticity diagram

The emission color of the $\text{YVO}_4:\text{Dy}^{3+}$ phosphor can be expressed by Commission Internationale de l'Éclairage (CIE) coordinates as indicated in figure 5.6(b). The chromaticity coordinate for the $\text{YVO}_4:\text{Dy}^{3+}$ with different Dy^{3+} concentrations are very similar. It is clear that the $\text{YVO}_4:\text{Dy}^{3+}$ emitted a more yellowish color light. The blue part helped to shift it

slightly towards the white part of the spectrum. The phosphor can be used as a yellow emitted material in LEDs.

5.2.6 Lifetime study

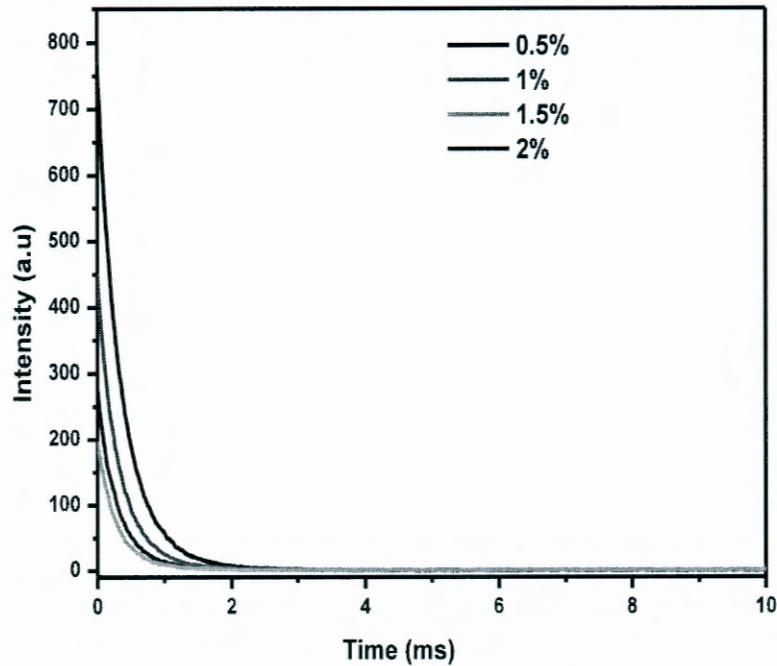


Figure 5.7. Decay curves of $\text{YVO}_4:\text{Dy}^{3+}$ phosphors with different concentration of Dy^{3+} .

Figure 5.7 shows the decay curves for the different concentration of Dy^{3+} doped YVO_4 . The logarithmic plots of the curves were fitted by a two order exponential decay equation:

$$I = A_1 \exp(-t/\tau_1) + A_2 \exp(-t/\tau_2) \quad (3)$$

Where I represent the phosphorescent intensity, τ_1 and τ_2 correspond to shorter and longer lifetime constants, and A_1 and A_2 are constants. The parameters for the fitting data are listed in table 2. The phosphorescence decay times as shown in table 2 can be explained by an initial rapid decay and then an intermediate transitional. A decrease in the intensity with an increase in concentration is due to the improvement of the crystallinity as the particle size increased with the concentration [11].

Table 2: Lifetime values obtained after bi-exponential fitting

to the data of $\text{YVO}_4:\text{Dy}^{3+}$.

%Dy	τ_1 (ms)	τ_2 (ms)	A_1	A_2
0.5	0.27	0.56	273	493
1	0.26	0.89	20	177
1.5	0.26	0.65	27	267
2	0.28	0.64	47	150

5.3 Conclusion

$\text{YVO}_4:\text{Dy}^{3+}$ phosphors prepared with different concentration of Dy^{3+} have been synthesized by the combustion method at 600°C . The XRD characteristics confirmed the crystalline single phase present in the sample. In SEM images the particle size seemed to increase along with the concentration of Dy^{3+} . The emission color of the luminescence is yellow (${}^4\text{F}_{9/2} \rightarrow {}^6\text{H}_{13/2}$) and approaching the white region due to the blue (${}^4\text{F}_{9/2} \rightarrow {}^6\text{H}_{15/2}$) emissions of Dy^{3+} and has the potential to be used as a phosphor for pc-LEDs. The intensity of the PL was decreasing while increasing the concentration due to concentration quenching.

References

- [1] W. Hao, X. Huifang, S. Qiang S, C. Tianhu and W. Mingmei, *J. Mater. Chem.*, **13** (2003) 1223–1228.
- [2] D. L. T. Lizhu, S. Jianhui, Y. Hua, *J. of Alloys and Compounds*, **512** (2012) 361–365.
- [3] H. Young, P. S. K. Jong, K. Ji , K. Jong, D. Young, 2004 *Bull. Korean Chem.,Soc.*, **25**(10) (2004) 1585-1588.
- [4] J. Wang, Y. Xu, H. Mirabbos, C. Y. H. Liu, *J. of Alloys and Compounds*, **24** (2009) 772–776.
- [5] M.Yu, J. Lin, Z. Wang, J. Fu, S.Wang, H. J. Zhang, Y. C. Han, *J. Mater.*, **14** (2002) 2224-2231.
- [6] Y. Y. Liang, P. Chui, X. Sun X, Zhao Y, F. Cheng, K. Su, *J. of Alloys and Compounds*, **552** (2013) 289–293.
- [7] M. Aldén, O. Alaa, R. Mattias, Gustaf Särner *Progress in Energy and Combustion Science*, **37** (2011) 422-461.
- [8] H. Zhang, X. Fu, S. Niu, Q. Xin, *J. of alloys and Compounds*, **457** (2008) 61-65.
- [9] K. Yang, F. Zheng, R. Wu, H. Li, X. Zhang, *J. of Rare earths*, **24** (2006) 162-166.
- [10] L. Chen, K. Chen, C. Lin, C. Chu, S. Hu, M. Lee, Liu R, *J. Comb. Chem*, **12** (2010) 587-594.
- [11] N. L. Meitram, S. N. Raghmani, K. S. Sri, K. V. Rajesh, *Journal Mater.Chem.* **21** (2011) 5326-5337.

The effect of urea:nitrate ratio on the structure and luminescence properties of $\text{YVO}_4:\text{Dy}^{3+}$ phosphors

6.1 Introduction

Most of luminescence materials such as oxides, oxysulfides, and sulphides are doped with transition metal or rare earth ions. Although the luminescence characteristics of vanadates phosphors have been reported, yttrium vanadates (YVO_4) are good host materials for luminescence efficiency. Like Eu, Tm and other rare earth ions Dy can also act as a useful activator. Many researchers have been reported that YVO_4 can be modified by Eu to be used as a red phosphor in colour television and cathode ray tubes because of its high luminescence [1-3]. Besides europium, Dy^{3+} ions is a good activator for YVO_4 . Dy^{3+} activated YVO_4 materials produce blue, yellow and red emissions consisting of (${}^4\text{F}_{9/2} \rightarrow {}^6\text{H}_{15/2}$), (${}^4\text{F}_{9/2} \rightarrow {}^6\text{H}_{13/2}$) and ${}^4\text{F}_{9/2} \rightarrow {}^6\text{H}_{11/2}$ transitions, in the visible and near infrared region [4]. Dy^{3+} ions give most intense emission in the yellow region [5]. Because of these colours the combined emission is close to white and it can extensively be used as an activator ion in designing the LED based white light sources [6]. Synthesis of YVO_4 has been previously prepared by the sol-gel method [7], solid state reaction, hydrothermal process [8], microwave heating process [9, 10]. The combustion method is one of the ideal techniques, because an exothermic reaction is initiated at the ignition temperature and it generates heat which is manifested in a maximum temperature of 1000-1650 K [11]. *Zhang et al.* [12] prepared $\text{YVO}_4:\text{Dy}^{3+}$ phosphor using sol gel and found agglomerated particles. Also *Hong-Tao Liua et al* [13] studied and reported on the hydrothermal synthesis and optical properties of $\text{YVO}_4:\text{Dy}^{3+}$. Here $\text{YVO}_4:\text{Dy}^{3+}$ was prepared by the combustion method at an initiation temperature of 600°C. The particle size, phase homogeneity and morphology were well controlled. The effect of the ratio of urea on the structure and luminescence properties has been investigated.

6.2 Results and discussion

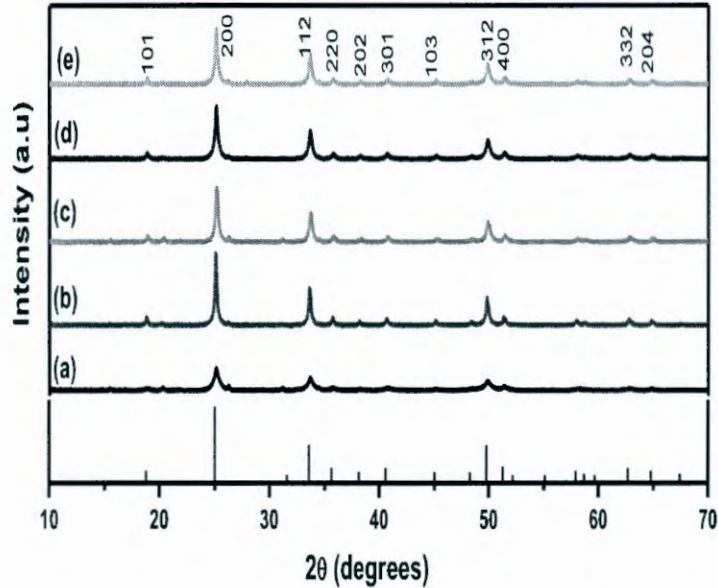


Figure 6.1: XRD patterns of $\text{YVO}_4:\text{Dy}^{3+}$ with various ratios of urea:nitrate (a) 1, (b) 2, (c) 2.5, (d) 3 and (e) 4.

The amount of urea (NH_2CONH_2) was introduced as a fuel because of its effectiveness in an exothermic reaction. Figure 6.1 shows the XRD patterns of the $\text{YVO}_4:\text{Dy}^{3+}$ powders synthesized by combustion method at an initiation temperature of 600°C . The mole ratio of urea:nitrate was varying from 1 to 4. The phosphor powders showed that the XRD peaks were due to the YVO_4 tetragonal phase (JCPDS No. 17-0341) with its lattice parameters $a=0.7119$ nm and $c=0.6228$ nm. No other crystalline phase was observed on the XRD spectra. The XRD patterns showed poor crystallinity at a low mole ratio of urea. This may be due to the fact that at a low concentration of urea the reactive temperature will be lower, and this will lead to poor crystallinity in a sample [14]. When increasing the ratio of the urea to 2 a highly crystalline structure of the $\text{YVO}_4:\text{Dy}^{3+}$ sample was observed, which may be due to the fact that by increasing the ratio of fuel (urea) in the precursor increased the exothermic flame temperature and hence the crystallinity in the product phase [15]. The lattice parameters of $\text{YVO}_4:\text{Dy}^{3+}$ samples have been calculated from the observed values of 2θ using the d interplaner spacing for the tetragonal structure,

$$\frac{1}{d_{hkl}} = \frac{h^2 + k^2}{a^2} + \frac{l^2}{c^2} \quad (1)$$

Where h , k and l are miller indices of the plane and a , c are lattice parameters. The obtained values of the lattice parameters are shown in Table 1. The calculated lattice parameters were found to be in good agreement when compared with the one from the standard JCPDS tetragonal structure. The values of the crystalline size were estimated from the Scherrer's formula. The crystalline size values were found to be 20, 38, 33, 30 and 27 nm for the samples prepared with the ratio of 1, 2, 2.5, 3 and 4, respectively. The crystalline size decreased after increasing the ratio of urea. The excessively high urea concentration might induce a large heat release, which may cause the formation of a single phase [16].

Table 1. Results for XRD analysis of $YVO_4:Dy^{3+}$ powders with various ratio of urea.

Nitrate/urea ratio	Lattice parameters (nm)		Grain size (nm)
	a	b	
1	0.7081	0.6273	20
2	0.7080	0.6240	38
2.5	0.7075	0.6267	33
3	0.7087	0.6274	30
4	0.7086	0.6273	27

The SEM images of the $YVO_4:Dy^{3+}$ powders with various ratios of urea:nitrate are shown in figure 6.2. The observed results show the formation of agglomeration. It was observed that when increasing the concentration of urea the flake-like particles formed and exhibit some holes at the surface, which may be due to the strong dispersant effect of gasses generated during the reaction. *Husairi et al* [17] reported that nano-flakes were observed when increasing the concentration of urea. *Bacalskilnet al* [18] prepared barium magnesium doped Dy by combustion and observed the flakes-like particles when increasing ratio of urea. As discussed earlier that the increase in urea increased the exothermic flame and this played an important role in controlling the particle size and shape. Figure 6.3 shows the EDS results for the $YVO_4:Dy^{3+}$. The presence of Yttrium (Y), vanadium (v) oxygen (O) elements was observed, which can be attributed to the formation of $YVO_4:Dy^{3+}$.

The diffuse reflectance spectra of $YVO_4:Dy^{3+}$ with various ratios of urea:nitrate is shown in figure 6.4. Broad absorption bands positioned below 350 nm are associated with the absorption of the VO_4^{3-} vanadates groups [19]. There is a weak absorption band centred at 282 nm shown at a ratio of urea of 2. This band can be associated to the charge transfer (CT) of Dy^{3+} .

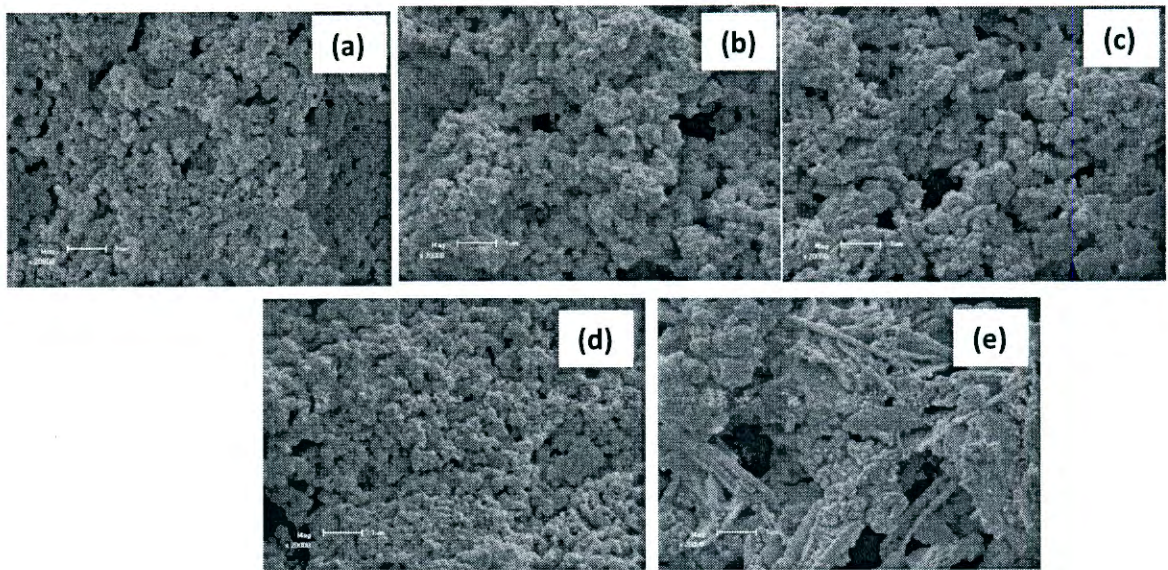


Figure 6.2: SEM images of $\text{YVO}_4:\text{Dy}^{3+}$ for different ratios of urea. (a) 1 (b) 2 (c) 2.5 (d) 3 and (e) 4.

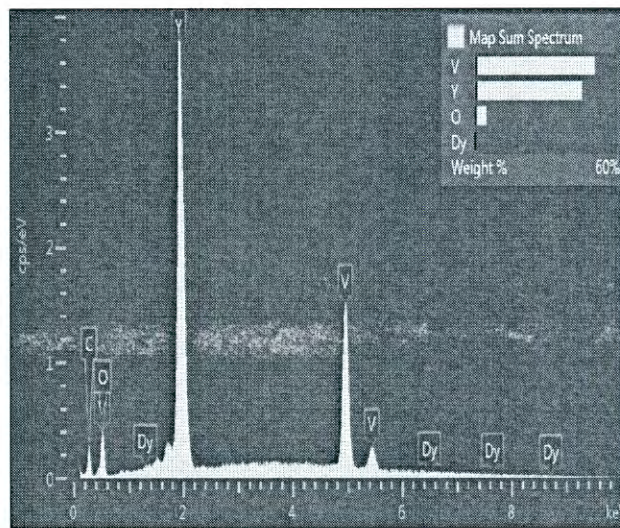


Figure 6.3: EDS spectra of $\text{YVO}_4:\text{Dy}^{3+}$ for the ratio of 2 urea:nitrate.

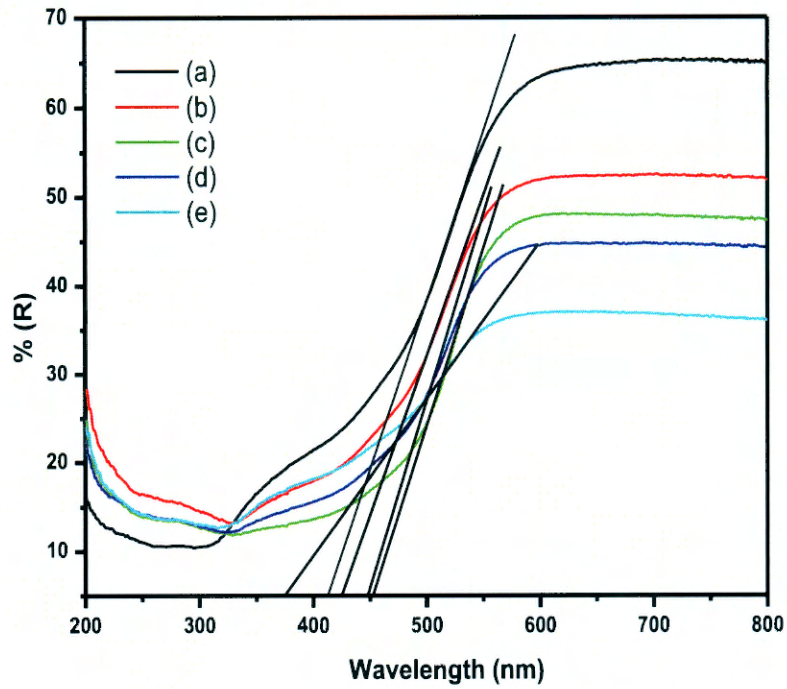


Figure 6.4: The reflectance spectra for $\text{YVO}_4:\text{Dy}^{3+}$ structures prepared with different ratios of urea:nitrate (a) 1, (b) 2, (c) 2.5, (d) 3 and (e) 4.

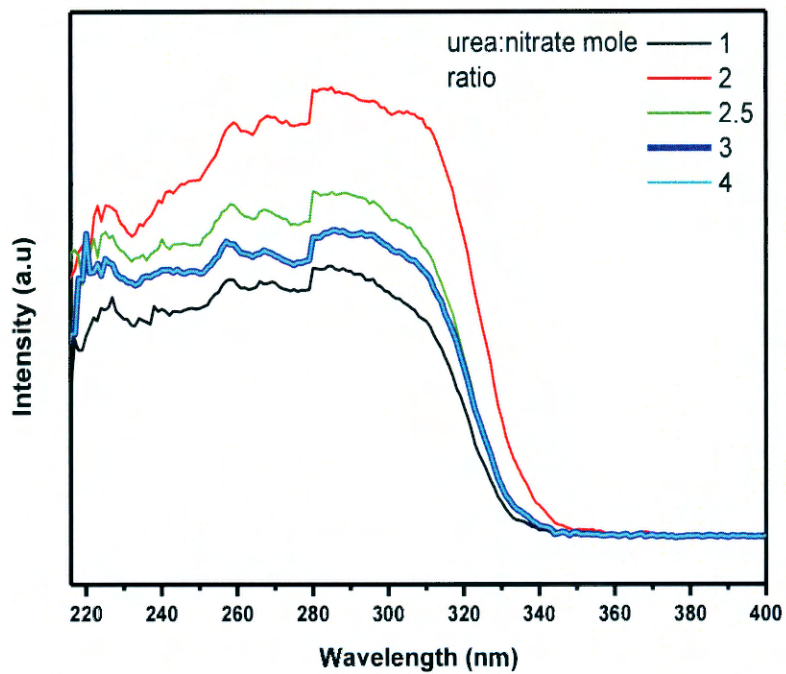


Figure 6.5: PL excitation spectra of $\text{YVO}_4:\text{Dy}^{3+}$ with different ratio of urea:nitrate.

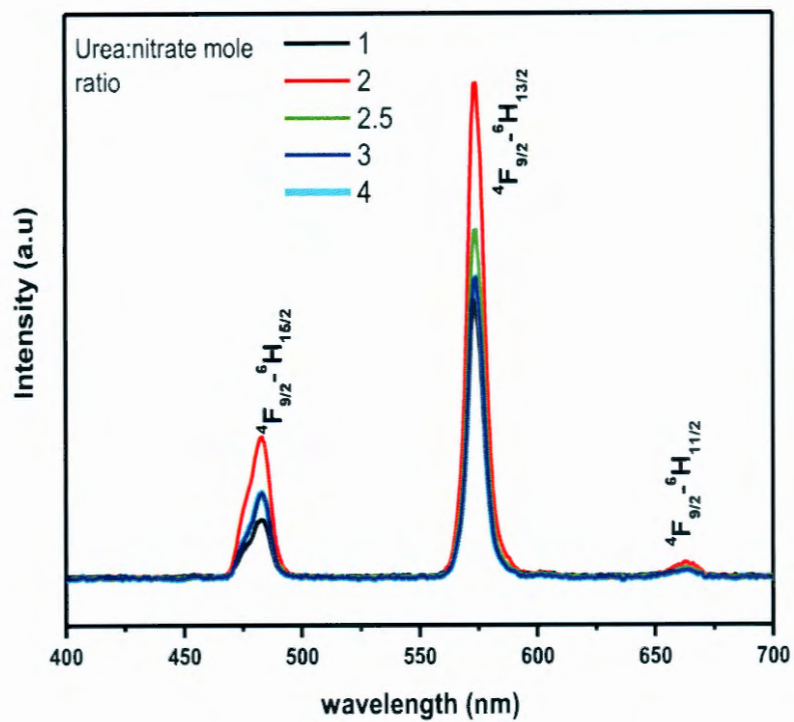


Figure 6.6: PL emission spectra of $\text{YVO}_4:\text{Dy}^{3+}$ with different ratio of urea:nitrate.

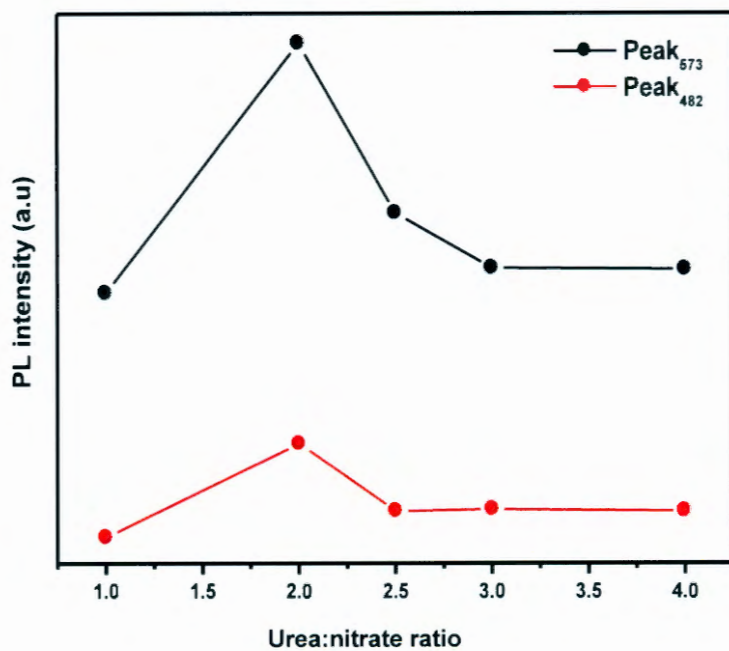


Figure 6.7: PL intensity of the ${}^4\text{F}_{9/2} \rightarrow {}^6\text{H}_{13/2}$ and the ${}^4\text{F}_{9/2} \rightarrow {}^6\text{H}_{15/2}$ transitions as a function of the ratio of urea:nitrate.

The optical band gap determined by extrapolating the linear portion of the reflection curve onto the energy (wavelength) E_g of $YVO_4:Dy^{3+}$ samples are in a range of 3.3 to 2.3 eV. This shows that the energy band gap decreased with an increase in the ratio of urea.

The PL excitation spectra of $YVO_4:Dy^{3+}$ monitored at 573 nm are shown in figure 6.5. The different ratio of urea was varied from 1 to 4. The excitation spectra consisted with a broad band from 220 nm to 340 nm. The band around 290 nm is associated with the charge transfer of Dy^{3+} . This charge transfer originates from interaction between Dy^{3+} and O^{2-} [20]. Figure 6.6 shows the emission spectra of $YVO_4:Dy^{3+}$ with different ratio of urea:nitrate prepared by combustion method at initiation temperature of 600°C. The emission spectra were obtained from excitation of 290 nm. The ratio of urea was varied from 1 to 4, and was used to determine the influence of urea on the luminescence properties.

The emission spectra consist of two main peaks, yellow-green band at 573 nm corresponding to ${}^4F_{9/2} \rightarrow {}^6H_{13/2}$ and the blue band at 482 nm corresponding to the ${}^4F_{9/2} \rightarrow {}^6H_{15/2}$ transition [21]. There is a very weak band at 663 nm which correspond to ${}^4F_{9/2} \rightarrow {}^6H_{11/2}$ transition. The intensity of yellow emission was stronger than that of the blue emission, this is because when the Dy^{3+} ions is located at low symmetry local sites with no inversion centres, the ${}^4F_{9/2} \rightarrow {}^6H_{13/2}$ transition is prominent in its emission spectrum [22]. The PL intensity as a function of ratio of urea for ${}^4F_{9/2} \rightarrow {}^6H_{13/2}$ and ${}^4F_{9/2} \rightarrow {}^6H_{15/2}$ transitions is shown in figure 6.7. It was found that the PL emission intensity for both transitions increased with an increase in the ratio of urea and reached a maximum at 2. The $YVO_4:Dy^{3+}$ generated the highest emission intensity due to the optimized heat release. With increasing the ratio of urea further, the intensity began to decrease because the excessively high urea concentration induced a large heat release [16].

As illustrated in figure 6.8 the emission colour of the $YVO_4:Dy^{3+}$ phosphor can be expressed by the corresponding CIE coordinates. The chromaticity coordinates for Dy was between 0.39 ~and 0.41 for the X coordinate and 0.44~0.46 for the Y coordinate which falls in the yellow region. Because of the green-yellow and blue emission colours the chromaticity coordinates approached the white colour. Figure 6.9 shows the luminescence decay curves for the ${}^4F_{9/2}$ level of the $YVO_4:Dy^{3+}$ powders. The curves were taken under the excitation and emission wavelength of 290 nm and 573 nm, respectively. The maximum initial luminescence intensity increased as the ratio of urea increases.

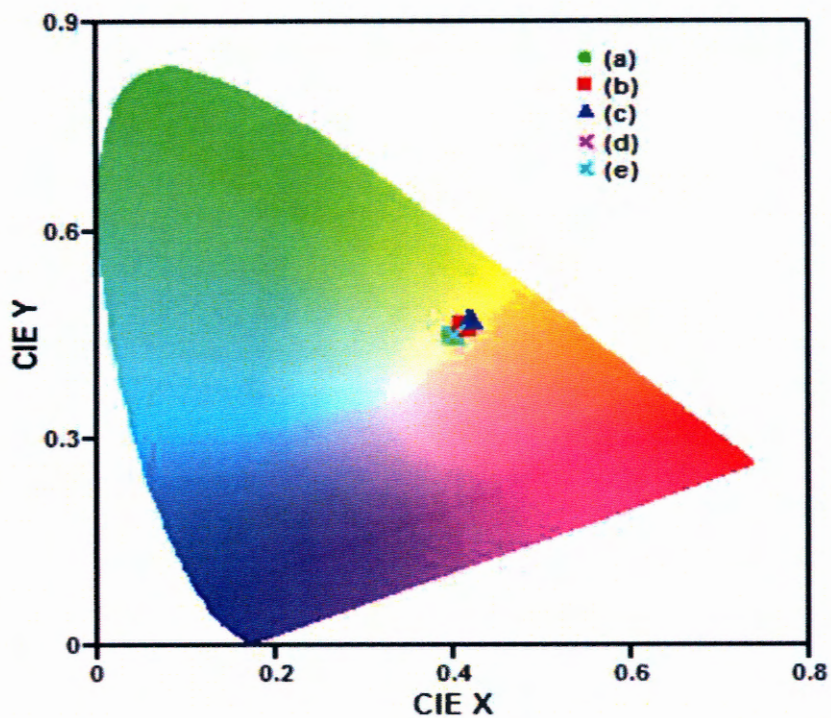


Figure 6.8: CIE chromaticity diagram showing the dependence of the emission colour with regard to the urea:nitrate ratio in the synthesized $\text{YVO}_4:\text{Dy}^{3+}$ powders.

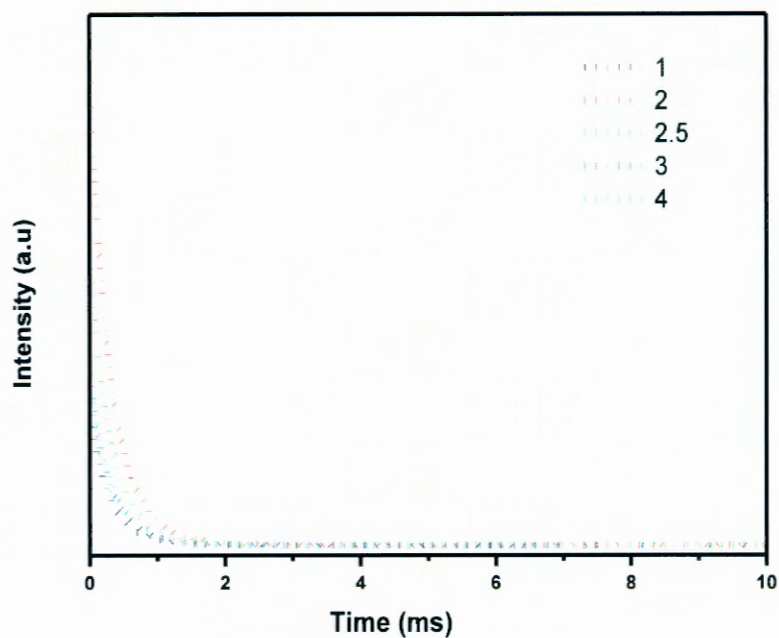


Figure 6.9: Luminescence decay curves of $^4\text{F}_{9/2}$ for $\text{YVO}_4:\text{Dy}^{3+}$ at different ratio of urea:nitrate.

The initial luminescence intensity observed when the addition ratio of urea was 2. But significant decreased in initial intensity was observed when the ratio of urea was increased up to 4. All the decay curves can be well fitted in a single exponential function. Lifetime values from the decay curves for 1, 2, 2.5, 3 and 4 ratio of urea were found to be 0.29, 0.32, 0.32, 0.31 and 0.35 ms.

6.3 Conclusion

YVO₄:Dy³⁺ phosphors have been synthesized by combustion method using the different ratio of urea as a fuel. XRD results revealed a single tetragonal phase (JCPDS No. 17-0341). No other crystalline phase was observed on the XRD spectra. It was observed that when increasing the concentration of urea further the flake-like particles was formed because an increase in urea increased the exothermic flame and hence the formation of crystalline structures. Under the excitation of 290 nm, the YVO₄:Dy³⁺ phosphor emitted yellow light at (574 nm) corresponding to the ⁴F_{9/2}→⁶H_{13/2} transition and the blue band (482 nm) corresponded to the ⁴F_{9/2}→⁶H_{15/2} transition. Because of the green-yellow and blue emission colours the chromaticity coordinates approached the white colour. All the decay curves were fitted with a single exponential function. The lifetime values from the decay curves for 1, 2, 2.5, 3 and 4 ratio of urea were found to be 0.29, 0.32, 0.32, 0.31 and 0.35 ms.

References

- [1] J. Wang, Y. Xu, M. Hojamberdiev, Y. Cui, H. Liu, G. Zhu, *J. of Alloys and Compounds* **479** (2009) 772-776.
- [2] Z. Xia, D. Chen, M. Yang, T. Ying, *J. of Physics and Chemistry of Solids*, **71** (2010) 175-180.
- [3] S. S. Yi, J. S. Bae, B. C. Choi, K. S. Shim, H. K. Yang, B. K. Moon, J. H. Jeong, J. H. Kim, *Optical Materials*, **28** (2006) 703-708.
- [4] Y. Dwivedi, S. B. Rai, *Optical Materials*, **31** (2009) 1472-1477.
- [5] S. Selvi, G. Venkataiah, S. Arunkumar, G. Muralidharan, K. Marimuthu, *Physica B Condensed Matter*, **454** (2014) 72-81.
- [6] H. Zhang, X. Fu, S. Niu and Q. Xin, *J. of Alloys and Compounds*, **457** (2008) 61-65.
- [7] H. Zhang, X. Fu, S. Niu, G. Sun, Q. Xin, *Materials Letters*, **61** (2007) 308-311.
- [8] L. Chen, G. Liu, Y. Liu, K. Huang, *J. of Materials processing technology*, **198** (2008) 129-133.
- [9] H. Xua, H. Wang, Y. Meng, H. Yana, *Solid State Communications*, **130** (2004) 465-468.
- [10] W. J. Park, M. K Jung, T. Masaki, S. Jim, D. H Yoon, *Materials Science and Engineering B*, **146** (2008) 95-98.
- [11] A. S. Mukasyan, J. D. E. White, *International Journal of Self-Propagating High-Temperature Synthesis*, **16** (2007) 154-168.
- [12] P. Huang, D. Chen, Y. Wang, *J. of Alloys and Compounds*, **509** (2011) 3375-3381.
- [13] H. T. Liu, Y. Liang, X. Gao, S. Zhang, X. Zhao, X. Chen, *J. of the Korean Physical Society*, **63(8)** (2013) 1615-1620.
- [14] S. Yao, D. Hen, *Optics and Laser Technology*, **40** (2008) 466-471.
- [15] A Sharma, O. P. Modi, G. K. Gupta, *Advances in Applied Science Research*, **13** (2012) 3819-3824.
- [16] B. Kim, Z. Hasan, J. Kim, *J. of Ceramic Processing Research*, **14** (2013) 601-605.
- [17] F. S. Husairi, S. Ali, A. Azlinda, M. Rusop, S. Abdullah, *J of Nanomaterials*, (2013) 163527 1-7.
- [18] C. F Bacalski, M. A. Cherry, G. A. Hirata, J. M. Mckittrick, J. Mourant, *Journal of the SID Supplement-1* (2000) 9398.
- [19] Y. Huang, Y. M. Yu, T. Tsuboi, H. J. Seo, *Optics Express*, **20** (2012) 4360-4368.
- [20] M. N. Luwang, R. S. Ningthoujam, S. K. Srivastava, R. K.r Vatsa, *J of Material Chemistry*, **21** (2011) 5326-5337.

- [21] V. B. Bhatkar, *J. of Engineering Science and Innovative Technology*, **2** (2013) 426-432.
- [22] Y. Li, Y. Chang, Y. Lin, Y. Chang, Y. Lin, *Journal of Alloys and Compounds*, **439** (2007) 367-375.

Effect of substrate temperature on structure and luminescence properties of YVO₄:Eu thin films grown by PLD

7.1 Introduction

Yttrium vanadate has been shown to be a useful phosphor host lattice. The vanadates are prepared by combining vanadium pentoxide with oxide or carbonates of metals with calculated quantities, or by ammonium metavanadate with carbonates or nitrates. Vanadates are doped with rare earth ions to produce emitting phosphors [1]. YVO₄:Eu³⁺ is an important red emitting phosphor materials with main lines at 594 nm (⁵D₀-⁷F₁), 618 nm (⁵D₀-⁷F₂), 699 nm (⁵D₀-⁷F₄) [2]. YVO₄:Eu³⁺ materials are used in flat panel display for its good colour purity [3,4]. The energy transfer from VO₄³⁻ to Eu³⁺ is highly efficient because of a strong absorption to ultraviolet light by YVO₄ [5, 6]. A number of techniques were used to prepare YVO₄ thin film such as chemical vapour deposition [7], sol-gel methods [8], spray pyrolysis [9], Radio frequency magnetron sputter deposition [10]. But these techniques produce films that lack crystallographic orientation control. YVO₄:Eu³⁺ thin films were also deposited by pulse laser deposition (PLD). It allows the deposition of films of good crystalline quality at lower temperatures in different gas environments. PLD is a technique that produce stoichiometric structures that transports materials from the target to the substrate to grow high quality crystalline films [11]. The results of *Milev et al* showed that the crystallinity of the films at deposition temperatures higher than 500°C [12]. In this study the crystallinity of the thin films was observed at higher deposition temperatures. The effects of the deposition temperature and the deposition background pressure on the structural and luminescence properties of the thin films was also studied.

7.2 Results and discussion

7.2.1 Structure of YVO₄:Eu thin films

Figure 7.1 shows the XRD spectra of YVO₄:Eu³⁺ phosphor thin films deposited by pulse laser deposition on silicon substrate. The substrate temperature was varied from 200 to 400°C.

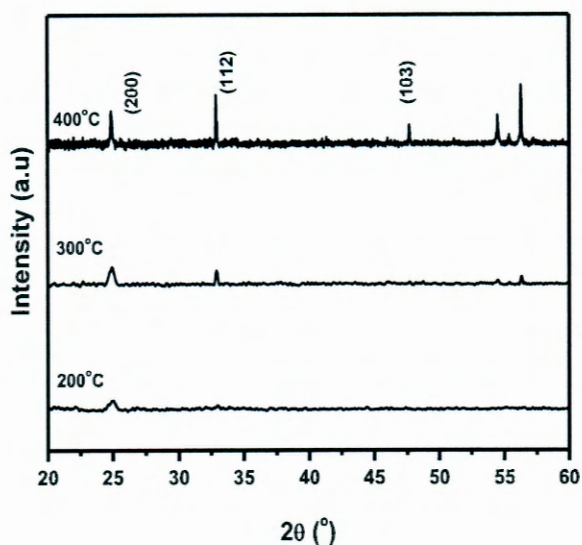


Figure 7.1: XRD spectra of $\text{YVO}_4:\text{Eu}^{3+}$ thin films deposited at various substrate temperatures (200, 300 and 400°C).

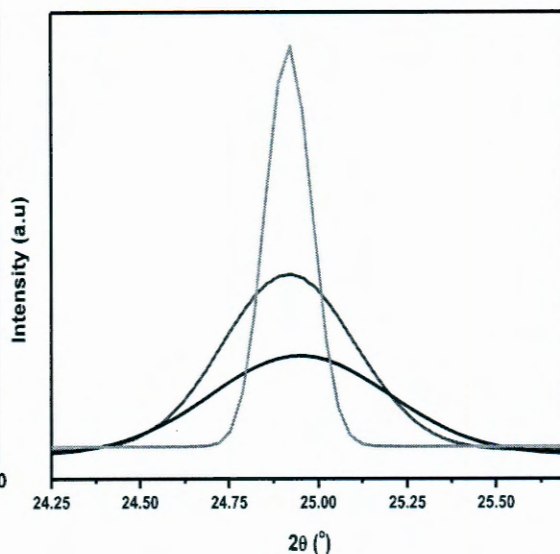


Figure 7.2: XRD powder diffraction of (200) peak for $\text{YVO}_4:\text{Eu}^{3+}$ thin films deposited at various substrate temperatures (200, 300 and 400°C).

The diffraction peaks of the thin films are matched with that of tetragonal phase standard JCPDS card 17-0341 and there were no impurities that were observed. At a deposition temperature of 200 °C the spectra showed a small and broader peak at (200) orientation. The crystallinity improves for samples deposited at higher substrate temperatures [13]. At 400°C substrate temperature the phosphor thin film showed a crystalline structure with narrow and sharper peaks. The substrate temperature did not show any influence on a peak position as shown in figure 7.2. The value of the particle size was estimated using Scherrer's equation along the (200) direction. The particle size range from 16 nm at 200°C, 20 nm at 300°C to 67 nm at 400°C.

7.2.2 Morphology of $\text{YVO}_4:\text{Eu}$ thin film

Figure 7.3 shows the SEM images of $\text{YVO}_4:\text{Eu}^{3+}$ thin films deposited at substrate temperature of 200 and 400°C. Films deposited at 200°C is composed of small spherical particles of different sizes. SEM images indicated that with increasing in deposition temperature the particles becomes larger. This increase in particle size agrees well with the XRD results showing decrease in full width at half maxima. AFM images of the $\text{YVO}_4:\text{Eu}^{3+}$ thin films grown at different deposition temperature are shown in figure 7.4.

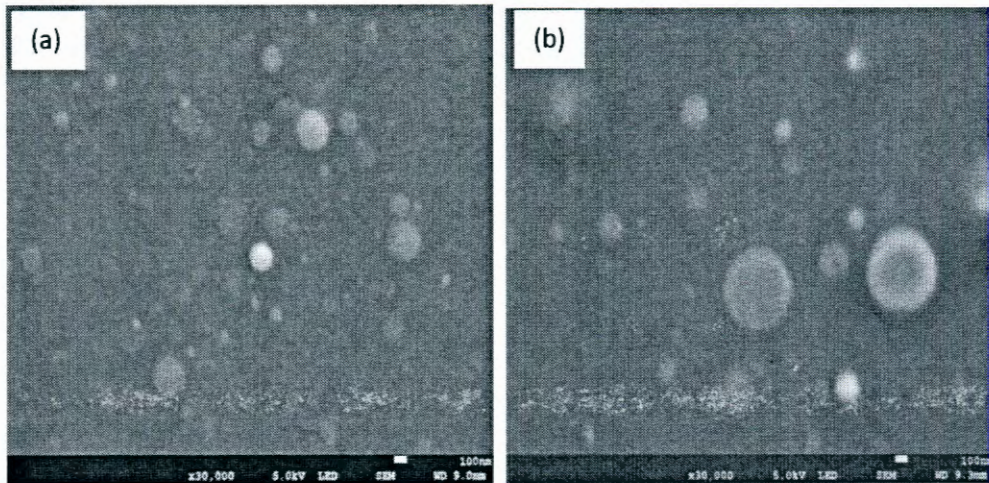


Figure 7.3: SEM images of $\text{YVO}_4:\text{Eu}^{3+}$ thin films deposited at (a) 200°C and (b) 400°C.

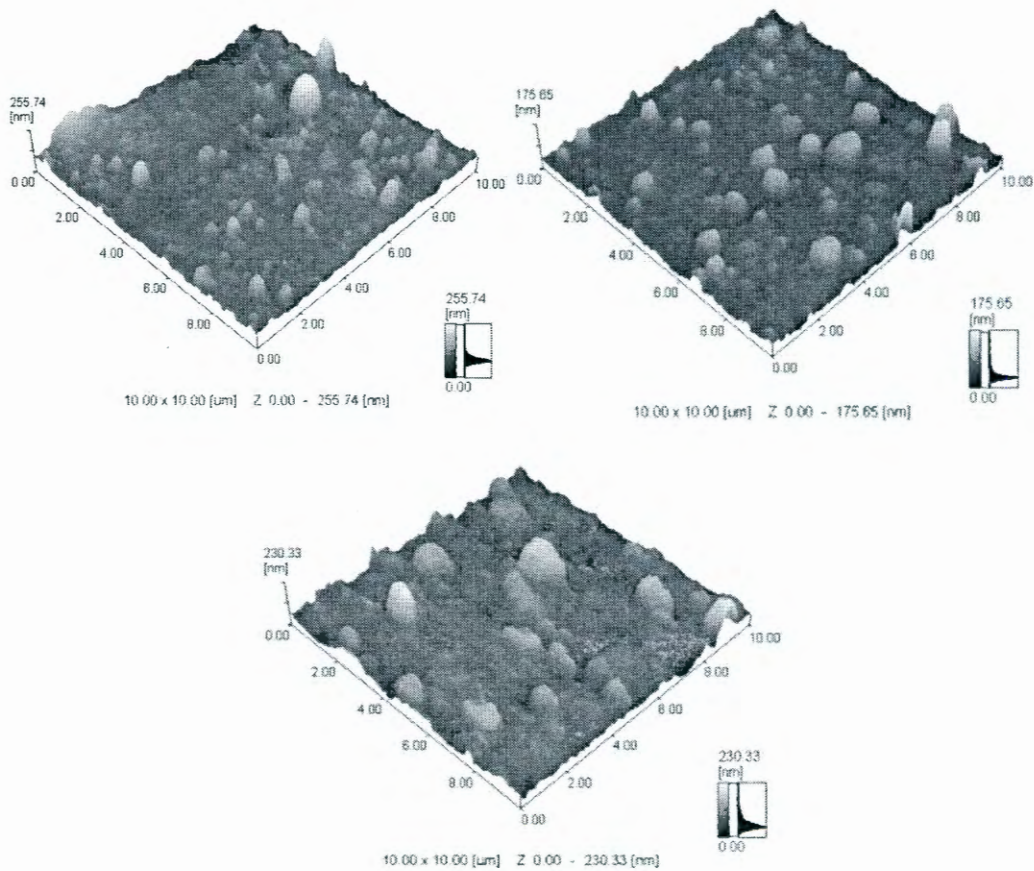


Figure 7.4: AFM images of $\text{YVO}_4:\text{Eu}^{3+}$ thin films deposited at (a) 200°C (b) 300°C and (c) 400°C.

The thin films deposited at lower temperature 200°C showed a smooth surface with small particles. When the deposition temperature increased, the thin films showed a rough surface. The roughness of the surface maybe due to the formation of the sample crystallinity as confirmed by XRD results [14]. The large particles were observed at 400°C deposition temperature. The rms thickness of the thin films at 200, 300 and 400°C were 10.8, 17.8 and 29.7 nm, respectively.

7.2.3 Photoluminescence properties of $YVO_4:Eu$ thin films

Figure 7.5 show the PL excitation spectra of $YVO_4:Eu^{3+}$ thin films for the emission of 618 nm. The spectra showed a broad band between 230 and 360 nm. This band corresponds to the V-O charge transfer transition from the VO_4^{3-} groups of the host to Eu^{3+} ions [15]. It was observed that the excitation intensity increased with an increase in substrate temperatures. This may be due to the energy transfer from the host YVO_4 to Eu is enhanced with the increase of deposition temperature [16]. The PL spectra in figure 7.6 show the emission peaks of $YVO_4:Eu^{3+}$ thin films deposited at different temperature. Emission spectra showed the peaks at 594, 618, 652 and 699 nm corresponding to ${}^5D_0-{}^7F_1$, ${}^5D_0-{}^7F_2$, ${}^5D_0-{}^7F_3$ and ${}^5D_0-{}^7F_4$, respectively [17]. The insert shows the graph of PL intensity as a function of deposition temperature. The spectra showed an increase in intensity when deposition temperature increased and the maximum intensity was reached at 400°C.

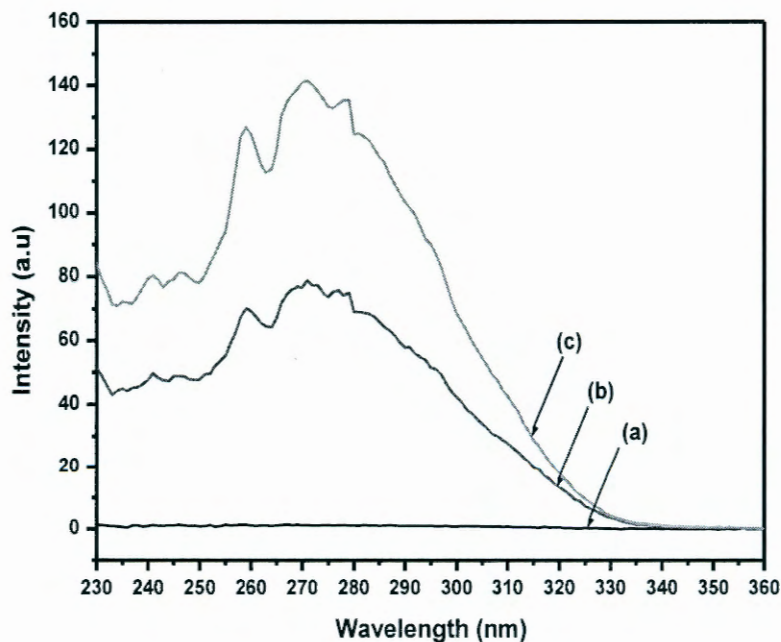


Figure 7.5: PL excitation spectra of $YVO_4:Eu^{3+}$ thin films deposited at substrate temperature of (a) 200 °C (b) 300 °C and (c) 400 °C.

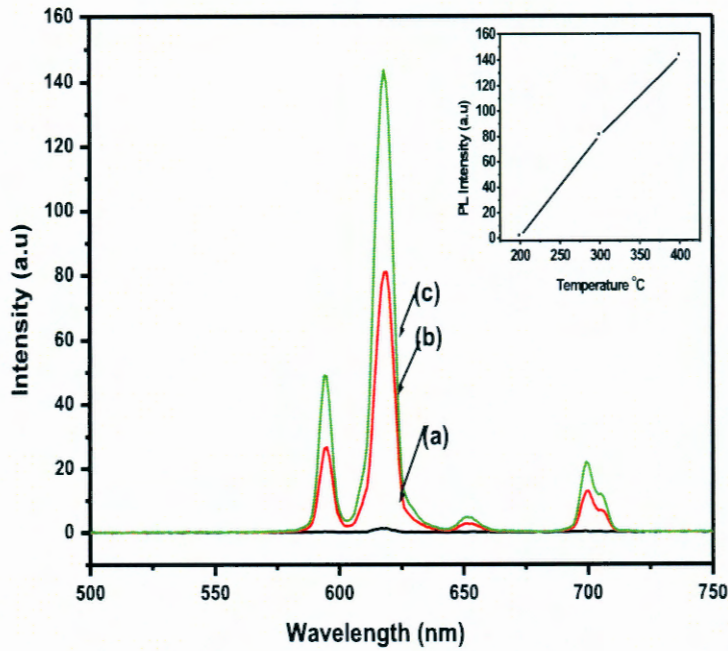


Figure 7.6: PL emission spectra of $\text{YVO}_4:\text{Eu}^{3+}$ thin films deposited at substrate temperature of (a) 200°C (b) 300°C and (c) 400°C .

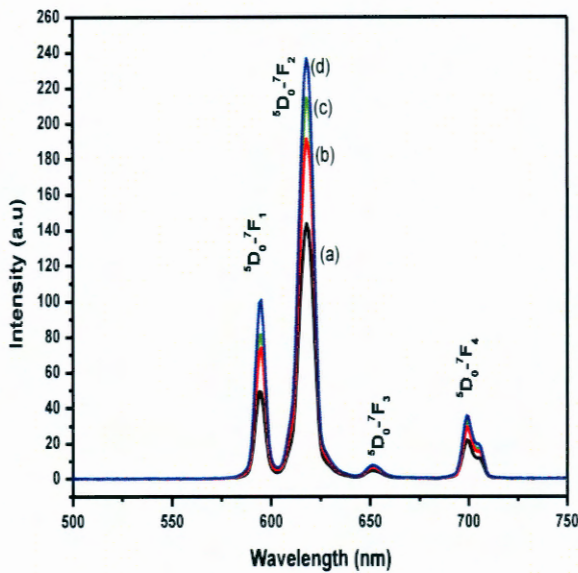


Figure 7.7: PL emission spectra of $\text{YVO}_4:\text{Eu}^{3+}$ thin films deposited at 400°C at 20, 50, 72 and 85 mTorr.

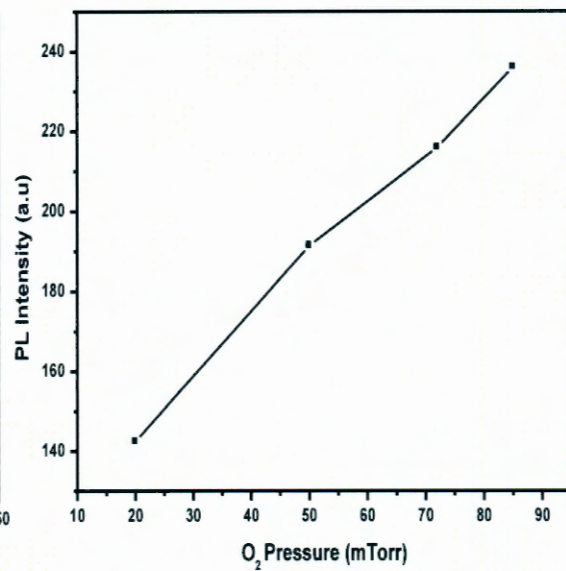


Figure 7.8: PL intensity of $\text{YVO}_4:\text{Eu}^{3+}$ thin films as a function of oxygen pressure in mTorr.

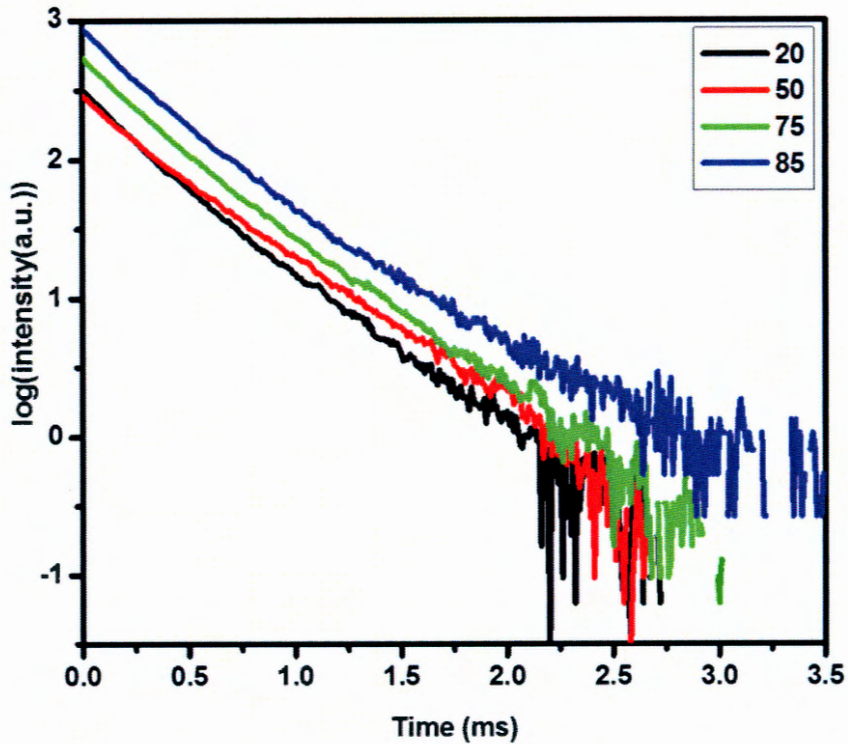


Figure 7.9: Luminescence decay curve of $\text{YVO}_4:\text{Eu}^{3+}$ thin films deposited at 20, 50, 72 and 85 mTorr Observed at 618 nm emission and 6270 excitation under 400°C.

Figure 7.7 shows the emission spectra of $\text{YVO}_4:\text{Eu}^{3+}$ thin films deposited at 400°C and different oxygen pressure. The oxygen pressure was varied from 20, 50, and 72 to 85 mTorr. The emission spectra showed the increase in intensity with increase in deposition pressures. The intensity as a function of oxygen pressure was shown in figure 7.8. It was found that the intensity of the electric dipole ${}^5\text{D}_0\text{-}{}^7\text{F}_2$ transition of Eu at 618 nm increased with oxygen pressure. This shows the PL enhancement and the formation of the roughness by laser ablation at higher oxygen pressure [18]. The luminescence decay curves of $\text{YVO}_4:\text{Eu}^{3+}$ ${}^5\text{D}_0\text{-}{}^7\text{F}_2$ electric dipole transition of Eu at 618 nm emission under 270 nm excitation deposited at various oxygen pressure at 400 °C are shown in figure 7.9. The decay curves can be well fitted with a double exponential function. The calculated life times for 20 mTorr were $t_1=0.25$ and $t_2=0.82$ ms, 50 mTorr are $t_1=0.41$ and $t_2=0.61$ ms, 72 mTorr are $t_1=0.26$ and $t_2=0.68$ ms and 85 mTorr $t_1=0.23$ and $t_2=0.64$. The results showed an increase in the initial luminescence intensity, but the decay time varied as the oxygen partial pressure increased. To study the electronic interactions near the optical band gap region of $\text{YVO}_4:\text{Eu}^{3+}$ thin-film

samples, diffuse reflectance measurements were taken on the samples in the UV–Vis region at room temperature. All spectra were obtained in the range of 200–800 nm. Figure 10 (a) shows the diffuse reflectance spectra, R , as a function of wavelength. It can be seen that films transmit and absorb significantly at wavelength below 600 nm but reflects more in the visible region. It is suggested that the PL intensity strongly depends on the scattering rate of the film [19]. It is observed from the results that scattering rate reduces with an increase in oxygen partial pressure; hence, the reflectance of the $\text{YVO}_4:\text{Eu}^{3+}$ thin-film samples in the visible region reduces significantly with the increase in the oxygen partial pressure. The band gap energy of the doped $\text{YVO}_4:\text{Eu}^{3+}$ thin-film samples was calculated from the diffuse reflectance spectra by plotting the square of the Kubelka–Munk function $F(R)^2$ versus the energy in electron volts and shown in Fig. 10 (b). The linear part of the curve was extrapolated to $F(R)^2 = 0$ to calculate the direct band gap energy. As the oxygen pressure increases from 20 to 85 mTorr, the band gap decreases. The reduction in band gap with oxygen partial pressure is due to the increase in oxygen vacancies in the $\text{YVO}_4:\text{Eu}^{3+}$ thin films. Since larger concentrations of vacancies offer higher defect states near the conduction band edge, this effectively leads to decrease in the optical band gap. The content of oxygen vacancies increases with oxygen partial pressure, and hence, carrier concentration decreases. So the band gap decreases from 3.77 to 3.26 eV with increase in oxygen partial pressure from 20 to 85 mTorr.

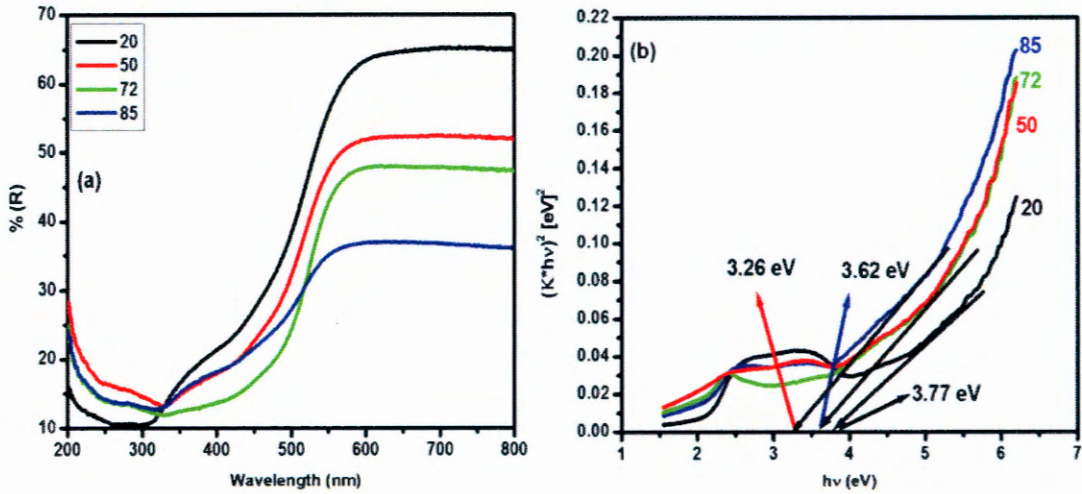


Figure 7.10: (a) Diffuse reflectance and (b) band gap energy of the $\text{YVO}_4:\text{Eu}^{3+}$ thin films deposited at 20, 50, 72 and 85 mTorr.

7.3 Conclusion

YVO₄:Eu³⁺ thin films were deposited by PLD under the various substrate temperature and oxygen pressures. The diffraction peaks of the thin films showed the tetragonal phase structure. An increase in substrate temperature led to an improvement in crystallinity and the roughness of the surface of YVO₄:Eu³⁺ thin films. The emission spectra showed an increase in intensity when deposition temperature increased and also when the oxygen pressure increased. It has been shown that the surface morphology and the luminescence of the thin films can be enhanced by increasing the substrate temperature and by increasing the oxygen pressure.

References

- [1] Z. Xia, D. Chen, M. Yang, T. Ying, *J. of physics and chemistry of solids*, **71** (2010) 175-180.
- [2] V. Kumar, A. F. Khan, S. Chawla, *J. Phys. D: Appl. Phys.* **46** (2013) 365101-1-365101-9.
- [3] J. H. Kang, M. Nazarov, W. B. Im, *J. Vac. Sci. Technol.*, B **23**(2) (2005) 843-848.
- [4] B. K. Grandhe, V. R. Bandi, K. Jang, S. Ramaprabhu, S. Yi, J. Jeong, *Electronic Materials Letters*, **7**(2) (2011) 161-165.
- [5] G. Wang, W. Qin, D. Zhang, L. Wang, G. Wei, P. Zhu, R. Kim, *J. Phys. Chem. C*, (44) (2008) 17042-17045.
- [6] V. Pankratov, A. I. Popov, L. Shirmane, A. Kotlov, and C. Feldmann, *Journal of Applied Physics* **110** (2011) 053522-053527.
- [7] G. R. Bai, H. Zhang, C. M. Foster, *Thin Solid Films*. **325**(1–2) (1998) 115–122.
- [8] S. Hirano, T. Yogo, K. Kikuta, W. Sakamoto, H. Koganei, *J. of the American Ceramic Society*, **79**(12) (1996) 3041–3044.
- [9] D. Perednis, L. J. Gauckler, *J. of Electro ceramics*, **14** (2005) 103–111.
- [10] J. H. Kang, J. Han, H. Jang, H. S. Yoo, S. J. Yun, D. Y. Jeon, *IMID '07 DIGEST* 1547.
- [11] D. B. Geohegan, D. N. Mashburn, R. J. Culbertson, S. J. Pennycook, J. D. Budai, R. E. Valiga, B. C. Sales, D. H. Lowndes, L. A. Boatner, E. Sonder D. Eres, D. K. Christen, W. H. Christie, *J. Mater. Res.* **3**(6) (1988).
- [12] D. R. Milev, P. A. Atanasov, A. Og. Dikovska, I. G. Dimitrov, K. P. Petrov, G. V. Avdeev, *Applies Surface Science*, **253** (2007) 8250-8253.
- [13] E. Atanassova, M. Kalitzova, G. Zollo, A. Paskaleva, A. Peeva, M. Georgieva, G. Vitali, *Thin Solid Films*, **426** (2003) 191–199,
- [14] D. Kim, W. Kang, *Bull. Korean Chem. Soc.*, **25**(12) (2004) 1859-1862.
- [15] G. Chu, X. Wang, T. Chen, W. Xu, Y. Wang, H. Song, Y. Xu, *J. Mater. Chem. C*, **3** (2015) 3384-3390.
- [16] W. Kang, J. Park, D. Kim, K. Suh, *Bull. Korean Chem. Soc.*, **22**(8) (2001) 921-924.

- [17] Yu. A. Dolinskaya, I. E. Kolesnikova, A. V. Kurochkina, A. A. Man'shina, M. D. Mikhailov, A. V. Semencha, *J. of Glass Physics and Chemistry*, **9** (2013) 308–310.
- [18] C. Wang, B. L. Cheng, S. Y. Wang, H. B. Lu, Y. L. Zhou, Z. H. Chen, G. Z. Yang, *Thin Solid Films*, **485** (2005) 82 – 89.
- [19] G. Dantelle, B. Fleury, J.P. Boilot, T. Gacoin, *ACS Appl. Mater. Interfaces* **5(21)** (2013) 11315–11320.

Optimizing deposition time to enhanced photoluminescence properties of laser-ablated red Eu^{3+} doped YVO_4 thin films.

8.1 Introduction

The interest in thin films phosphors are growing due to their potential application in high resolution devices. Among these thin films phosphors, there has been significant research in the development of oxide based red phosphor materials. $\text{Y}_2\text{O}_3:\text{Eu}$ was one of the red materials used for field emission display (FED) devices. *S. L Jones et al* [1] found that the $\text{Y}_2\text{O}_3:\text{Eu}$ require a high temperature to crystallize. However, the FED devices require the low temperature [2]. Because of its low melting point, $\text{YVO}_4:\text{Eu}^{3+}$ thin films are promising luminescent materials for FED device. $\text{YVO}_4:\text{Eu}^{3+}$ is a highly efficient red light-emitting material, because of its strong absorption of ultraviolet light and an effective energy transfer from VO_4 to Eu^{3+} [3-5]. A number of techniques were recently used for the development of YVO_4 thin films growth, such as chemical vapour deposition (CVD) [6, 7], spray pyrolysis [8, 9], solid state reaction [10] and sol-gel methods [11-13]. In general, these techniques need complicated, and expensive equipment set-ups, and complicated processing [14]. $\text{YVO}_4:\text{Eu}^{3+}$ was deposited by pulse laser deposition (PLD). It is well known that the importance of the PLD deposition is the stoichiometric transfer of target material to the substrate [15]. In this study, $\text{YVO}_4:\text{Eu}^{3+}$ thin films were grown in a fixed oxygen pressure. The variation in deposition time was used to improve the crystallinity and to enhance the luminescence of the thin films. It is well known that longer the deposition time results in thick films [16]. As reported by other researcher, *Kassima et al* prepared ZnS thin films and found that increasing the deposition time improves the crystallinity of the thin film [16]. Another study on the effect of deposition time on $\text{YVO}_4:\text{Eu}^{3+}$ thin films [15] showed that the best results were obtained when the annealed temperature increased and thin films were deposited for 60 minutes. Many studies on $\text{YVO}_4:\text{Eu}^{3+}$ thin films showed that the improvement of the crystallinity is due to the increasing of annealing temperature [15, 2]. In this work we report the optimization of deposition time to improve the crystallinity and enhanced the photoluminescence properties of the $\text{YVO}_4:\text{Eu}$ films deposited at 5 mTorr oxygen pressure.

8.2 Results and discussion

The x-ray diffraction patterns results of $\text{YVO}_4:\text{Eu}^{3+}$ thin film deposited at different deposition times of 30 minutes, 45 minutes and 60 minutes in 5 mTorr oxygen pressure at room temperature are shown in figure 8.1. The diffraction peaks observed have been analysed and are match well with those of tetragonal phase (JCPDS card #17-3441) [17]. The peaks observed at 25.04° and 33.07° match with reflections from (200) and (112) crystallographic planes of tetragonal phase of $\text{YVO}_4:\text{Eu}^{3+}$, respectively. The poor crystallinity was observed at the deposition time of 30 minutes. It was observed that the crystallinity improved after the deposition time of 45 minutes, and the best film was observed after the deposition time of 60 minutes. From figure 8.1, it is clear that by increasing the deposition time the preferred orientation is (200). *Kang et al* shows the relatively well preferred orientation of (200) plane [2]. *Yi et al* [18] reported that the nucleation of grains with (200) orientation is energetically favourable at lower deposition temperatures. Other researchers observed that with an increase in substrate temperature of PLD the crystallinity of the $\text{YVO}_4:\text{Eu}$ improved [18]. It clearly seen that by drawing the XRD orientation of (200) peak from figure 8.2, the effect on XRD intensity was observed when varying the deposition time. The thickness of $\text{YVO}_4:\text{Eu}^{3+}$ thin films increases and the crystallinity was improved. The grain sizes were estimated using the Debye-Scherrer's formula [19].

$$D = \frac{0.9\lambda}{\beta \cos\theta} \quad (5)$$

Where D is the grain size, λ is x-ray wavelength, β is a width at half maximum intensity (FWHM) and θ is the Bragg angle. The average grain size was found to be 60 nm. It was found that the estimated grain size increase with the increase in the deposition time as shown in figure 8.3. The estimated grain size was calculated using the (200) plane. The improvement in estimated grain size maybe due to the fact that free molecules have tendency to condense on the surface of larger particles therefore, all smaller particles shrink, while larger particles grow, and overall the average size will increase [20].

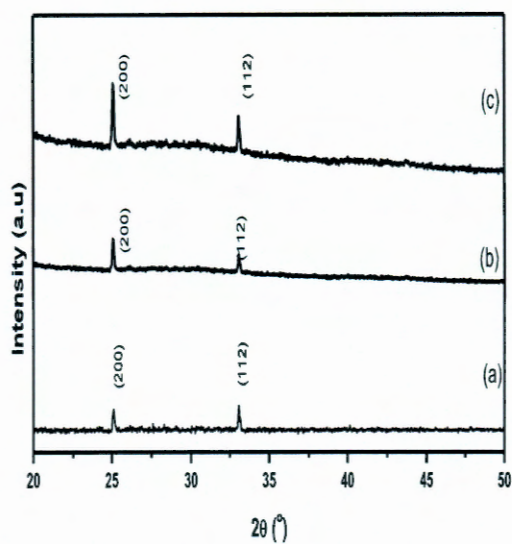


Figure 8.1: XRD patterns of $\text{YVO}_4:\text{Eu}^{3+}$ deposited at (a) 30, (b) 45 and (c) 60 minutes.

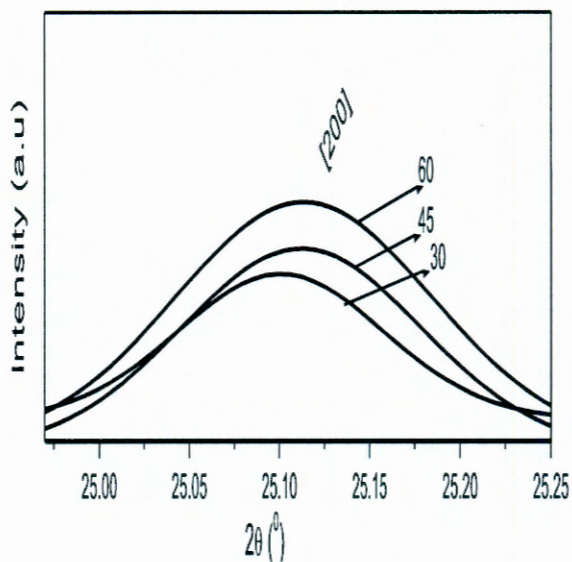


Figure 8.2: XRD powder diffraction patterns of [200] for $\text{YVO}_4:\text{Eu}^{3+}$ (a) 30, (b) 45 and (c) 60 minutes.

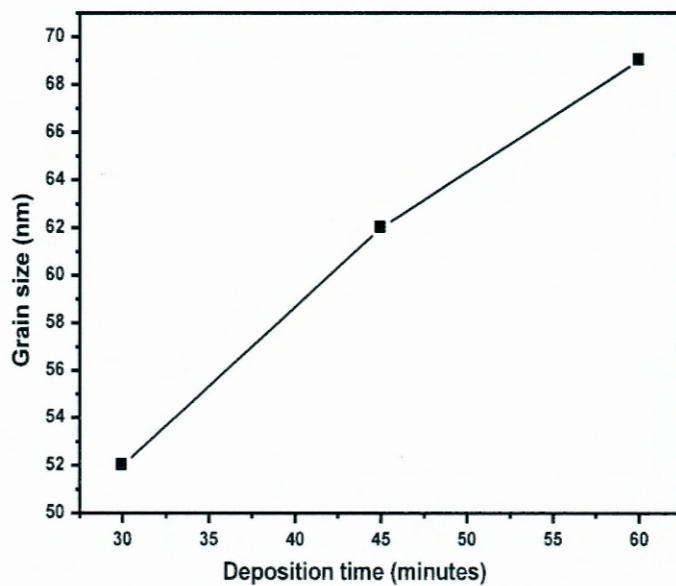


Figure 8.3: average grain size as a function of deposition time for (200) plane.

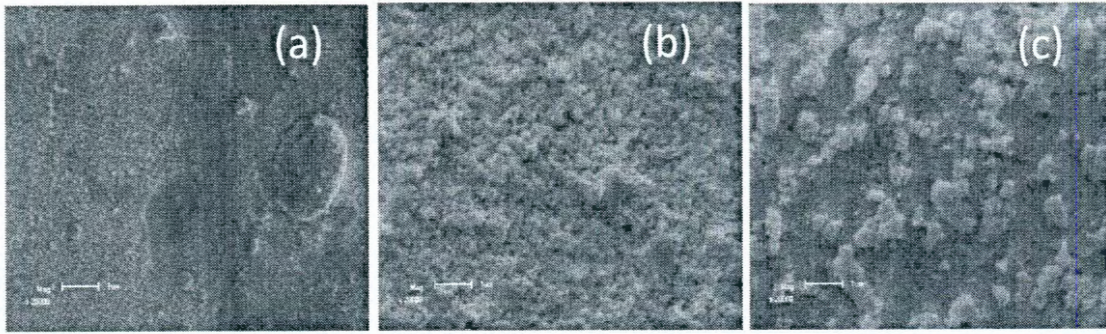


Figure 8.4: SEM images of the $\text{YVO}_4:\text{Eu}^{3+}$ thin films deposited at different times (a) 30, (b) 45 and (c) 60 minutes in 5 mTorr at room temperature.

The surface morphology of the films obtained with different deposition times at room temperature were determined by scanning electron microscopy (SEM) and is shown in figure 8.4. SEM image shows the small grain size particles for sample deposited at low deposition time. The formation of homogenous surface was observed after a films deposited at 45 minutes. The grain size of the films are generally small, this can be attributed to the deposition at room temperature at which ions in the bath do not possess enough mobility to form a larger grains. Rough surface and larger grain particles appear in sample with higher deposition time of 60 minutes. The crystallinity of the samples increased with an increase in deposition time, this is confirmed by XRD results.

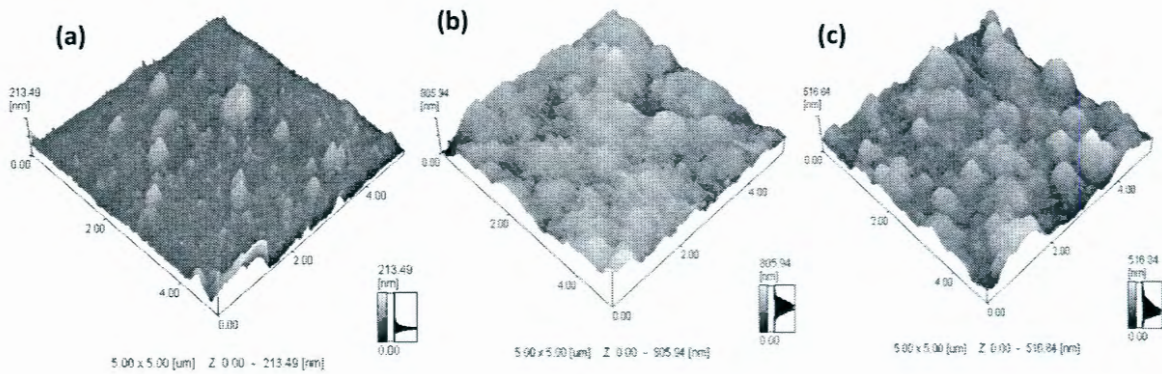


Figure 8.5: AFM images for $\text{YVO}_4:\text{Eu}^{3+}$ thin films deposited at different deposition times (a) 30, (b) 45 and (c) 60 minutes at 5 mTorr.

The AFM results were recorded to study the effect of deposition time on surface of the $\text{YVO}_4:\text{Eu}$ thin films. Figure 8.5 shows the 3D AFM images of the $\text{YVO}_4:\text{Eu}^{3+}$ thin films

obtained by various deposition times of 30, 45 and 60 minutes at room temperature. The surface of the sample deposited after 30 minutes consist of irregular and spherical particles. The grain size grows slightly as the deposition time increased to 45 minutes, the surface of the thin film became smooth and the surface layer was well uniformed and agglomerated, this shows that the substrate is well covered with particles. This may be due to the fact that the growth takes place by diffusion when deposition time is long enough [21]. The film deposited for 60 minutes have the largest grain size and produce the roughest surface morphology. The roughness of the films was found to increase from 2.26 nm, 7.4 nm to 24.20 nm as the deposition time increased from 30 minutes, 45 minutes to 60 minutes as shown in figure 8.6. The AFM results illustrate that the deposition time significantly affect the grain size, film thickness and surface roughness of $\text{YVO}_4:\text{Eu}^{3+}$ thin films. The SEM results illustrated in figure 8.4 are consistent with the AFM results.

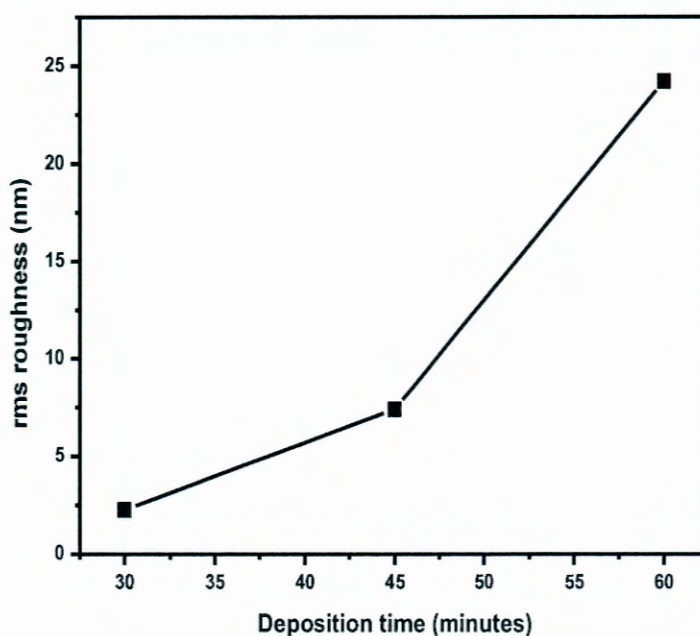


Figure 8.6: rms roughness as a function of deposition time.

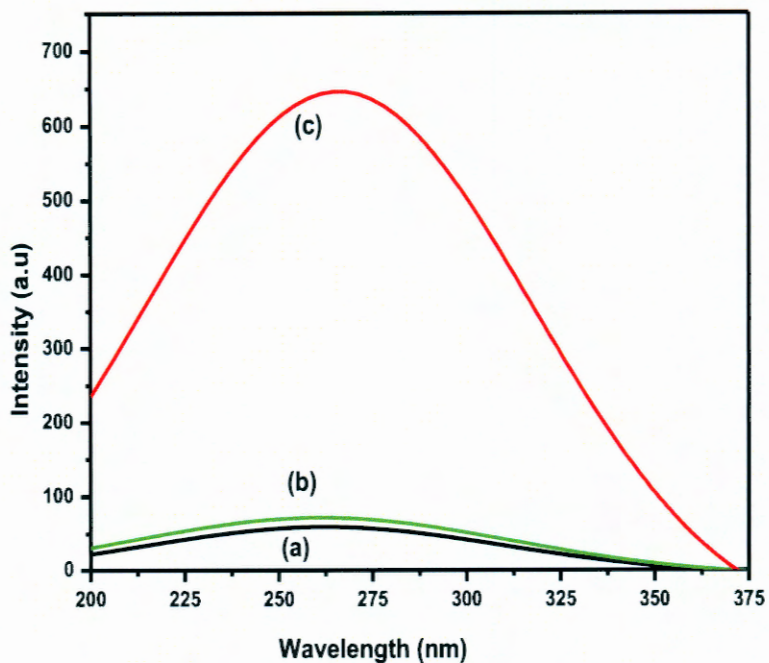


Figure 8.7: Excitation spectra of the $\text{YVO}_4:\text{Eu}^{3+}$ thin films deposited at different deposition time of (a) 30 (b) 45 and (c) 60 minutes.

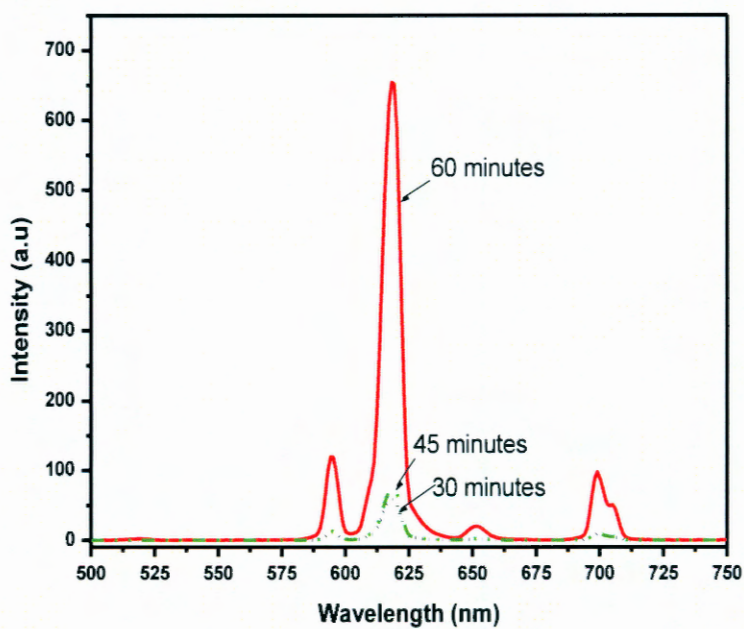


Figure 8.8: emission spectra of the $\text{YVO}_4:\text{Eu}^{3+}$ thin films deposited at different deposition time of 30, 45 and 60 minutes.

Figure 8.7 shows the PL excitation spectra of $\text{YVO}_4:\text{Eu}^{3+}$ thin films obtained for deposition time ranging from 30 to 60 minutes. The PL excitation spectra consist of a broad band between 200 nm and 350 nm. The broad excitation band is due to the charge transfer transition between Eu^{3+} and VO_4^{3-} anions [22]. Figure 8.8 shows PL emission spectra of $\text{YVO}_4:\text{Eu}^{3+}$ with deposition time between 30 minutes and 60 minutes. The main emission peaks are due to the Eu^{3+} transition ${}^5\text{D}_j \rightarrow {}^7\text{F}_j$. The strongest red emission peak at 618 nm is due to transition ${}^5\text{D}_0 \rightarrow {}^7\text{F}_2$. The deep red emission peak at 703 nm is due to the transition ${}^5\text{D}_0 \rightarrow {}^7\text{F}_4$. The shorter wavelength peaks at 594 nm and 651 nm correspond to the transition ${}^5\text{D}_0 \rightarrow {}^7\text{F}_1$ and ${}^5\text{D}_0 \rightarrow {}^7\text{F}_3$, respectively.

It is well known that these narrow emission peaks are due to the Eu^{3+} , thus is because of the shielding effect of $4f$ electrons by $5s$ and $5p$ electrons at the europium ions. The emission intensity enhanced with increasing deposition time without changing peak position. This improvement in PL intensity firstly is due to the improvement of the crystallinity leading to higher oscillator strengths for optical transitions [23]. Secondly may be due from the reduced internal reflections of emitted light due to rougher surface at high deposition time [18]. The incorporation of Eu^{3+} ions in the YVO_4 host also contributes to the enhancement of emission intensity [24]. Figure 8.9 shows the relation between the PL intensity and deposition time of $\text{YVO}_4:\text{Eu}^{3+}$ thin films. The intensity of the thin films increased with an increase in deposition time. This concludes that the intensity depends on the deposition time. The chromaticity diagram in figure 8.10 confirms the red $\text{YVO}_4:\text{Eu}^{3+}$ thin films with (0.675, 0.324) coordinates.

Figure 8.11 shows the luminescence decay for the ${}^5\text{D}_0$ level of Eu^{3+} in $\text{YVO}_4:\text{Eu}^{3+}$ samples deposited at different deposition time (30, 45 and 60 minutes). Excitation and emission wavelengths are fixed at 275 nm and 618 nm, respectively. The decay curves are exponential for all the cases and can be well-fitted with a double-exponential function as:

$$I(t) = I_0 + A_1 \exp(-t/t_1) + A_2 \exp(-t/t_2) \quad (6)$$

Where I and I_0 are the luminescence intensity at time t and 0, A_1 and A_2 are constants, t is the time; t_1 and t_2 are the decay times for the exponential components, respectively. The average decay lifetimes can be calculated using the formula.

$$t_{ave} = (A_1 t_1^2 + A_2 t_2^2) / (A_1 t_1 + A_2 t_2) \quad (7)$$

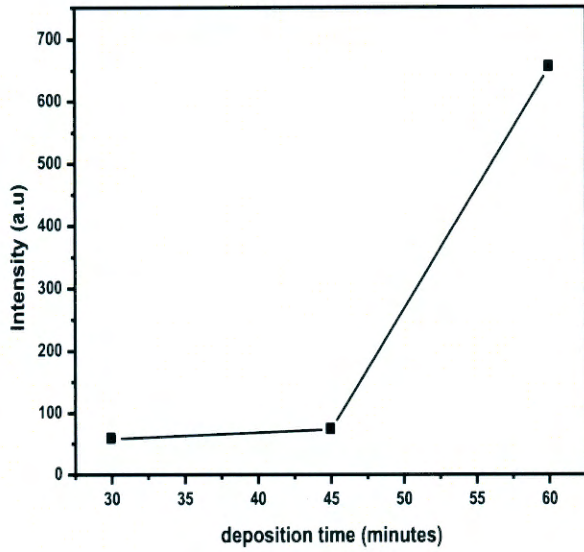


Figure 8.9: PL intensity as a function of deposition time.

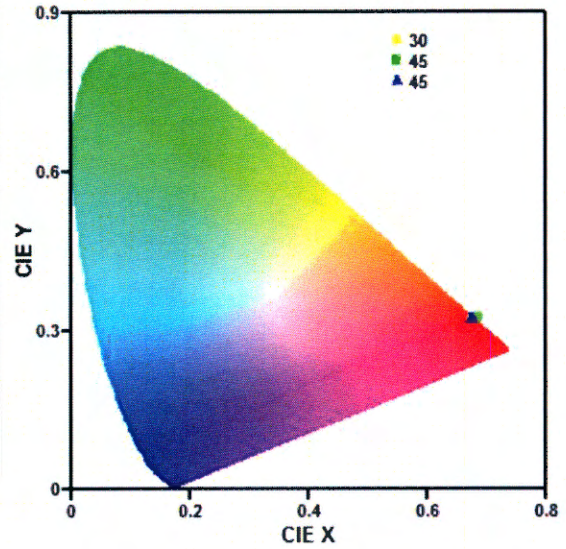


Figure 8.10: CIE chromaticity diagram showing the red emission colour for $\text{YVO}_4:\text{Eu}^{3+}$ thin films.

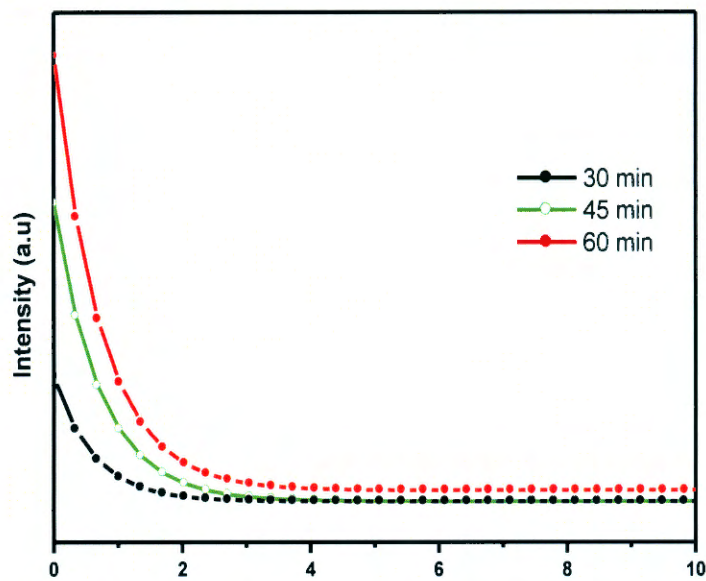


Figure 8.11: luminescence decay curves of $\text{YVO}_4:\text{Eu}^{3+}$ thin films deposited at different deposition time of 30, 45 and 60 minutes.

Luminescence average lifetimes listed in table 1 are increased from 0.208 ms to 0.578 ms in the $\text{YVO}_4:\text{Eu}^{3+}$ sample. From our results analysis it is clear that the crystallinity and roughness of the phosphor thin films have strongly affected the photoluminescence

properties. Other researchers [18] observed the same behaviour but they were varying the substrate temperature.

Table 1: The values of calculated life times

Deposition time (min)	t_1 (ms)	t_2 (ms)	t_{ave} (ms)
30	0.02	0.59	0.208
45	0.04	0.64	0.213
60	0.08	0.71	0.578

8.3 Conclusion

The $YVO_4:Eu^{3+}$ thin films phosphors have been deposited on Si (100) substrates using pulse laser deposition with deposition time varying from 30 to 60 minutes. The x-ray diffraction results indicated that crystallinity of the thin films improved by increasing deposition time to 60 minutes. SEM images showed rough surface and larger grain particles appear in sample with higher deposition time of 60 minutes. The AFM showed that the surface of the film became smooth and agglomerated at low deposition time and larger grains observed at 60 minutes deposition time. The luminescence properties showed emission spectra of $YVO_4:Eu^{3+}$ deposited with different deposition time. The best luminescence intensity was obtained for the sample deposited for 60 minutes.

References

- [1] S. L. Jones, D. Kumar, K. G. Cho, R. Singh, P. H. Holloway, *displays*, **19** (1999) 151-167.
- [2] W. Kang, J. Park, D. Kim, K. Suh, *Bull. Korean Chem. Soc.*, **22** (2001) 921-924.
- [3] G. Wang, W. Qin, D. Zhang, L. Wang, G. Wei, P. Zhu R. Kim, *J. Phys. Chem. C*, **112** (2008) 17042–17045.
- [4] V. B. Bhatkar, *IJESIT*, **2** (2013) 426-432.
- [5] X. Xiaoa, G. Lua, S. Shena, D. Maoa, Y. Guo, Y. Wang, *Materials Science and Engineering B*, **176** (2011) 72–78.
- [6] A. Kathalingam, N. Ambika, M. R. Kim, J. Elanchezhian, Y. S. Chare, J. K. Hee *Materials Science-Poland*, **2** (2010) 28.
- [7] G. R. Bai, H. Zhang, C. M Foster, *Thin Solid films*, **321** (1998) 115.
- [8] G. E. Patil, D. D. Kajale, V. B. Gaikwad and G. H. Jain, *International Scholarly Research Network ISRN Nanotechnology*, Article ID 275872, (2012) 1-5.
- [9] J. Hao, S. A. Studenikin, M. Cocivera, *J. Lumin*, **93** (2001) 313.
- [10] S. Ekambaram, K. C. Patil, *J. Alloys Compounds*, **217** (1995) 104.
- [11] Y. S. Chang, F. M. Huang, Y. Y. Tsai, L. G. Teoh, *J of Luminescence*, **129** (2009) 1181-1185.
- [12] J. M. Nedelec, C. Mansuy, *Journal of Sol-Gel Science and Technology*, **32** (2004) 253–258.
- [13] J. Li, M. Kuwabara, *Sci. Tech, Adv, Mater*, **4** (2003) 143.
- [14] Y. Cho and Y. Huh, *Bull. Korean Chem. Soc.*, **32** (2011) No. 1 335.
- [15] D. Kim, W. Kang, *Bull. Korean Chem. Soc.*, **25** (2004) 1859-1862.
- [16] A. Kassima, H. S. Mina, A. H. Abdullah, N. Karrima, S. Nagalingm, *Digest Journal of Nanomaterials and Biostructures*, **5** (2010) 975-980.

- [17] H. Xu, H. Wng, T. Jin, H. Yan, *Nanotechnology*, **16** (2005) 65-69.
- [18] S. Yi, J. S. Bae, B. C. Choi, K. S. Shim, H. K. Yang, B. K. Moon, J. H. Jeong, J. H. Kim, *Optical Materials*, **28** (2006) 703-708.
- [19] B. D. Cullity, *Ellements of X-ray Diffraction*, (1978) 284-285.
- [20] L. F. Koao, F. B. Dejene, H. C. Swart, *Materials Science in Semiconductor processing*, **27** (2014) 33-40.
- [21] P. J. Sophia, G. Attolini, M. Bosi, E. Buffagni, C. Ferrari, C. Frigeri, K. Vad, A. Csik, V. Takáts, Z. Zolnai, *ECS Journal of Solid State Science and Technology*, **4(3)** (2015) 53-56.
- [22] J. C. Batista, P. C. de Sousa Filho, O. A. Serra, *Dalton Trans*, **41** (2012) 6310-5318.
- [23] H. K. Yang, B. K. Moon, B. C. Choi, J. H. Jeong, J. H. Kim, 15th Microoptics Conference (MOC'09), (2009) 25-28.
- [24] I. D. Faryuni, B. W. Nuryadin, F. Iskandar, M. Abdullah, T. Ogi, K. Okuyama, *J. of Luminescence*, **148** (2014) 165–168.

9.1 Summary

In this study the morphological, structural and luminescence properties of the yttrium vanadate and zinc vanadate phosphors were discussed. The vanadate phosphors have been prepared by combustion and sol-gel method. The thin films phosphors have been prepared by pulse laser deposition. The annealing process in the sol-gel method was performed at the temperatures of (700, 770 and 850°C) while the combustion process was performed under the initiation temperature of 600°C.

The structural, morphological, and photoluminescence characterization of undoped and Ca, Ba and Sr doped self-yellow $Zn_2V_2O_7$ synthesized via the combustion method has been discussed. First the $Zn_2V_2O_7$ was synthesized at different synthesis temperatures of 500, 600 and 700°C. It was found that the XRD structure obtained was single phase at low and higher synthesis temperature and the best luminescent intensity was obtained for samples synthesized at 600°C. The $Zn_2V_2O_7$ was then doped with the different dopants (Ca, Ba, Sr). The XRD structure showed that no impurities or secondary phases were observed by adding the different dopants to $Zn_2V_2O_7$ were observed.

The effects of annealing temperatures on structural and luminescence properties of $Zn_2V_2O_7$ were studied. $Zn_2V_2O_7$ phosphor powders were annealed at 700 – 850°C for 2 hours. It was obtained that the annealing temperature has influence on the structure and morphology. The aggregation of particle was increasing with the particles size from 77 nm at 700°C to 90 nm at 850 °C. The photoluminescence emission spectra of $Zn_2V_2O_7$ annealed at different temperature was observed. The broad yellow to green emission band of $Zn_2V_2O_7$, which consist of the two peaks corresponding to the 3T_2 and 3T_1 states to the 1A_1 ground state of V^{5+} ions, was observed.

The effect of YVO_4 phosphor material doped with different concentration of Dy^{3+} has been study. SEM images show that the particle size seemed to increase along with the concentration of Dy^{3+} . The emission colour of the luminescence is yellow ($^4F_{9/2} \rightarrow ^6H_{13/2}$) and approaching white region due to the blue ($^4F_{9/2} \rightarrow ^6H_{15/2}$) emissions of Dy^{3+} and has the potential to be used as a phosphor for pc-LEDs. The intensity of the PL decreased while increasing the concentration due to concentration quenching.

Dy³⁺ ions give most intense emission in the yellow region. Because of these colours the combined emission is close to white and it can extensively be used as an activator ion in designing the LED based white light sources. The effect of urea:nitrate ratio on the structure and luminescence properties of YVO₄:Dy³⁺ phosphors has been studied. XRD results revealed a single tetragonal phase (JCPDS No. 17-0341). No other crystalline phase was observed on the XRD spectra. It was observed that when increasing the concentration of urea further the flake-like particles was formed because an increase in urea increased the exothermic flame and hence the formation of crystalline structures.

Effect of substrate temperature on structure and luminescence properties of YVO₄:Eu thin films grown by PLD. YVO₄:Eu thin films were deposited by PLD under the various substrate temperature and oxygen pressures. The diffraction peaks of the thin films showed the tetragonal phase structure. An increase in substrate temperature led to an improvement in crystallinity and the roughness of the surface of YVO₄:Eu thin films. The spectra showed an increase in intensity when deposition temperature increased and the maximum intensity was reached at 400 °C.

Optimizing deposition time to enhanced photoluminescence properties of laser-ablated red Eu³⁺ doped YVO₄ thin films. The poor crystallinity was observed at the deposition time of 30 minutes. It was observed that the crystallinity improved after the deposition time of 45 minutes, and the best film was observed after the deposition time of 60 minutes. The AFM showed that the surface of the film became smooth and agglomerated at low deposition time and larger grains observed at 60 minutes deposition time. The luminescence properties showed emission spectra of YVO₄:Eu³⁺ deposited with different deposition time. The best luminescence intensity was obtained for the sample deposited for 60 minutes.

9.2 Recommendations for future work

With the optimal composition of $\text{YVO}_4:\text{Eu}^{3+}$, $\text{YVO}_4:\text{Dy}^{3+}$, $\text{Zn}_2\text{V}_2\text{O}_7$ and (Ca, Ba, Sr)-doped $\text{Zn}_2\text{V}_2\text{O}_7$ phosphors, it would be of the interest to further test the performance of the phosphors for future applications.

- 1) Temperature measurements should be performed at atmospheric pressure. It is known that the thermal response of $\text{YVO}_4:\text{Eu}^{3+}$ phosphors shows dependence to temperature. It would be of the interest to verify the performance of $\text{YVO}_4:\text{Dy}^{3+}$, $\text{Zn}_2\text{V}_2\text{O}_7$ and (Ca, Ba, Sr)-doped $\text{Zn}_2\text{V}_2\text{O}_7$ phosphors at different temperature, possibly for thermo graphic phosphors applications.
- 2) More investigations involving laser power, energy density, fluence and substrate target distance should be explored involving films deposited by using Pulsed Laser Deposition technique.
- 3) Elaborate and accurate phase change monitoring techniques using In situ-XRD technique needs to be incorporated in future research activities.
- 4) Use of XPS, TEM and Time of Flight (ToF SIMS) as a characterization methods needs to be emphasized.

9.3 List of publications and proceedings

- K. E. Foka, B. F. Dejene, H. C. Swart, The effect of urea:nitrate ratio on the structure and luminescence properties of $\text{YVO}_4:\text{Dy}^{3+}$ phosphors, *Physica B: Physics of Condensed Matter*, 480 (2016) 95-99.
- K. E. Foka, B. F. Dejene, H. C. Swart, Effect of substrate temperature on structure and luminescence properties of $\text{YVO}_4:\text{Eu}^{3+}$ thin films grown by PLD, *Applied Physics A*, (2016) 122-189.
- K. E. Foka, F. B. Dejene and H. C. Swart, Characteristic of Ce^{3+} doped SrAl_2O_4 prepared by Solution Combustion method, *Physica B: Physics of Condensed Matter*, 439 (2014) 177–180.
- K. E. Foka, F. B. Dejene and H. C. Swart, Structural and luminescence properties of self-yellow emitting undoped $\text{Zn}_2\text{V}_2\text{O}_7$ and (Ca, Ba, Sr)-doped $\text{Zn}_2\text{V}_2\text{O}_7$ phosphors synthesised by combustion method, submitted February 2015 *J. of Solid State Science*
- K. E. Foka, F. B. Dejene and H. C. Swart, Synthesis and characterization of a green $\text{CaAl}_x\text{O}_y:\text{Tb}^{3+}$ phosphor using solution combustion method, SAIP'2011 Proceedings, the 56th Annual Conference of the South African Institute of Physics, edited by I. Basson and A.E. Botha (University of South Africa, Pretoria, 2011), p 90-94. ISBN: 978-1-86888-688-3
- K. E. Foka, F. B. Dejene and H. C. Swart, Characterization of green $\text{SrAl}_2\text{O}_4:\text{Tb}^{3+}$ phosphor synthesized using solution-combustion method, accepted SAIP 2012 Proceedings, in Proceedings of SAIP2012: the 57 Annual Conference of the South African Institute of Physics, edited by Johan Janse van Rensburg (2014), pp 63-68. ISBN: 978-1-77592-070-0 Available online at <http://events.saip.org.za>.
- K. E. Foka, B. F. Dejene, H. C. Swart and R. Kittes, $\text{YVO}_4:\text{Eu}$ phosphor thin films prepared by PLD, in Proceedings of SAIP2013: the 58th Annual Conference of the South African Institute of Physics, edited by Roelf Botha and Thulani Jili (2014), pp. 31-36. ISBN: 978-0-620-62819-8. Available online at <http://events.saip.org.za>.
- K. E. Foka, B. F. Dejene and H. C. Swart, Combustion Synthesis of Dy^{3+} -doped YVO_4 phosphor, in Proceedings of SAIP2014: the 59th Annual Conference of the South African Institute of Physics, edited by Chris Engelbrecht and Steven Karataglidis (2015), pp. 34-40. ISBN: 978-0-620-65391-6, Available online at <http://events.saip.org.za>.